Eindhoven University of Technology

MASTER

Influence of substrate and tip on inelastic electron tunneling spectroscopy

Rossen, E.T.R.

Award date:
2007

Link to publication

technische universiteit eindhoven

Influence of substrate and tip on Inelastic Electron Tunneling Spectroscopy

Erwin Rossen
M.Sc. Thesis
August 2007

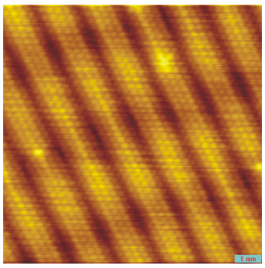

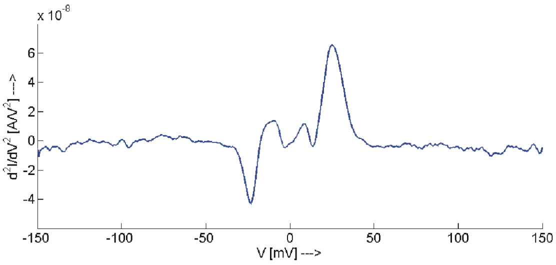

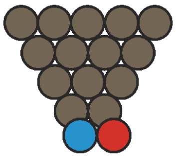

Faculty of Applied Physics
-
Molecular Materials and Nanosystems

Abstract

It has been proposed that our sense of smell works as an Inelastic Electron Tunneling Spectroscope. The electrons in the nose should be able to detect and recognize vibrations in a molecule. Detection of vibrations is governed by selection rules, and individual vibrations might be influenced by the substrates of the adsorbate molecules. STM-IETS is used to extract data, necessary for constructing selection rules, and to investigate the influence of substrates for NO on noble metals. A frustrated rotation mode is observed around 21 meV for NO molecules on Ag(100), other modes are not observed up to 150 meV. If an NO molecule is adsorbed to a silver terminated tip, the same vibration is identified as well, if it is adsorbed to a tungsten terminated tip, vibrations are observed around 56 and 110 meV, close to theoretically predicted values. Combining experiment and calculations shows that NO on a Ag-terminated tip is oriented upright, where the NO molecule is bound flat to a W-terminated tip. To predict IETS spectra, the tunneling junction has been modeled. For the non resonant case, the NEGF method is applied to calculate the influence of additional phonons to the system, which turns out to be very small. When a very high number of phonons is added, IETS features diminish. For the resonant case, a modification to the model has been applied, though implementation of a necessary FFT leads to lack of results.

Preface

The present thesis is submitted in candidacy for the Master of Science degree within the Applied Physics program at the Eindhoven University of Technology. It describes my work carried out in the Molecular Materials and Nanosystems Group, which is part of the Applied Physics faculty, from June 2006 to August 2007 under the supervision of Kees Flipse.

I am grateful to my supervisor Kees Flipse for all the efforts and interest he put into this project with lots of enthusiasm. I would like to thank all my colleagues in the M2N group for all their help, whether it be experimental expertise, fruitful discussions or good company during coffee and lunch breaks. In particular, I would like to thank Joris Hagelaar, who has been my guide for the past year and was always willing to explain things, to help me out, to discuss results, to ask questions and to answer questions.

The intended level of the text is aimed at fellow students with background knowledge of quantum mechanics. Concepts as energy diagram, density of states or tunneling are assumed to be known. For more advanced concepts used, like orbital hybridization, second quantization or Green's functions, references are given to introductory text books.

My interest in this project was large enough to decide to pursue a PhD on a similar project as this one. This means that I remain into the subject and are always willing to discuss this with others. If the reader wishes to ask questions, put forward comments or discuss similar matter, he or she is invited to send me an e-mail at `erwin.rossen@gmail.com`. Have fun reading!

Erwin Rossen, Eindhoven, September 14, 2007

Contents

1 Introduction **7**

2 Theory **11**
- 2.1 Scanning Tunneling Microscopy . . . 11
- 2.2 Inelastic Electron Tunneling Spectroscopy . . . 14
- 2.3 Single molecule IETS . . . 16
- 2.4 Resonant vs. far off resonance tunneling . . . 16

3 Experimental setup **19**
- 3.1 Preparing the surfaces . . . 19
- 3.2 Scanning tunneling microscope . . . 20
- 3.3 Scanning tunneling spectroscopy . . . 21

4 Experimental STM and IETS results **23**
- 4.1 IETS on Nitric Oxide . . . 23
- 4.2 Au(111) and Ag(111): *sp*-surface states . . . 26
- 4.3 Au(100) . . . 28
- 4.4 Ag(100) . . . 30
- 4.5 Conclusions . . . 38

5 Simulations - Non resonant case **39**
- 5.1 The physical model . . . 40
- 5.2 The mathematical model . . . 42
- 5.3 Assumptions and limitations . . . 48
- 5.4 Calculation scheme . . . 48
- 5.5 Technical details . . . 51
- 5.6 Raising the phonon occupation . . . 52
- 5.7 Numerical results . . . 53

6 Simulations - Resonant case **57**
- 6.1 Lang-Firsov transformation . . . 57
- 6.2 Mathematical model . . . 59
- 6.3 Calculation scheme . . . 60

6.4 Lehmann representation 64
6.5 Technical details 65
6.6 Influence of energy range 66

7 Summary and outlook 69
7.1 IETS - The experiment 69
7.2 IETS - The theory 70

A Clean Au and Ag substrates 73
A.1 Au(111) 73
A.2 Ag(111) 75
A.3 Au(100) 76
A.4 Ag(100) 76

B Matlab files belonging to chapter 5 79

C Matlab files belonging to chapter 6 89

Chapter 1

Introduction

As we move around in this world, we acquire information about our environment through our senses and interpret them with our mind. This perception is provisional, which means that it can change with new information, just as scientific hypotheses can be rejected or altered when new observations are taken into account. The gathering of information with our senses is therefore equivalent to conducting scientific experiments to gain more understanding of the environment or nature itself. We use five senses to gather this information: sight, hearing, taste, smell and touch. The sensory systems of the human body have extensively been studied the past century, and a lot is known about how the human body translates certain features of the environment (e.g. electromagnetic radiation, vibrations, presence of certain molecules) into electrical impulses, which are processed in the brain.

One sense fully understood is for instance sight. When a light ray enters the human eye, the cornea and the pupil act together as a lens to refract the ray and project an inverted image on the retina. This retina consists of a large number of photoreceptor cells. They contain a particular protein called opsin. In the human eye, there are two types of opsins: rod opsins and cone opsins. In the presence of light, both opsin molecules can absorb a photon, thereby changing their configuration, and as a result generating a nerve impulse. There are three types of cones that differ in the wavelength of the light they absorb. The brain combines the information from each type of receptor to perceive the brightness and the color (i.e. wavelength) of the incident light ray. Because of the ability to detect wavelengths, this sense is called a *spectroscopic* sense. Another spectroscopic sense is hearing.

One sense which is not spectroscopic but *chemoreceptive* is taste. Humans receive tastes through sensory organs called taste buds, concentrated on the upper surface of the tongue. There are five basic tastes: saltiness, sourness, sweetness, bitterness and umami. The receptors for sour and salty are ion channels, which are pore-forming proteins that help to establish and control the small voltage gradient across the cell membrane by allowing a flow of ions. The receptors for sweet, bitter and umami are G-protein coupled receptors, that are proteins that sense molecules outside the cell and activate cellular responses. Their shape often dictates the kind of molecules they can sense outside.

The sense of smell however, is not yet understood. Synthesis of new odorants proceed largely by trial and error. Nowadays, there are two main theories to describe olfaction: the odotope theory, assuming smell is a chemoreceptive sense, and the vibration theory, assuming that smell is a spectroscopic sense. These two theories have been reviewed in reference [1], here a brief description of both theories is presented.

According to odotope theory, different receptors inside the nose bind to structures of the odorant as a key fits to a lock. The pattern of receptor activation is interpreted by the brain to identify in a unique fashion the whole odorant molecule. The main argument in favor of this theory is that the identified receptors respond to many odorants, so that receptors are binding to a feature shared by the odorants. Odorants with a common feature are called odotopes. Main arguments against this theory is that there are many examples of molecules of very similar shapes having very different smells and the fact that functional groups (e.g. thiol) can easily be identified, which would be too small odotopes for an accurate detection.

According to vibration theory, the odorants are still bound to a receptor. However, the vibrations of the odorant molecule are determined by the nose. These vibrations are in a similar manner interpreted by the brain to identify the whole odorant molecule. Main arguments in favor of this theory is that functional groups can easily be detected and isotopes can be distinguished. Main arguments against this theory that it is unable to account for odorant intensity and there is no proof of a biological mechanism to sense vibrations.

Luca Turin proposed a mechanism for detection of vibrations by suggesting that the receptors act as an inelastic electron tunneling spectrometer (IETS) [2]. In IETS, electrons tunnel through a narrow gap from one metallic electrode to another. If the gap is empty, the electrons cross the gap at constant energy, and the bridge is ohmic. If a molecule is present in the gap, tunneling electrons might excite a vibrational mode of the molecule on the way. The minimum amount of energy the electron should have to be able to do so is the energy of that vibration. This new tunneling path causes an increase in conduction of the bridge, which corresponds to a narrow peak in the second derivative of the current to the voltage at energies corresponding to the vibrational modes of the molecule in the gap. Of course, there are no metallic electrodes inside the nose. The electron source and sink would be two proteins, with a gap in between to fit an odorant. Probably not the second derivative of the current, but only the inelastic part of the current is measured inside the nose. To get more insight into vibrational spectroscopy as the mechanism of our sense of smell, several questions have to be answered, such as:

- Some odorants of essentially identical shape smell completely different. Also intensities of the smell can change a lot. This might be due to differences in frequency of the vibrational modes, but also due to different coupling of certain vibrational modes to tunneling electrons. What is the influence of electron-phonon coupling on our sense of smell?

- The binding of molecules onto the proteins will change the vibrational mode frequencies and couplings. What restrictions does the binding of molecules impose on the ability to smell certain molecules?

To address these issues, experiments are required. To imitate the nose as an inelastic spectrometer, a scanning tunneling microscope (STM) is equipped with spectroscopic tools to perform single molecule vibrational spectroscopies. The proteins are replaced by a metallic substrate and a metallic STM tip, the odorants are replaced by adsorbates, which are not necessarily odorous. In this research, NO molecules are used as adsorbates, because there is already data about NO molecules on rhodium. Besides that, diatomic molecules are the easiest molecule to study, because they do not have a long list of vibrational modes. The substrates used are either gold or silver substrates, that have a weaker bond with the NO molecules compared to rhodium. The IETS spectra of NO on silver are compared to the spectra of NO on rhodium and CO on copper to experimentally investigate the influence of the substrates on the positions, widths and intensities of the IETS peaks. It is found that the spectra depend strongly on the termination of the used tip. This dependence is reviewed in this thesis.

Due to the fact that electron-phonon coupling is important to know with which intensities vibrational modes can be detected, predictions of these intensities are not easy. Experiments are required to determine intensities and calculate couplings in order to construct selection rules for electron-phonon couplings. These selection rules are not only important in understanding the nose, but also for molecular electronics, the subfield of nanotechnology where molecular building blocks are used to fabricate electronic components.

To improve the understanding of qualitative and quantitative features in STM-IETS spectra, the experiments are modeled. There are several models available for this system, valid for several subproblems. The approach based on many-body physics, and in particular using non equilibrium Green's functions (NEGF), is used here. This NEGF formalism provides a consistent and systematic framework to describe transport phenomena in interacting particle systems. The consistency however, is inevitably accompanied by complexity, and approximations are required to evaluate the needed Green's functions. The most common one is the Born approximation (BA) and an extension of this, the self consistent Born approximation (SCBA). In this thesis, the NEGF formalism is applied with the SCBA to calculate IETS spectra for different parameters to theoretically investigate the influence of the contacts on the positions and intensities of the IETS peaks.

The present thesis is organized as follows. This chapter presents a motivation of conducting IETS experiments and puts forward the fundamental issues which we want to address. Chapter 2 provides the general theory of STM, IETS and single molecule STS and introduces several parameters that indicate in which regimes we are working, important for the expected outcome. The experimental setup used is described in chapter 3, whereafter the experimental results are presented and discussed in chapter 4. The NEGF formalism and the SCBA are introduced in chapter 5, and used to calculate IETS spectra in the limit of weak electron-phonon coupling. In the case of intermediate to strong electron-phonon coupling, a slightly different approach is used. This approach is introduced in chapter 6, and used to calculate IETS spectra in this limit. Finally, chapter 7 summarizes the thesis and provides an outlook for future work.

Chapter 2

Theory

This chapter explains the theory which is required to understand the conducted IETS experiments. First, section 2.1 explains the general theory of the scanning tunneling microscope, after which in section 2.2 the theory of inelastic electron tunneling spectroscopy is explained. In section 2.3, these two techniques are combined to be able to perform IETS on single molecules. A few parameters used in the model described in section 2.2 are highlighted in section 2.4. A more elaborate physical model of this system, based on the non equilibrium Green's function method, will be explained in chapters 5 and 6, where computer simulations are described.

2.1 Scanning Tunneling Microscopy

A scanning tunneling microscope (STM) is a microscope which can produce images of surfaces with atomic resolution utilizing tunneling currents. It is invented in 1981 by Gerd Binnig and Heinrich Rohrer of IBM's Zurich Lab in Switzerland [3], which earned them the Nobel Prize in Physics in 1986. The standard setup is shown in figure 2.1. An atomically sharp tip is brought to within a few atomic diameters of the surface under investigation. There is no physical contact, so there is a very small overlap of the wavefunctions of the surface with the wavefunctions of the end atom of the tip. When a bias voltage, ranging from 1 mV to 10 V, is applied between the sample and the tip, electrons tunnel across this gap with a probability that increases exponentially as the tip approaches the sample. The tunneling current is roughly given by the following equation [4],

$$I = cV \exp\left[-d\sqrt{\Phi}\right] \tag{2.1}$$

where c is a constant, Φ is the barrier height of the tunneling gap, measured in electron volts, V is the applied voltage and d is the distance between tip and surface, measured in Angstroms. This exponential dependence makes the STM extremely sensitive to detect small changes in the surface height due to individual atoms. Scanning over a surface and measuring - at fixed bias - the tunneling current at each point gives in principal a topographic map of the surface under investigation. In practice, a feedback loop corrects

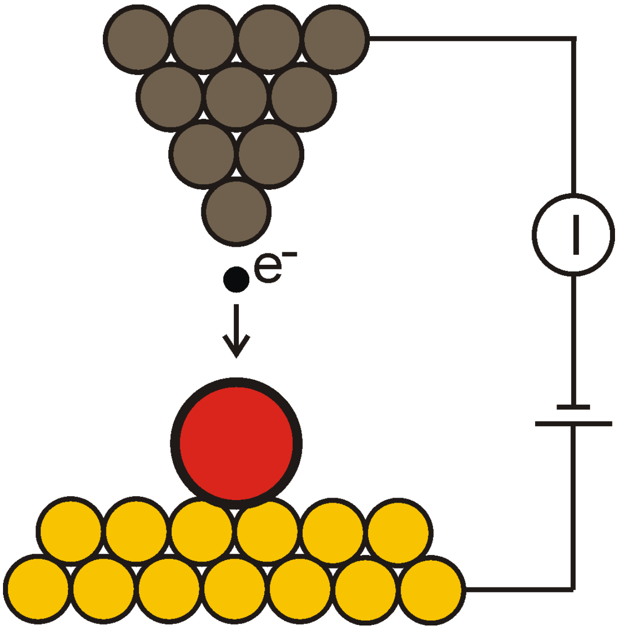

Figure 2.1: *The standard setup of an STM schematically drawn.*

the vertical position of the tip to maintain a constant current, called the setpoint current, and records the vertical corrections as the *topographic mapping* and the deviations from the setpoint current as the *current mapping*.

Equation 2.1 is however an approximation that is valid only in the *wide band limit*, which assumes a constant density of states of both sample and tip. How the density of states of the sample and tip come into play, is shown in figure 2.2.

This figure shows the energy level diagram for the system consisting of the sample, the tip and the vacuum in between. Figure 2.2a shows the case where the sample and tip are independent, so their vacuum levels are considered to be equal. Their respective Fermi energies (E_F) lie below the vacuum level by their respective work functions ϕ_s and ϕ_t. If the sample and tip are in thermodynamical equilibrium, their Fermi energies must be equal, as is shown in figure 2.2b. Electrons attempting to pass from sample to tip encounter a potential barrier, which they can tunnel through if the barrier is sufficiently narrow. When a voltage V is applied to the sample, its energy levels will be shifted upward (if $V < 0$) or downward (if $V > 0$) in energy by the amount $|eV|$, where e is the electronic charge. At positive sample bias, the net tunneling current arises from electrons that tunnel from the occupied states of the tip into the unoccupied states of the sample, as is shown in figure 2.2c. At negative sample bias, the net tunneling current arises from electrons that tunnel from the occupied states of the sample into the unoccupied states of the tip, as is shown in figure 2.2d. An expression for this tunneling current can be found using the WKB method [5], and is given in equation 2.2,

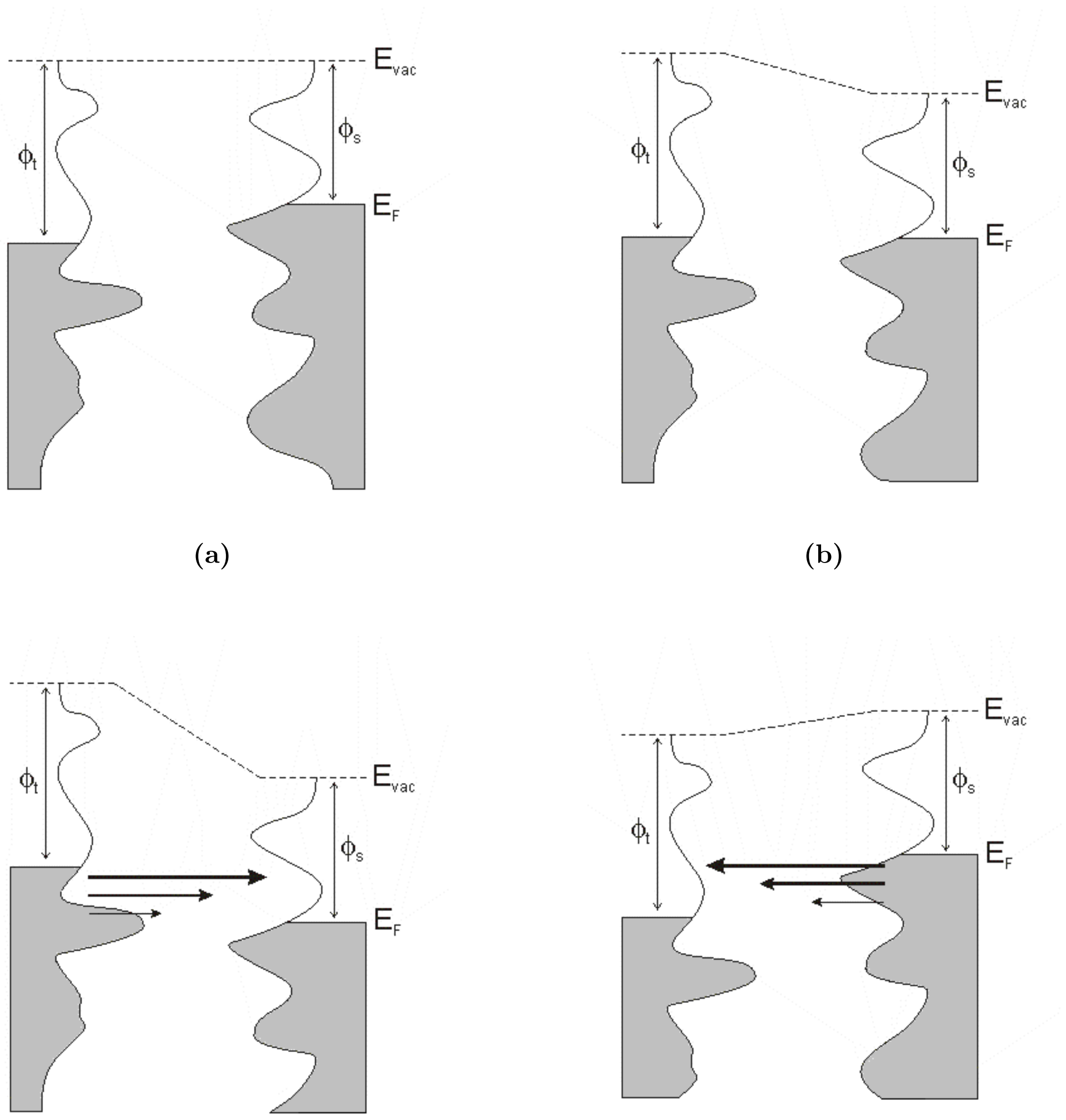

(a) **(b)**

(c) **(d)**

Figure 2.2: *Energy level diagrams for sample and tip. a) Independent sample and tip. b) Sample and tip at thermodynamical equilibrium. c) Positive sample bias. Electrons tunnel from tip to sample. d) Negative sample bias. Electrons tunnel from sample into tip.*

$$I = \int_0^{eV} \rho_s(E)\rho_t(E - eV)T(E, eV)dE \tag{2.2}$$

where $\rho_s(E)$ is the (local) density of states of the sample, $\rho_t(E)$ is the density of states of the tip and $T(E, eV)$ is the transmission probability. In the WKB approximation, this probability is given by the following equation [5],

$$T(E, eV) = \exp\left[-\frac{2Z\sqrt{2m}}{\hbar}\sqrt{\frac{\phi_s + \phi_t}{2} + \frac{eV}{2} - E}\right] \tag{2.3}$$

where m is the electron mass, $\hbar$ is Planck's constant, Z is the tip-sample separation and E is the energy measured with respect to the Fermi level. This expression again shows the exponential dependence on the tip-sample separation, but also the influence of E. States with the highest energy have the longest decay lengths into the vacuum, so most of the tunneling current arises from electrons lying near the Fermi level of the negative-biased electrode. The dependence of the tunneling current on the overlap of wavefunctions of tip and sample (equation 2.2) implies that STM does not reveal the positions of atoms themselves, but rather the electronic density of states, which is assumed to be higher around the atoms. It also implies that with an STM, it is possible to obtain spectroscopic information with atomic spatial resolution.

2.2 Inelastic Electron Tunneling Spectroscopy

Inelastic electron tunneling spectroscopy (IETS), developed in the 1960s, is an experimental tool for studying the vibrations of molecular adsorbates on metal oxides. It yields vibrational spectra of the adsorbates with high resolution (< 0.5 meV) and high sensitivity ($< 10^{13}$ molecules are required to provide a spectrum [6]). An additional advantage is the fact that optically forbidden transitions may be observed as well [7].

Within IETS, an oxide layer with molecules adsorbed on it is put between two metal plates. A bias voltage is applied between the two contacts. Figure 2.3 shows the energy diagram of the metal-oxide-metal device under bias. The metal contacts are characterized by a constant density of states, filled up to E_F. The metals are assumed to be equal. The adsorbates are situated on the oxide material. They are represented by a single bridge electronic level, which is the upper dashed line. If the insulator is thin enough, there is a finite probability that the incident electron tunnels through the barrier. Since the energy of the electron is not changed by this process, it is an elastic process. This is shown in figure 2.3a.

Some of the tunneling electrons can lose energy by exciting phonons[1] of the oxide or the adsorbate. These inelastic processes lead to a second tunneling path, which gives an additional current contribution to the tunneling current. Since the incident electron should

---

[1] The term "phonons" is used in this thesis for vibrational modes associated with the adsorbate, which are in a strict sense no phonons.

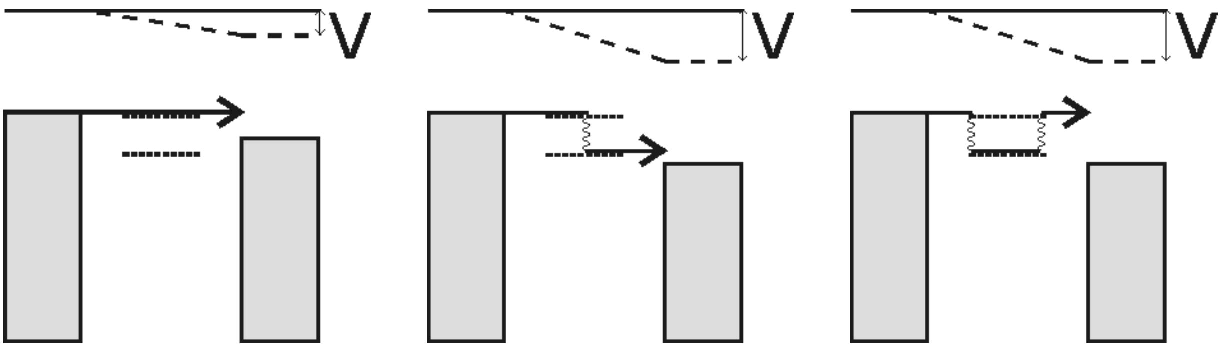

(a) Elastic tunneling **(b)** Inelastic tunneling **(c)** 2nd Order elastic tunneling

Figure 2.3: *A schematic drawing of the system under investigation, with an STM tip (left reservoir), a substrate (right reservoir), a molecule on top of the substrate (bridge electronic level) and a voltage applied between tip and substrate. The wide band limit is assumed for both the sample and the tip. a) Traveling electrons do not have sufficient energy to excite a phonon. Only elastic tunneling can take place. b) When increasing then bias voltage beyond* $V = \frac{\hbar\omega_0}{e}$*, traveling electrons do have sufficient energy to excite a phonon with energy* $\hbar\omega_0$*. Inelastic tunneling can take place. c) Traveling electrons can also excite and subsequently reabsorb a phonon, which leads to second order elastic tunneling.*

have enough energy to excite this phonon, there is a minimum energy that is the onset of this (inelastic) process. This is shown in figure 2.3b, where the lower dashed line is a vibronic state. This minimum energy for the electron corresponds with a minimum bias voltage, which is the onset for the additional contribution. The inelastic contribution to the current is small compared to the elastic tunneling current ($\sim 0.1\%$) and is more clearly seen as a peak in the second derivative of the current to the bias voltage, as can be seen in figure 2.4.

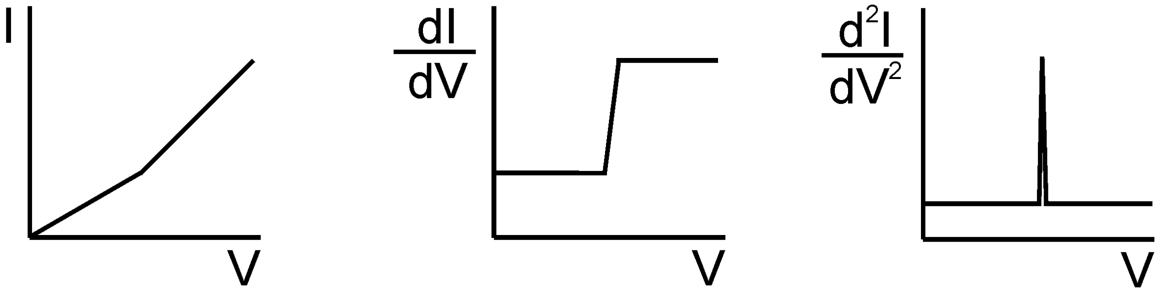

(a) (b) (c)

Figure 2.4: *A change of slope in the current vs. voltage (a) leads to a step in the first derivative (b) and to a peak in the second derivative (c) of the current to the voltage.*

There is however also an important correction to the elastic component of the tunneling current at the onset. This is a second order effect in electron-phonon coupling, where a phonon is emitted and reabsorbed or vice versa. This is shown in figure 2.3c. Depending on the energetic parameters of the system, this correction may be negative and it may outweigh the positive contribution of the inelastic current, resulting in a dip in the IETS spectrum. This is experimentally verified in both regular IETS (see e.g. [8]) and in STM-IETS (explained below, see e.g. [9]) and is also theoretically observed (see e.g. [10]). Not only peaks and dips may be observed, but depending on the energetic parameters also derivative-like features may be observed (see experimentally e.g. [11], see theoretically e.g. [12]).

2.3 Single molecule IETS

By using an STM and keeping the tip at a fixed position over the surface and sweeping the bias voltage, one can record a $I - V$ characteristic. This technique is called Scanning Tunneling Spectroscopy (STS). The first derivative gives information about the Local Density of States (LDOS) of the substrate, assumed that the tip has a constant density of states. The second derivative gives information on vibrations of the adsorbate, exactly as in IETS. That is why this technique is commonly called STM-IETS. The role of the insulating oxide layer is played by the gap between the tip and the adsorbate. The details of the experimental setup are discussed in chapter 3.

Nowadays molecular transport junctions have been produced with one single molecule between two electrodes, possibly with an additional, gate electrode near the molecule [13, 14, 15]. The advantage of this method in comparison with STM-IETS is that there is contact between both electrodes and the adsorbate, whereas in STM-IETS there is always a tunneling gap between the tip and the adsorbate. The disadvantage of this method is that it is experimentally very challenging to create and identify a junction with exactly one molecule between two electrodes.

2.4 Resonant vs. far off resonance tunneling

In the model described in section 2.2, there are several important energy parameters. Their influence on the system is described in detail by Galperin *et al.* [16]. An overview is given in this section.

The first important energy parameter is ΔE, which is the energy difference between the leads Fermi energy and the relevant bridge levels, illustrated in figure 2.5a. Second is Γ, which measures the broadening of bridge electronic states due to molecule-lead coupling. The larger Γ, the larger is the coupling between molecule and lead. The third one is γ_{ph}, which measures the broadening of molecular vibrations due to contact to thermal phonons in the environment. This parameter is assumed to be small relative to all other energetic parameters throughout this thesis. The last important energy parameter is M, which is a measure for the electron-phonon coupling.

If ΔE is large, the density of electronic states around E_F is low and the probability to tunnel onto the bridge molecule is small. This is called *deep tunneling* or *far off resonant tunneling.* If, however, ΔE is close to 0, the electron easily occupies the bridge electronic state. This is called *activated transport* or *resonant tunneling.* This is illustrated in figure 2.5.

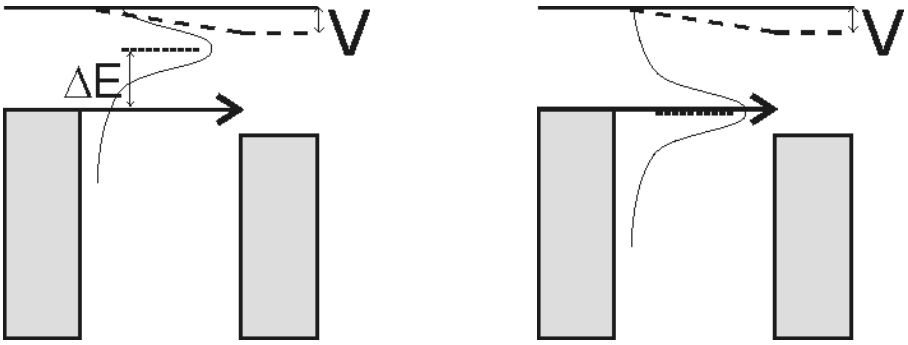

(a) Far off resonance tunneling **(b)** Resonant tunneling

Figure 2.5: *a) When the electronic level is far from the Fermi energy (i.e.* $\Delta E \gg 0$*), the density of states (the bell shaped curve) is low at* E_F*. This is called far off resonance tunneling. b) When the electronic level is near the Fermi energy (i.e.* $\Delta E \approx 0$*), the density of states is high at* E_F*. This is called resonant tunneling.*

There are important time scales related to the energy parameters. $\frac{\hbar}{\Gamma_K}$ measures the lifetime of a bridge electron for escaping into contact K. $\frac{\hbar}{\gamma_{ph}}$ is the relaxation time for bridge phonons to their thermal phonon environment. Γ_K and γ_{ph} represent the corresponding rates. An important time scale is the *dephasing time*, which is a measure of the time it takes for an electron to lose its phase due to electronic or phononic interactions. Another time scale is the *tunneling traversal time*, which is a measure of the time an electron spends on the bridge. For deep tunneling Nitzan *et al.* derived a general formula for this tunneling traversal time [17]. In the limit that the bridge is modeled by a one dimensional lattice of N equivalent sites, $\tau = \frac{\hbar N}{\Delta E}$. For resonant tunneling, this time depends on the escape rate Γ. This leads to the following unified expression to estimate the traversal time per bridge site,

$$\tau \sim \frac{\hbar}{\sqrt{\Delta E^2 + \Gamma^2}} \tag{2.4}$$

When the tunneling traversal time is greater than the dephasing time, the electronic motion becomes incoherent and can be described by successive classical rate processes, known as hopping. When the tunneling traversal time is smaller than the dephasing time, dephasing can be disregarded and the electronic motion is a coherent process. Equation 2.4 shows that for off resonant tunneling (large ΔE) or resonant tunneling with large electronic coupling to the contacts ($\Delta E \approx 0$, large Γ), the electronic motion is coherent, while for resonant tunneling with small electronic coupling to the contacts ($\Delta E \approx 0$, small Γ), the transmission proceeds by successive hopping, where at each site complete local thermalization is achieved. A model to describe the far off resonance case will be presented in chapter 5, while chapter 6 covers the resonant regime.

Chapter 3

Experimental setup

This chapter describes the details of the used experimental setup. Sample preparation is discussed in section 3.1, after which the hardware and electronics of the STM are discussed in section 3.2. A lock in amplifier is required to perform STS, which will be explained in section 3.3. This section also describes the used drift correction.

3.1 Preparing the surfaces

The surfaces used for this research are gold and silver samples, because they are expected to have a less strong bond with the used NO molecules than rhodium, for which information is already available. Section 4.1 gives a more elaborate explanation for the use of silver and gold samples.

Before the gold and silver samples are exposed to adsorbate molecules, they are mounted on a stainless steel or tantalum sample plate. Next, they enter the ultrahigh vacuum (UHV) system and undergo a cleaning procedure, which consists of sputtering and annealing. This cleaning procedure is carried out three times when the sample is fresh and is performed once every time the adsorbates need to be removed from the surface.

Sputtering is a process in which a surface is bombarded by high energy ions. The sputter gun used in this setup is the "Ion Source IQE 12/38", supplied by the "Ion Gun Power Supply 867 918" and the "Scan and Deflection Unit 867 916", all from Leybold-Heraeus. The inside of the sputter gun is schematically drawn in figure 3.1. The ions used in this setup are argon ions.

Neutral argon ions are let in the collision chamber of the sputter gun. A filament inside this chamber is heated by running a 5.5 A current through it. Thermal electrons are emitted and accelerated by an anode grid which has a potential of 100 V, resulting in a typical 10 mA emission current. While traveling to the anode, the electrons ionize the neutral particles present in the volume between filament (cathode) and anode. The anode is shaped in a way that permits the electrons to cross the anode volume many times to increase the probability of collision. The ions are extracted from the volume by a voltage of about 150 V and are accelerated to an energy of 1.5 keV. The ion beam is focused by ion

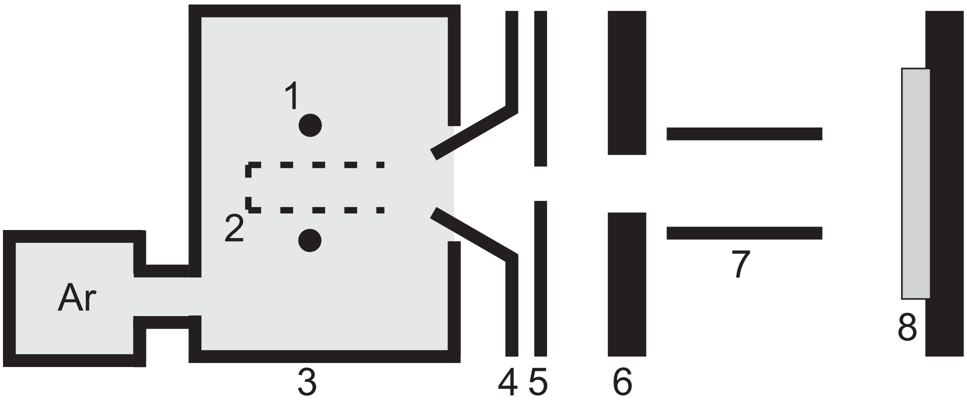

Figure 3.1: *The inside of the sputter gun, schematically drawn. 1) Ring shaped filament (cathode). 2) Cage shaped anode. 3) Electron repeller. 4) Ion extractor. 5) Ground plate. 6) Accelerator. 7) Deflection plates. 8) Sample plate.*

lenses onto the sample surface under an angle of 30 degrees relative to the surface normal. Two pairs of parallel plates under bias voltage, set with an angle of 90 degrees with respect to each other, are used to position and raster the ion beam onto the sample. The used range is 8×8 mm^2. The measured beam current between source volume and sample is 2-3 μA.

The result is that some of the atoms of the sample near the surface are ejected away from the sample. The number of atoms ejected from the surface per incident particle is called the sputter yield. At 1.5 keV and under this angle, the sputter yield of Ar ions on a Ag substrate is 7 and on a Au substrate is 5 [18]. One sputtering cycle takes $\sim$ 30 minutes, which corresponds with above mentioned parameters to the removal of 120-300 monolayers.

After sputtering, the surface is very rough with many deep holes. To repair this damage, the samples are annealed. In general, annealing is a heat treatment wherein a material is altered, causing changes in its properties. It involves heating a material, maintaining it at this temperature and cooling down again. In this case, the surface is heated and maintained to that temperature to increase the mobility of the surface atoms, promote diffusion and end up with larger flat terraces. The annealing temperature used is 500°C , the annealing time is $\sim$ 30 minutes. The heating is carried out with a ”ZEBHC6 Electron Bombardment Heater Temperature Controller” from Vacuum Generators. A filament is heated by running up to 2 A through it. Thermal electrons are accelerated to an energy of 650 eV towards the back side of the sample plate. The maximum emission current is 160 mA. Temperatures are measured by a thermocouple at the sample stage and desired temperatures are maintained using a PID temperature controller.

3.2 Scanning tunneling microscope

The STM used in this work is from Omicron Nanotechnology. It is situated inside a cryostat in a UHV system. The base pressure in the STM chamber is less than 10^{-11} mbar.

It is important that during STM and STS, the tip and the sample are not vibrating. Firstly because the tip-sample distance is ~ 0.5 nm, so a vertical vibration with an amplitude larger than this will cause the tip to crash after which it is unusable. Secondly because the resolution is at the atomic scale, so a vibrating tip or sample leads to a significant loss in the STM resolution. To suppress vibrations, the STM stage is hanged in springs. The frame of the entire setup is supported on an active damping control unit that compensates for vibrations of the system with a fast feedback system. To further repress vibrations, no pumps with moving parts are used during STM operation.

The STM is placed inside a gold heat shield, which is connected to a cryostat, to be able to cool down both the sample and the tip. There is an inner and an outer cryostat, each with its own heat shield. The outer one serves as an additional heat shield for the inner one. The inner cryostat can be filled with liquid nitrogen or helium to cool down to respectively 77 K and 4 K. The outer cryostat needs to be filled with liquid nitrogen. During STM operation, the shields of the cryostats are closed to refrain radiative losses to a minimum. The temperature inside is measured with a thermocouple on the STM stage.

The electronics to control the STM are from RHK Electronics. The tips used in this work are tungsten tips. Sometimes they are pushed slightly ($\sim 0.5nm$) into the substrate to sharpen the tips. This procedure is called *dipping*. The tungsten tips could then be terminated with the substrate material. The substrates are either gold or silver in either the (111) or the (100) orientation. The adsorbates are nitric oxide molecules. The NO inlet is shifted inside the cryostat to a distance of ~ 1 cm from the sample under an angle of ~ 70 degrees relative to the substrate's normal. The tip is less than 1 cm away from the substrate during deposition.

3.3 Scanning tunneling spectroscopy

To measure the first and second derivative of the tunneling current, a lock in amplifier is connected between the electronics and the STM. A lock in amplifier measures only one frequency component of the incoming signal by multiplying the input signal by a reference signal with amplitude $V_{ref,f}$. An additional AC modulation voltage with a specific frequency f_{mod} is applied on top of the DC bias voltage and the lock in is 'locked' on this frequency. It then measures $I_{sig,f}$, the current component of frequency f_{mod}. This current component is directly related to the first derivative of the current to the bias voltage $\frac{dI}{dV}$. A second lock in amplifier measures $I_{sig,2f}$, the current component of frequency $2f_{mod}$, which is directly related to $\frac{d^2I}{dV^2}$. These relations are clear from the Taylor expansion of $I(V)$ around $V = V_b$, where V_b is the DC bias voltage.

$$I(V) = I(V_b) + \frac{dI}{dV}(V - V_b) + \frac{1}{2}\frac{d^2I}{dV^2}(V - Vb)^2 + \dots \tag{3.1}$$

Because $V = V_b + V_{ref,f}\cos(2\pi f t)$, this translates into the next equation.

$$I(V) = I(V_b) + \frac{dI}{dV}V_{ref,f}\cos(2\pi f t) + \frac{1}{2}\frac{d^2I}{dV^2}V_{ref,f}^2\frac{1 + \cos(2\pi(2f)t)}{2} + \dots \tag{3.2}$$

The lock in tuned to f_{mod} measures $I_{sig,f} = \frac{dI}{dV}\frac{V_{ref,f}}{\sqrt{2}}$, because all other frequency components cancel out due to the multiplication mentioned above. The $\sqrt{2}$ in the denominator is due to the fact that the lock in is measuring RMS values, whereas $V_{ref,f}$ is the amplitude of the reference signal. Since this amplitude is known, the measured $I_{sig,f}$ can directly be related to $\frac{dI}{dV}$. The lock in tuned to $2f$ measures $I_{sig,2f} = \frac{1}{4}\frac{d^2I}{dV^2}\frac{V^2_{ref,f}}{\sqrt{2}}$, which means that the measured $I_{sig,2f}$ can directly be related to $\frac{d^2I}{dV^2}$. In the remainder of this thesis, $V_{ref,f}$ is written as V_{mod}.

There is always a lot of noise on the current measurements, as a result of which the IETS peaks cannot be identified by one single measurement. Therefore in order to determine an IETS spectrum, a lot of them are measured and an average is presented. To be able to take many IETS spectra at a certain place, the tip should be at a fixed position for a long time. However, even at low temperatures, there is a small lateral movement of the tip, which is called *drift*. At $T = 4$ K, the drift is less than 1 nm/h. In order to make sure all the spectroscopies are taken at the same position, a drift correction is applied in between two measurements. Before a spectroscopy is taken, a topographic mapping is recorded and compared to the previous mapping. The software is able to detect any lateral movements and corrects the position of the tip to the original position.

Chapter 4

Experimental STM and IETS results

This chapter gives an overview of the results from the STM and IETS experiments, conducted on nitric oxide (NO) molecules on gold and on silver. Section 4.1 first introduces the research of NO on metals by the work of J.H.A. Hagelaar about NO molecules on rhodium. The electronic structure of rhodium is different than the electronic structure of silver and gold, which is explained below. The absence of *d*-orbital holes makes the bonds of NO on silver and gold weaker. This means that the influence of the substrate on the bond of NO, and with it on its vibration, is less. There are four possible substrates to deposit the NO on: Au(111), Ag(111), Au(100) and Ag(100). The (111)-surfaces exhibit a problem with surface states, which is covered in section 4.2. The Au(100) surface exhibits the problem that NO is mobile on it, even at $T = 4$ K. This is covered in section 4.3. Ag(100) is the substrate that is eventually used to perform IETS measurements of NO on a noble metal. Section 4.4 displays and discusses the results of these measurements. In the end, section 4.5 draws conclusions from the available measurements and comparison to literature.

4.1 IETS on Nitric Oxide

The system of NO on Rh is interesting in the field of catalysis to convert NO into N_2 and O_2. To gain more understanding, this system has been extensively studied under UHV conditions. Hagelaar *et al.* [19] show that there are two structures in which the NO binds to the Rh, depending on the coverage. Figure 4.1b shows one of the two structures on the left side. IETS is performed on three different positions, labeled with the three blue dots. The spectra are shown in figure 4.1a. To show that the peaks can indeed be associated with the NO molecule, a scan is made of a single molecule where the $\frac{d^2I}{dV^2}$ is recorded. Figure 4.1c shows the ordinary topographic map of the single molecule, figure 4.1d shows the second derivative map. On top of the molecule the signal is the strongest, so the peak around $V = 55$ mV indeed comes from the NO molecule.

The expected peaks are summarized in table 4.1. Even when measuring on clean Rh, there are low frequency vibrational modes (i.e. below 10 meV). This is why in this experiment, the frustrated translation can never be distinguished. The frustrated rotation

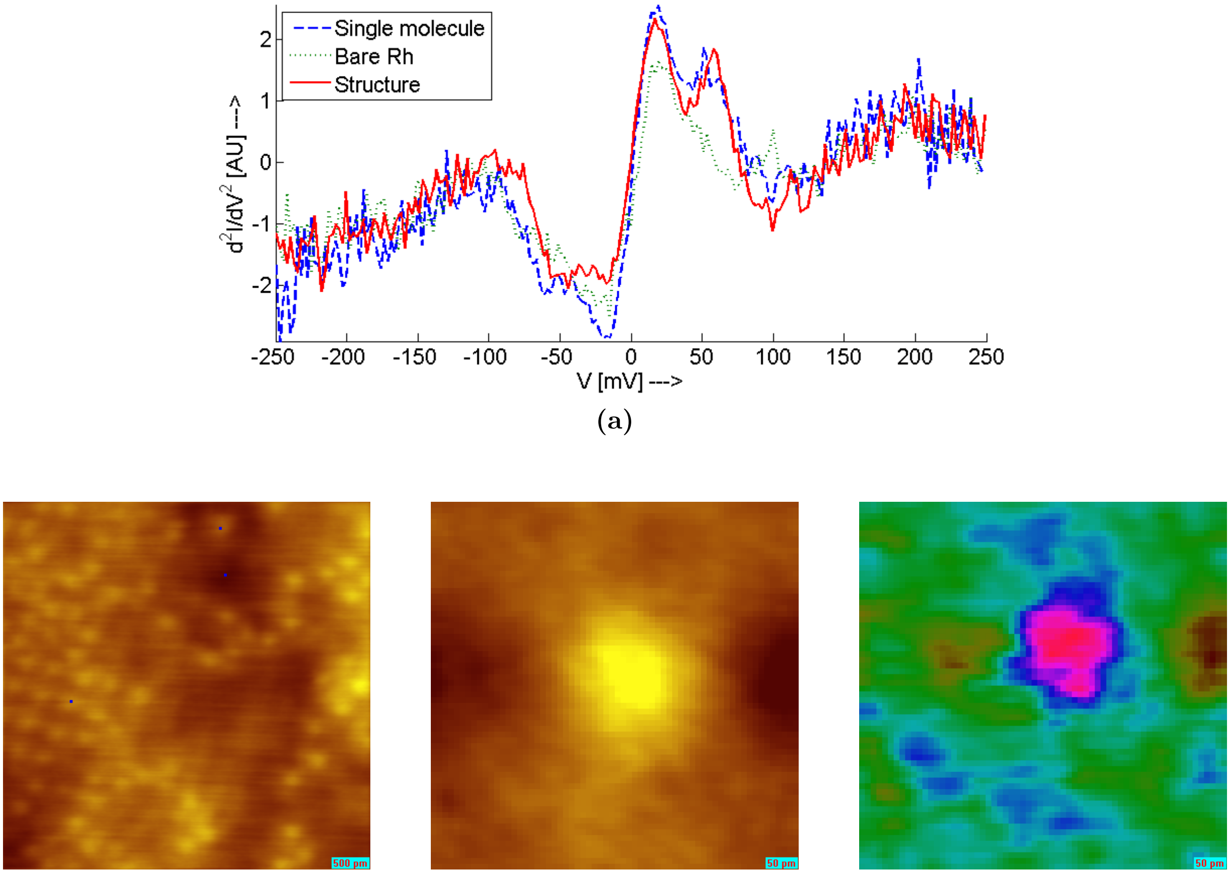

(a)

(b) **(c)** **(d)**

Figure 4.1: *a) IETS spectra taken on a single molecule (blue dashed line), on bare Rh (green dotted line) and on the NO structure (red solid line).* $V_{mod} = 14\ mV$*,* $f_{mod} = 4.7\ kHz$*, lock in time constant is 10 ms, pre-sample delay is 100 ms. The tunneling gaps were set with 100 mV sample bias and 2 nA tunneling current. A possible offset on the measured voltage is subtracted. b) A topographic image of NO on Rh. The three blue dots show where the spectra are taken. The scan size is* $4.87 \times 4.87\ nm$*,* $V_b = 100\ mV$*,* $I_{sp} = 2\ nA$*,* $T = 4\ K$*. c) A topographic mapping of a single NO molecule on Rh. The scan size is* $0.57 \times 0.57\ nm$*,* $V_b = 55\ mV$*,* $I_{sp} = 2\ nA$*,* $T = 4\ K$*. d) The recorded* $\frac{d^2I}{dV^2}$ *signal at every position. Green indicates a low signal and red indicates a high signal.*

mode and the N-O stretch mode are not measured in this experiment. This means that the coupling between the electrons on the molecule and these vibrations is so weak, that the inelastic intensity is less than the noise level. Whether one can observe certain vibrational modes is dictated by selection rules. These selection rules are as yet unknown. It could be possible that these vibrations can be measured if NO is deposited on another surface.

In order to calculate how CO molecules are adsorbed on a transition metal, Blyholder applies the general molecular orbital approach [22]. CO molecules are chemically comparable to NO molecules. It is assumed here that NO adsorbs in a similar manner. In

Table 4.1: *The expected vibrational modes of NO on Rh(111).*

Vibrational mode	*Energy [meV]*
frustrated translation	7.5^a - 11.5^b [20]
frustrated rotation	- ^{c}
Rh-NO stretch	45 [21]
N-O stretch	183^d - 202^e [21]

a) top site b) hollow site c) not found in literature
d) 0.1 L exposure e) 10 L exposure

an isolated NO molecule, an sp_z-hybrid orbital of the nitrogen atom combines with the p_z-orbital of the oxygen to produce a binding σ-bond[1]. The p_x- and p_y-orbitals of the nitrogen and oxygen atoms combine to produce two $\pi_{x,y}$-orbitals. This leaves a lone pair of electrons in the $2s$-orbital of the oxygen atom and a lone pair in a second sp_z-hybrid orbital of the carbon atom[2]. This last pair can form a coordinate bond[3] with a suitable acceptor orbital such as a d-orbital of a metal atom. This forms a σ-bond between the nitrogen atom and the metal atom. If only this σ-bond would be formed, a large formal negative charge[4] would be put on the metal atom. Therefore it is usually stated that back donation from a metal d-orbital to the antibonding π^*-molecular orbital on the NO molecule occurs to remove this excess negative charge. This π-donation involves placing electrons in a high energy antibonding orbital, but calculations show that these orbitals are still lower in energy than the metal d-orbitals [22]. This coordinate bond is a strong bond. The redistribution of charge into an antibonding orbital reduces the strength of the N-O bond, decreasing the N-O stretch frequency. The effect of this bond is not only on the N-O stretch vibration, but also on the other above mentioned vibrational modes.

Rhodium in its ground state has two holes in the $4d$-orbital, as opposed to Ag and Au that do have a completely filled $3d$- resp. $4d$-orbital. This means that this coordinate bond can be formed between NO and Rh, but not between NO and Ag or Au. To study how much the Rh affects the vibrations of NO, nitric oxide has been deposited on Ag and Au to compare the frequencies. Therefore STM-IETS is used instead of e.g. Raman spectroscopy or HREELS, because there might be different structures of NO on the substrate with different IETS spectra. The spatially resolved IETS spectra of STM-IETS differentiates between possible differences, where global IETS measurements average over them.

---

[1] A σ-orbital is an orbital which is symmetric for rotation about the interatomic axis.

[2] The eleventh electron goes into the antibonding orbital with the lowest energy, which is $\pi^*_{x,y}$ in the case of NO [23].

[3] A coordinate bond is a covalent chemical bond between two atoms that is produced when one atom shares a pair of electrons with another atom lacking such a pair.

[4] A formal charge is a partial charge on an atom in a molecule, assigned by assuming that electrons in a chemical bond are shared equally between atoms, regardless of relative electronegativity.

4.2 Au(111) and Ag(111): *sp*-surface states

It was expected that Au(111) and Ag(111) are good substrates to observe the deposited NO and to detect the vibrational frequencies, in particular the stretch frequency, which is around 150 meV. The cleaning procedure along with STM images of the clean substrates are presented in appendix A.

Even on a perfect surface, there is one macroscopic defect: the surface itself. The termination of a material with a surface leads to a change of the electronic band structure from the bulk material to the vacuum. In the weakened potential at the surface new electronic states can be formed, so called *surface states*. There are two types of surface states: Tamm surface states [24], named after 1958 Nobel Prize winner Igor Tamm, and Shockley surface states [25], named after 1956 Nobel Prize winner William Shockley. In all three noble metals (Cu, Ag and Au), the requirements for a Shockley-type surface state are met due to the *s*-*p*-orbital crossing in these materials [26]. In the case of Ag(111) these *sp*-surface states are visualized in figure 4.2. In the case of Au(111), they lead to *surface reconstruction*: the atoms at the surface of a crystal rearrange themselves to form a different structure than the bulk structure, which is fcc in the case of Ag and Au. This reconstruction can be visualized using STM and is shown in figure 4.3. Appendix A.1 goes more into the details of this reconstruction.

The surface states give rise to certain features in the local density of states (LDOS). The LDOS of Ag(111) at several positions is shown in figure 4.4. One can observe a peak around $V = -40$ mV. The same state around $E = -40$ meV is found in reference [27]. This spectrum shows clearly that there are many features in the LDOS of the bare metal, resulting in peaks in the $\frac{d^2I}{dV^2}$-spectrum, which is not shown here. These might cloud the vibrational features of NO on Ag(111), and therefore no spectroscopy of NO on Ag(111) is attempted. The same holds for Au(111). The LDOS of Au(111) has not been measured, but can be found in reference [28].

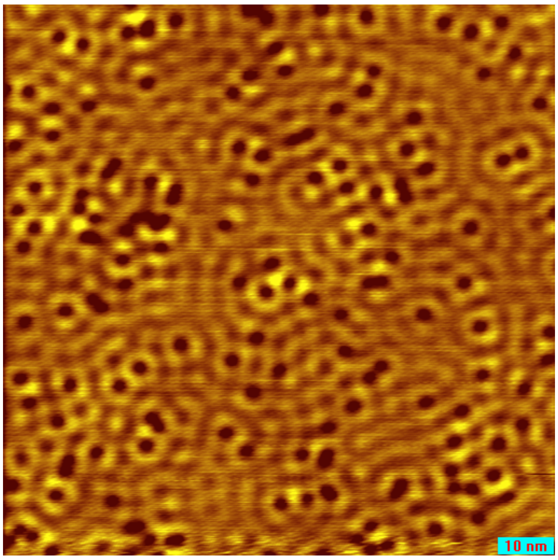

Figure 4.2: *A topography mapping of the surface states of Ag(111). The scan size is* 100×100 *nm*, $V_b = 10$ *mV*, $I_{sp} = 0.4$ *nA*, $T = 4$ *K.*

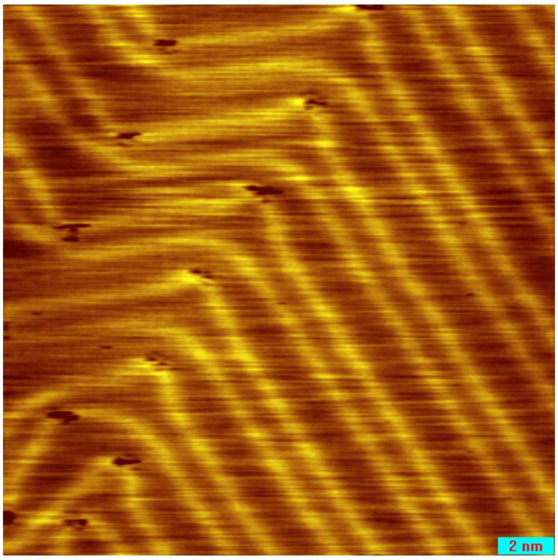

Figure 4.3: *A topography mapping of the herringbone reconstruction of Au(111). The scan size is* 20×20 *nm*, $V_b = 150$ *mV*, $I_{sp} = 0.5$ *nA*, $T = 77$ *K.*

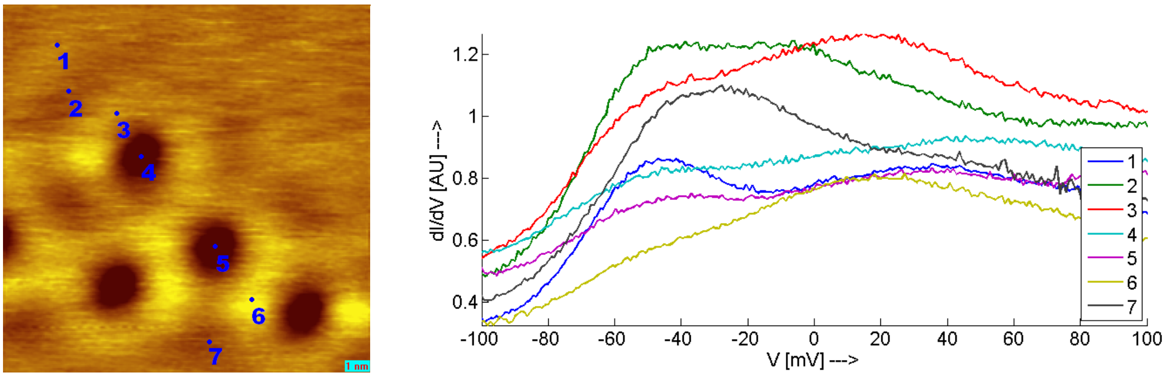

(a)

(b)

Figure 4.4: *a) Topographic mapping of the surface states of Ag(111). The scan size is* 15×15 *nm*, $V_b = 100$ *mV*, $I_{sp} = 0.4$ *nA*, $T = 4$ *K. b) The local density of states at seven different positions. The labels refer to the blue dots in figure a. The tunneling gaps were set with 100 mV sample bias and 0.4 nA tunneling current.*

4.3 Au(100)

The surface of Au(100) also shows a reconstruction pattern. The atoms in the surface layer are arranged in a close-packed rather than square arrangement. Since this surface layer does not match the underlying bulk layers, *buckling* takes place, which leads to height differences at the surface. Appendix A.3 goes more into the details of this reconstruction.

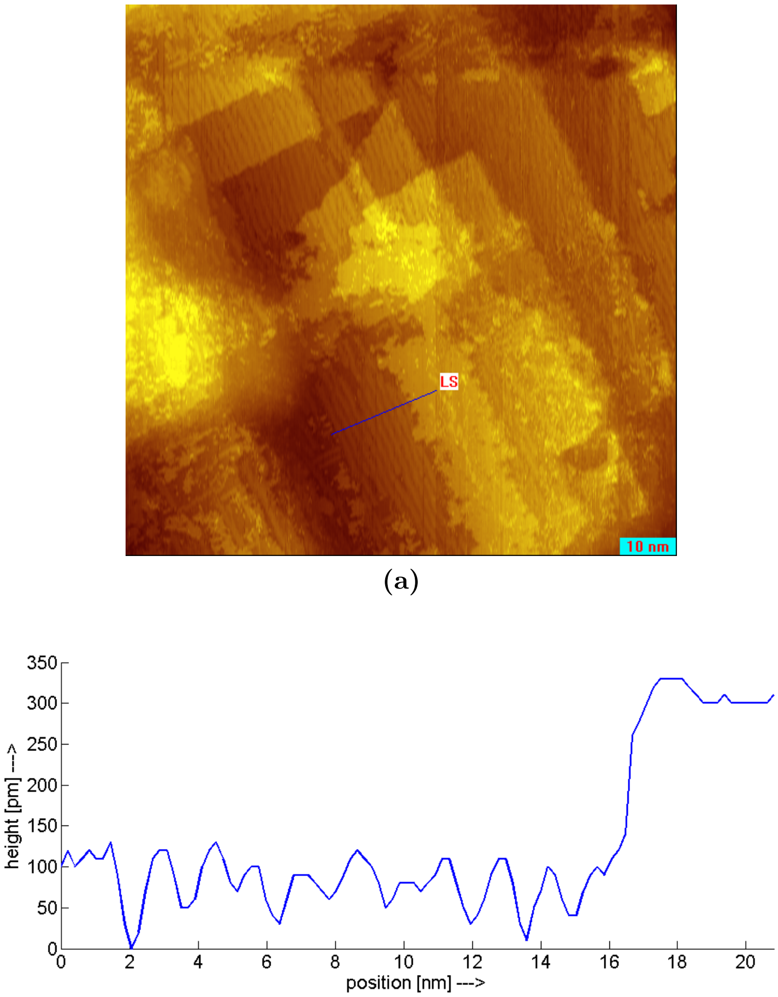

(a)

(b)

Figure 4.5: *a) Topography mapping of NO adsorbed on Au(100). The scan size is* 100×100 *nm,* $V_b = 100$ *mV,* $I_{sp} = 0.12$ *nA,* $T = 77$ *K. b) A line scan of an NO covered Au(100) substrate, taken at line LS in figure a.*

Figure 4.5a shows the Au(100) surface after deposition of NO. The temperature during deposition $T = 79$ K. A lot of covered areas are visible, but still some reconstruction rows are visible on the surface. A line scan over these reconstruction rows is given in figure 4.5b. Most of the surface however is unreconstructed. This is due to the adsorbates: the NO molecules induce a phase transition from a reconstructed surface to a bulk terminated

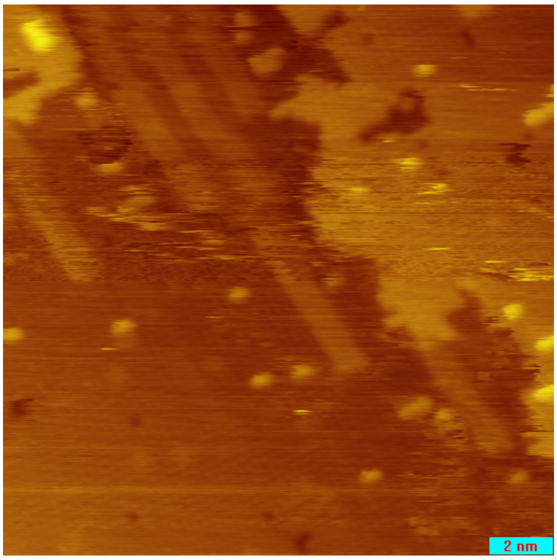

Figure 4.6: *A topography mapping of NO molecules on Au(100). In the bottom left part, the square arrangement can be identified. The rows in the top part of the image are reconstruction rows. The scan size is* 17.5×17.5 *nm,* $V_b = 100$ *mV,* $I_{sp} = 0.12$ *nA,* $T = 77$ *K.*

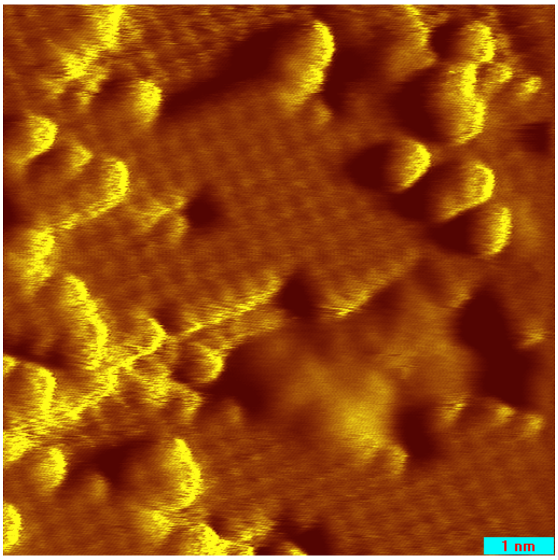

Figure 4.7: *A current mapping of NO molecules on Au(100). The square arrangement can easily be identified. The measured interatomic distance is* 0.30 ± 0.05 *nm, the theoretical interatomic distance is* $\frac{1}{2}\sqrt{2}a = 288$ *pm, where* $a = 410$ *pm is the bulk lattice constant for gold. The scan size is* 8×8 *nm,* $V_b = 8$ *mV,* $I_{sp} = 0.5$ *nA,* $T = 4$ *K. The temperature during deposition of this NO layer is* $T = 7$ *K.*

surface [29]. The square arrangement is shown in figures 4.6 and 4.7.

The 'blobs' in figures 4.6 and 4.7 are assumed to be (clusters of) NO molecules. These NO molecules are loosely bound to the Au(100) substrate. Even at $T = 4$ K, the molecules have sufficient energy to migrate over the surface, as is shown in figure 4.8.

As mentioned in section 3.3, many IETS measurements should be taken to be able to extract a stable IETS spectrum. If the NO is not fixed at one position, the drift correction explained in section 3.3, is unable to recognize two subsequent images, and hence two subsequent spectroscopies are not taken at the same position. In short: due to the high mobility of NO on Au(100), even at $T = 4$ K, no reliable IETS measurements can be obtained, and Au(100) is not a suitable substrate to investigate the IETS spectrum of NO on a noble metal.

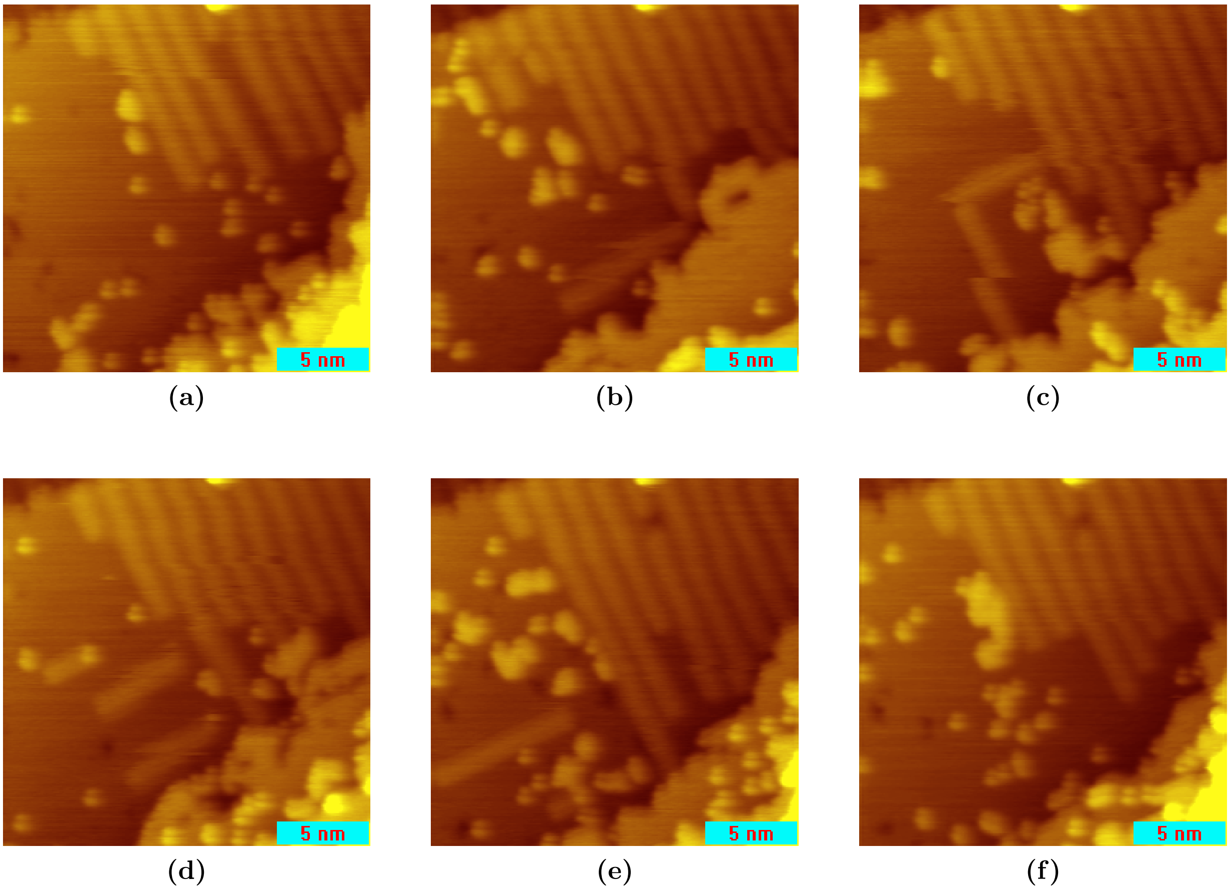

(a) **(b)** **(c)**

(d) **(e)** **(f)**

Figure 4.8: *Six subsequent topography mappings of NO molecules on Au(100). The rows are due to reconstruction of the Au(100) surface, the 'blobs' are (clusters of) NO molecules. The scan size is* 20×20 *nm,* $V_b = 100$ *mV,* $I_{sp} = 0.2$ *nA,* $T = 4$ *K. The time between the start of two subsequent images is* 46 *seconds.*

4.4 Ag(100)

Ag(100) has neither surface states nor surface reconstruction. An image of clean Ag(100) is shown in appendix A.4. There is no information available about the adsorption of NO molecules on Ag(100). There is however information about NO adsorption on Ag(111) [30, 31, 32]. NO molecules form dimers at temperatures as low as 40 K, at higher temperatures these dimers desorb. Although this is not necessarily the case for Ag(100), deposition takes place at $T = 8$ K to exclude any risks. Figure 4.9 shows three topographic images of NO molecules adsorbed on the Ag(100) substrate. There is no regular structure found of NO molecules on Ag(100). This might be due to the weaker bond, or due to the lower temperature during deposition. If the adsorbed NO molecules do not have sufficient thermal energy to move over the surface, they will not be able to form a structure.

Single-molecule IETS is performed over the NO adsorbates. Figure 4.10 shows the

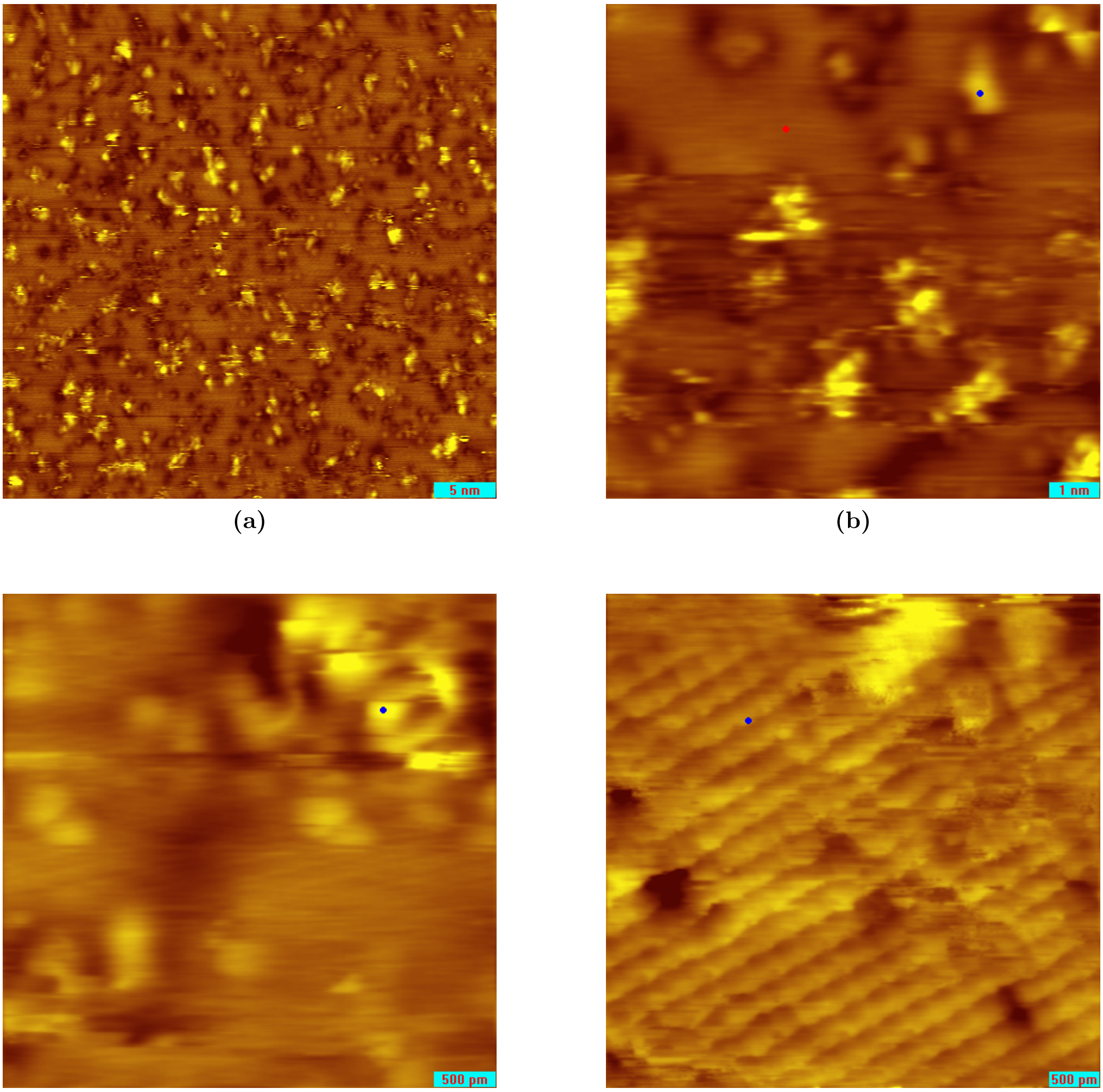

(a) **(b)** **(c)** **(d)**

Figure 4.9: *Topographic mappings of NO molecules adsorbed on Ag(100). a) The scan size is* 40×40 *nm,* $V_b = 100$ *mV,* $I_{sp} = 0.2$ *nA,* $T = 4$ *K. b) The scan size is* 10×10 *nm,* $V_b = 100$ *mV,* $I_{sp} = 0.2$ *nA,* $T = 4$ *K. c) The scan size is* 4×4 *nm,* $V_b = 100$ *mV,* $I_{sp} = 0.2$ *nA,* $T = 4$ *K. This image is taken with a modulation voltage of 12 mV enabled. d) The scan size is* 5×5 *nm,* $V_b = 470$ *mV,* $I_{sp} = 0.2$ *nA,* $T = 4$ *K.*

spectra obtained on top of an NO molecule and on clean Ag. For the spectrum taken over an NO molecule (figure 4.10a – position shown by blue dot in figure 4.9b), there is clearly an antisymmetric peak around ±25 mV. For the spectrum taken over another NO molecule (figure 4.10b – position shown by blue dot in figure 4.9c), this peak is around ±21 mV. For the spectrum taken over clean Ag (figure 4.10c – position shown by red dot in figure 4.9b) however, there is again an antisymmetric peak around ±21 mV. The properties of these peaks are summarized in table 4.2.

Table 4.2: *The parameters for the two peaks as shown in figure 4.10a (peaks 1 and 2), the two peaks as shown in figure 4.10b (peaks 3 and 4) and the two peaks as shown in figure 4.10c (peaks 5 and 6).*

Peak	*Center (mV)*	*Width (mV)*	*Peak*	*Center (mV)*	*Width (mV)*
1	-23.6	6.2	2	25.8	10.8
3	-20.8	4.8	4	21.6	10.5
5	-20.0	5.2	6	21.8	9.0

These antisymmetric peaks are associated with the frustrated rotation mode of NO on Ag, similar to reports about CO on Cu and on Ag. These vibrational modes are presented in table 4.3. A difference in energy between the negative and the positive peak, which is observed here, is reported in literature as well [35, 36]. The Ag-NO stretch, which is expected to be around $V = \pm 50$ mV, has not been observed, similar to reports about CO in literature [33, 35, 36]. This implies that the electron-phonon coupling is weak for this phonon mode. As already mentioned in section 4.1, the selection rules dictating the couplings are as yet unknown. The N-O stretch mode lies outside the used voltage range and could therefore not be observed.

Measuring an IETS spectrum with a bare tungsten tip over bare Ag, should show no features. The fact that the peak associated with the frustrated rotation of the NO molecule is also observed over clean Ag (figure 4.10c), suggests that there is an NO molecule on the tip as well. IETS spectra with molecule terminated tips have been reported in literature. Hahn and Ho [36] show a similar spectrum with CO on the tip over clean Ag(110). They show that a molecule on the tip leads to broadening and amplification of the signal. If the $\Delta\sigma/\sigma$-intensity of only this signal would be calculated, it would be over 50%. The peaks 1, 2, 3 and 4 in table 4.2 have intensities of 27%, 82%, 19% and 56% respectively. Therefore, the spectrum over bare Ag should be subtracted from the spectrum over an NO molecule in order to determine $\Delta\sigma/\sigma$-intensities. In figure 4.10 however, there is no clear difference between the spectra over bare Ag and over NO, so no intensities could be determined. Hahn and Ho do not state intensities as well.

There are more clues of the presence of a molecule on the tip. Literature [37, 9, 35, 36] shows that atomic resolution imaging is not achieved with a low current setpoint when using a bare tip, but is more easily achieved when using a molecule terminated tip. Atomic resolution in this work is seen on clean Ag(100) (figure A.8 in appendix A.4), as well as on

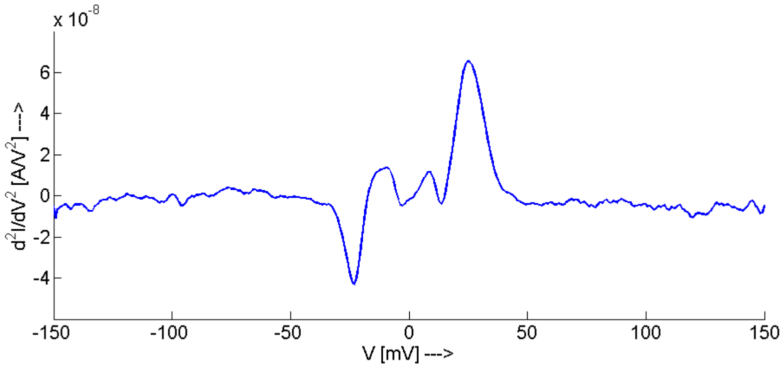

(a) Over NO molecule

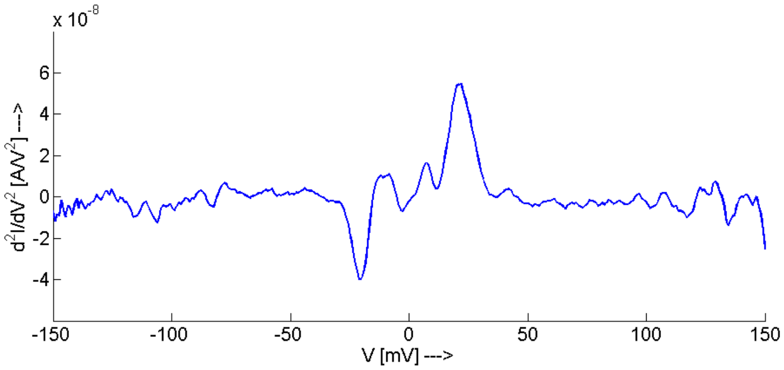

(b) Over NO molecule

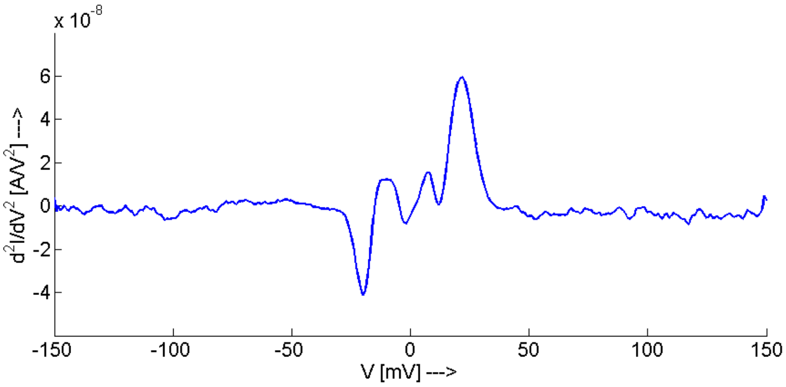

(c) Over bare Ag

Figure 4.10: *Averaged spectra measured on top of NO molecules adsorbed on Ag(100). Figure a is an average of 19 spectra, taken at the blue dot in figure 4.9b, figure b is an average of 7 spectra, taken at the blue dot in figure 4.9c, figure c is an average of 20 spectra, taken at the red dot in figure 4.9b.* $V_{mod} = 12\ mV$, $f_{mod} = 1.8\ kHz$, *lock in time constant is 3 ms, pre-sample delay is 30 ms. The tunneling gaps were set with 100 mV sample bias and 0.2 nA tunneling current. A possible offset on the measured voltage is subtracted. The antisymmetric peaks are fitted with Lorentzian peaks, for which the parameters are summarized in table 4.2.*

Table 4.3: *The reported vibrational modes of CO adsorbates on Cu and Ag substrates.*

Substrate	*Energy (meV)*	*Vibrational mode*	*Reference*
Cu(100)	4	Frustrated translation	[33]
Cu(100)	36	Frustrated rotation	[33]
Cu(100)	42	Cu-CO stretch	[33]
Cu(100)	256	C-O stretch	[33]
Cu(110)	4	Frustrated translation	[33]
Cu(110)	36	Frustrated rotation	[33]
Cu(110)	42	Cu-CO stretch	[33]
Cu(110)	257	C-O stretch	[33]
Cu(111)	4	Frustrated translation	[34]
Cu(111)	35	Frustrated rotation	[34]
Cu(111)	41	Cu-CO stretch	[34]
Ag(110)	7	Frustrated translation	[36]
Ag(110)	21	Frustrated rotation	[35, 36]
Ag(110)	267	C-O stretch	[37]

Ag(100) with adsorbed NO molecules (figure 4.9d). Figures 4.9b and 4.9c show no atomic resolution, probably due to instability of the tunnel junction. Literature [35, 36, 37, 38] also shows that a CO molecule is imaged as a depression when using a bare tip, but imaged as a protrusion when using a molecule terminated tip. In figure 4.9, all the molecules are imaged as a protrusion. However, it should be noted that when imaging NO on Rh(111), all the molecules show up as protrusions, regardless of the presence of a molecule on the tip.

The peaks associated with the NO molecule on the tip are at the same energies as the peaks associated with the NO molecule on Ag. This suggests that the tungsten tip is terminated with Ag due to the dipping procedure, described in section 2.1. In all previously mentioned references, the tip has always been dipped into the substrate as well. The NO molecule is then attached in the upright position, with the N attached to the tip. Vibrational energies are almost unchanged in this configuration. If the tip is not dipped into the substrate, it is tungsten terminated. There is still a probability that an NO molecule is bound to the tip. There are a lot of different configurations possible, three of which are illustrated in figure 4.11. All three configurations can be obtained with an fcc and a bcc tip, so there are in fact six different configurations illustrated. They lead to different vibrational modes, four of which have been calculated and are shown in table 4.4. No total energy calculations have been performed, so the configuration with the lowest energy is not known.

IETS spectra have been taken with an NO on W terminated tip. The results are

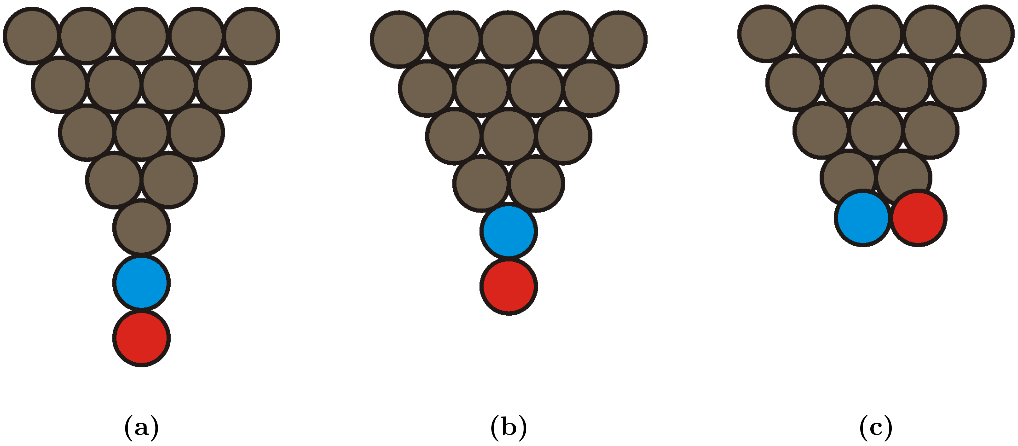

Figure 4.11: *Three different configurations of an NO molecule on a tip. The blue circles represent N atoms, the red circles represent O atoms. All tips can either be in fcc or bcc structure. a) The NO stands upright on the tip with the N-atom bound to a top site of the tip. b) The NO stands upright on the tip with the N-atom bound to a hollow site of the tip. c) The NO lies flat on the tip with the N-atom bound to a bridge site of the tip.*

Table 4.4: *The expected vibrational modes of NO on a tungsten tip. They are calculated with DFT calculations, performed by J.T. Cerdá.*

Conf.	*Tip structure*	*N-O stretch*	*Frustrated transl.*
		Energy (meV)	
4.11a	bcc	198	68
4.11c	bcc	114	56
4.11a	fcc	202	63
4.11b	fcc	167	48

shown in figure 4.12. The measured peaks around 56 mV and 100 mV have been fitted with Lorentzian peaks, for which the parameters are presented in table 4.5. The peaks are always positive at negative bias and always negative at positive bias. The positions suggest that the most likely configuration of NO on a W tip is the flat position, shown in figure 4.11c. Why sometimes only one vibration is measured is not understood, nor is the broadening that sometimes occurs and sometimes not.

Table 4.5: *The parameters for the two peaks as shown in figure 4.12a (peaks 1 and 2), the two peaks as shown in figure 4.12b (peaks 3 and 4) and the four peaks as shown in figure 4.12c (peaks 5, 6, 7 and 8) around 56 meV and 92 meV.*

Peak	*Center (mV)*	*Width (mV)*	*Peak*	*Center (mV)*	*Width (mV)*
1	- 53.4	41.8	2	58.3	44.4
3	-107.9	22.8	4	113.1	29.5
5	- 86.3	14.1	6	96.9	16.4
7	- 52.0	12.0	8	60.1	14.2

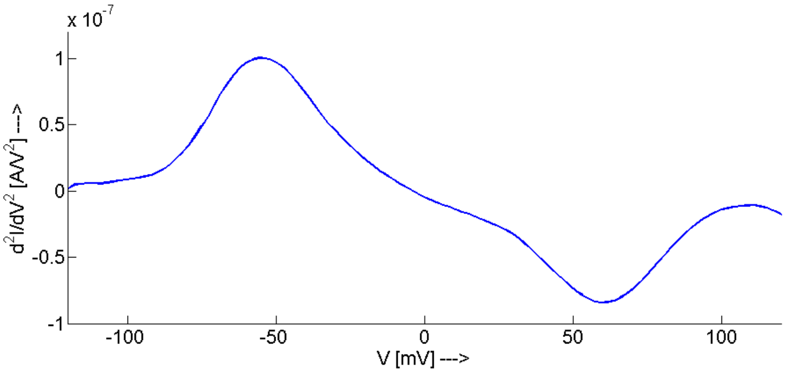

(a) Peaks around ±56 meV

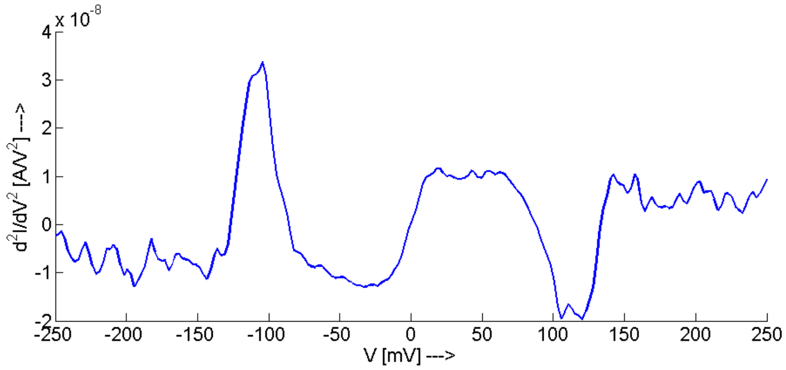

(b) Peaks around ±110 meV

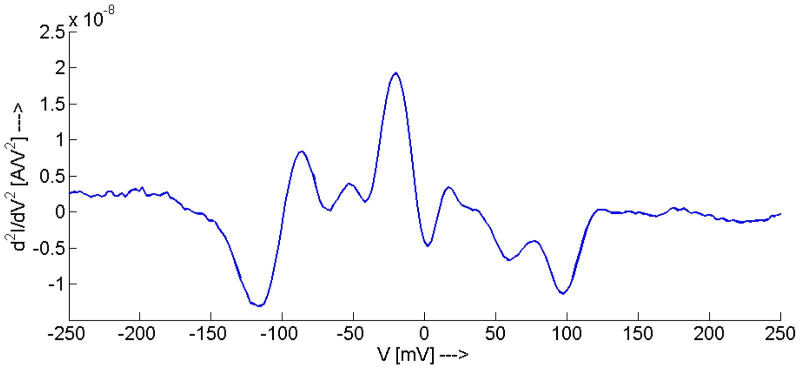

(c) Peaks around ±56 meV and around ±92 meV

Figure 4.12: *Averaged spectra measured with an NO on W terminated tip on top of clean substrates. Possible offsets on the measured voltage have been subtracted. The antisymmetric peaks are fitted with Lorentzian peaks, for which the parameters are summarized in table 4.5. a) An average of 50 spectra, taken at clean Ag(100) at the blue dot in figure 4.9d.* $V_{mod} = 12$ *mV*, $f_{mod} = 1.8$ *kHz, lock in time constant is 3 ms, pre-sample delay is 30 ms. The tunneling gap was set with 470 mV sample bias and 0.2 nA tunneling current. b) An average of 50 spectra, taken at clean Rh(111).* $V_{mod} = 14$ *mV*, $f_{mod} = 4.7$ *kHz, lock in time constant is 10 ms, pre-sample delay is 100 ms. The tunneling gap was set with 100 mV sample bias and 0.4 nA tunneling current. c) An average of 50 spectra, taken at clean Rh(111).* $V_{mod} = 14$ *mV*, $f_{mod} = 886$ *Hz, lock in time constant is 10 ms, pre-sample delay is 100 ms. The tunneling gap was set with 100 mV sample bias and 0.4 nA tunneling current.*

4.5 Conclusions

Section 4.2 shows that a surface without surface states is required to be able to perform IETS on adsorbates, otherwise vibrational features will be clouded by features in the LDOS of the substrate. Section 4.3 shows that NO molecules are mobile at $T = 4$ K on Au(100), so this will lead to the conclusion that from the four investigated substrate, Ag(100) is the only suitable substrate to perform IETS on NO.

During scanning and obtaining spectra, most of the times an NO molecule is adsorbed on the tip, due to presence of the tip in the neighborhood of the sample when NO is admitted. This can be identified by three characteristics. First, atomic resolution is more easily achieved with an NO terminated tip, where it is not achieved at low setpoint current with a bare tip. Second, NO is imaged as a protrusion with an NO terminated tip, where it is imaged as a depression with a bare tip. Last, with an NO molecule on the tip, the IETS spectrum shows vibrational features even on a clean part of the substrate.

Dipping of the tip leaves some Ag molecules on the tip. When an NO molecule adsorbs to this Ag-covered tip, the most likely position is the upright position with the N atom bound to the Ag, just as at the substrate. The IETS spectrum over a single molecule is then the same as one over the bare metal, so no difference spectra can be presented. When the tip is not dipped, the end atoms of the apex are tungsten atoms. When an NO molecule adsorbs to this W tip, the most likely position is the flat position. The IETS spectrum over a single molecule is then mixed with the spectrum of a molecule on the tip.

In order to perform IETS on a single molecule adsorbed on a substrate, a clean tip is required. Therefore the experimental setup needs to be revised, so it is possible to admit NO molecules to the substrate, without the tip being in the neighborhood. The absence of a molecule on the tip should be stable and be identified by the three above mentioned characteristics, before performing IETS.

Chapter 5

Simulations - Non resonant case

To predict the influence of certain parameters, IETS spectra have also theoretically been studied. These studies can be roughly divided into three groups: works based on scattering theory, works based on many-body physics and works using kinetic equations. Reference [16] reviews several theoretical works on this subject.

Inelastic electron tunneling involving vibrating molecules in vacuum can be treated exactly using scattering theory. However, the scattering cross-sections calculated in vacuum do not take into account the Fermi statistics of the electrons in the metal leads. In some studies, vacuum-based transmission coefficients are simply multiplied by Fermi population factors to take this into account. Though this approach leads to good practical results in the weak electron-phonon coupling, the results are not reliable in the intermediate to strong coupling. On top of that, it does not become exact when a small parameter goes to zero and it disregards the effect of the non equilibrium electronic system on the phononic system.

Approaches based on many-body physics methods are exact, though in practice simplifications have to be made to be able to calculate the system. The most used many-body method is the non equilibrium Green's function method (NEGF), which will be explained below. One possible simplification is to disregard Fermi population in the leads; the results are then equivalent to scattering theory approaches. Another approach within the NEGF formalism is to take only into account a few diagrams. When only the Hartree and Fock diagrams are taken into account, the approximation is called the Born approximation. When an infinite number of Hartree and Fock diagrams is taken into account, the approximation is called the self consistent Born Approximation. Other approaches are the linked cluster expansion, the equation of motion approach, Hamiltonian transformations or numerical renormalization group methods.

Strong electron-phonon coupling situations are often treated using kinetic equations, based on the assumption that the tunneling traversal time (see section 2.4) is long relative to the dephasing time due to electron-electron or electron-phonon interactions. This assumption holds if the molecule is only weakly coupled to the leads. Within this approach, electrons can hop onto and out of the bridge. The charge on the bridge is modeled using a classical or quantum mechanical harmonic oscillator that couples to the electrons.

The NEGF method is the most general method of the above described approaches. It is this method, together with the SCBA, which is used in the case of weak electron-phonon coupling throughout this thesis. This weak coupling limit is covered in this chapter. The next chapter will cover the intermediate to strong electron-phonon coupling. It uses therefore a Lang-Firsov transformation to the Hamiltonian within the NEGF framework. In both situations, the aim is to calculate IETS spectra with the given coupling parameters. Especially the influence of raising the phonon occupation at a certain frequency is evaluated.

This chapter explains first the physical model in section 5.1, which is the same in both regimes. Next, the transition from physical model to mathematical model using the Green's functions is explained in section 5.2. The assumptions and limitations of the model used are given in section 5.3. It continues with the calculation scheme used in the computer simulation in section 5.4 and some technical details about the simulation in section 5.5. The process of raising the phonon occupation is described in section 5.6. Finally in section 5.7 the numerical results are presented and discussed.

The model used in this and the subsequent chapter makes use of the second quantization. A perfect introduction to this subject is found in [39]. This chapter closely follows the work of [40].

5.1 The physical model

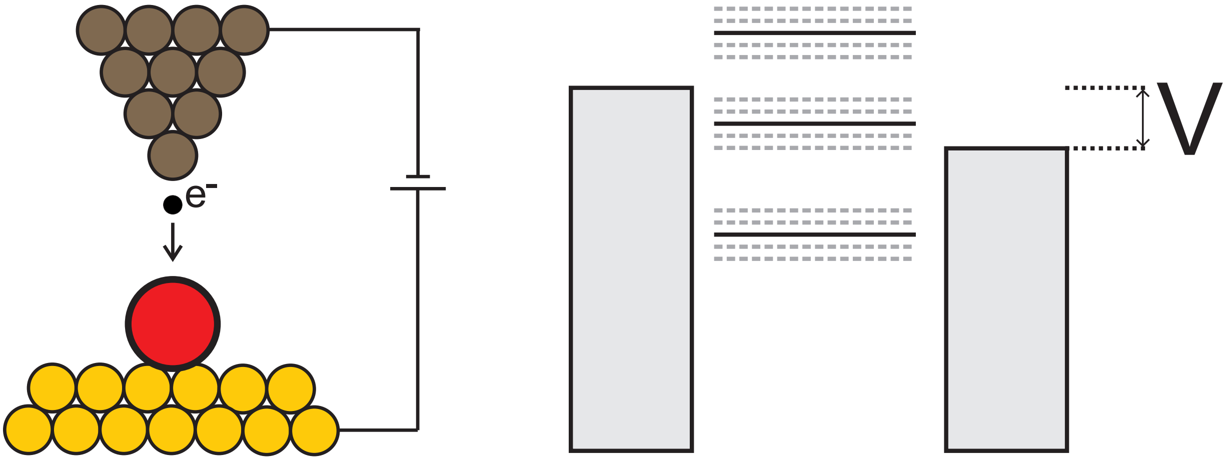

(a) (b)

Figure 5.1: *a) A schematic drawing of the system under investigation, with an STM tip, a gold substrate, a molecule on top of the substrate and a voltage applied between tip and substrate. b) Energy diagram of the system, with a left and right lead with continuous electronic states, several discrete electronic levels (solid lines) in the molecular bridge and the corresponding vibronic states (dashed lines). Vibronic states are one or a multiple of phonon energies lower or higher than the electronic states.*

Figure 5.1 shows the system under investigation. The tip and substrate are represented by a left and a right lead, which are free electron reservoirs in thermal equilibrium and coupled through a bridging molecular system. Molecular motions are described as phonons with energy $\hbar\omega$ and are divided into two groups. The primary phonons interact with the electronic system, whereas the secondary phonons only couple to the primary phonons. The secondary phonons represent the environment, and is assumed to be in thermal equilibrium. They are referred to as the thermal bath. The primary phonons are therefore driven by the non equilibrium electronic system, while interchanging energy with the thermal bath. Electron-phonon interaction in the leads is disregarded.

The next list summarizes the involved electron and phonon states and their interactions.

- Electron states in left and right lead, which are labeled by $k \in L, R$, with corresponding creation (annihilation) operators $\hat{d}_k^\dagger$ ($\hat{d}_k$) and energies ϵ_k. Later on, the wide band limit is used, which means that the electronic levels in the leads form a continuous band with a flat density of states.

- Electron states in the molecular bridge, which are labeled by i, with corresponding creation (annihilation) operators $\hat{c}_i^\dagger$ ($\hat{c}_i$) and interstate coupling t_{ij}, where $t_{ii} = E_i$ is the energy of electronic state i.

- Primary phonon states in the molecular bridge, which are labeled by l, with corresponding creation (annihilation) operators $\hat{a}_l^\dagger$ ($\hat{a}_l$) and energies $\hbar\Omega_l$. Primary phonon states are phonon states which couple to electron states.

- Secondary phonon states in the molecular bridge, which are labeled by m, with corresponding creation (annihilation) operators $\hat{b}_m^\dagger$ ($\hat{b}_m$) and energies $\hbar\omega_m$. Secondary phonon states are phonon states that do not couple to electron states.

- Coupling between electron states i in the molecular bridge and the leads $k \in L, R$, denoted by V_{ki}.

- Coupling between the electron states i and the primary phonon states l in the molecular bridge, denoted by M_i^l.

- Coupling between the primary phonon states l and the secondary phonon states m in the molecular bridge, denoted by U_m^l.

This leads to a zero-order Hamiltonian as in equation 5.2 and an interaction Hamiltonian as in equation 5.3.

$$\hat{H} = \hat{H}_0 + \hat{H}_1 \tag{5.1}$$

$$\hat{H}_0 = \sum_{i,j} t_{ij}\hat{c}_i^\dagger\hat{c}_j + \sum_{k\in L,R} \epsilon_k \hat{d}_k^\dagger \hat{d}_k + \sum_l \Omega_l \hat{a}_l^\dagger \hat{a}_l + \sum_m \omega_m \hat{b}_m^\dagger \hat{b}_m \tag{5.2}$$

$$\hat{H}_1 = \sum_{k\in L,R;i} (V_{ki}\hat{d}_k^\dagger \hat{c}_i + V_{ik}\hat{c}_i^\dagger \hat{d}_k) + \sum_{l,i} M_i^l \hat{A}_l \hat{c}_i^\dagger \hat{c}_i + \sum_{l,m} U_m^l \hat{A}_l \hat{B}_m \tag{5.3}$$

$\hat{A}$ and $\hat{B}$ are phonon displacement operators, defined as $\hat{A}_l = (\hat{a}_l^\dagger + \hat{a}_l)$ and $\hat{B}_m = (\hat{b}_m^\dagger + \hat{b}_m)$. In other works, they are often written as $\hat{Q}_a$ and $\hat{Q}_m$ respectively.

5.2 The mathematical model

In general, the eigenstates of the Hamiltonian of equation 5.1 cannot be calculated exactly. The properties of a system that is described by a Hamiltonian $\hat{H}$ which may not be solved exactly, are generally deduced using Green's functions. This approach is called the non equilibrium Green's function (NEGF) approach. In short, the approach is to choose a $\hat{H}_0$ such that $\hat{H} = \hat{H}_0 + \hat{V}$, where $\hat{H}_0$ is a Hamiltonian that may be solved exactly and $\hat{V}$ is the rest of the total Hamiltonian, which effects are small. Then start with a system completely described by $\hat{H}_0$, introduce $\hat{V}$ and see how this changes the system that was understood.

This section briefly introduces the NEGF approach that is used in the remainder of this thesis. For a more elaborate description of this approach, see [41].

The mathematical objects used within the NEGF formalism are the one-particle Green's functions. These are defined on the Keldysh contour [42] (see figure 5.2) by

$$G_{ij}(\tau,\tau') = -i\langle \hat{T}_c \hat{c}_i(\tau)\hat{c}_j^\dagger(\tau')\rangle \tag{5.4}$$

$$D_{ij}(\tau,\tau') = -i\langle \hat{T}_c \hat{A}_i(\tau)\hat{A}_j(\tau')\rangle \tag{5.5}$$

$\hat{T}_c$ is the time ordering operator which arranges the operators after it with the earliest time on the Keldysh contour to the right.

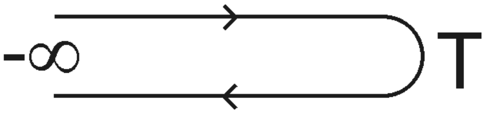

Figure 5.2: *The Keldysh contour is the timeline in which time goes from $-\infty$ to time T and back to $-\infty$, where eventually $T \to \infty$.*

The Green's function is often called a propagator. This means that the Green's function can be physically interpreted as follows: $iG_{ij}(\tau,\tau')$ is the probability amplitude that, given an electron in state j at time τ', this electron is in state i at time τ, where τ is not necessarily a later time as τ'. A similar interpretation can be given to $D_{ij}(\tau,\tau')$.

These Green's functions satisfy the following Dyson equations, which are visualized in figure 5.3,

$$G_{ij}(\tau,\tau') = G_{0,ij}(\tau,\tau') + \sum_{k,l} \int_c d\tau_1 \int_c d\tau_2 G_{0,il}(\tau,\tau_1)\Sigma_{lk}(\tau_1,\tau_2)G_{kj}(\tau_2,\tau') \tag{5.6}$$

$$D_{ij}(\tau,\tau') = D_{0,ij}(\tau,\tau') + \sum_{k,l} \int_c d\tau_1 \int_c d\tau_2 D_{0,il}(\tau,\tau_1)\Pi_{lk}(\tau_1,\tau_2)D_{kj}(\tau_2,\tau') \tag{5.7}$$

where G_0 and D_0 are the electron and phonon Green's functions of the unperturbed system respectively and Σ and Π are the electron and phonon self energies respectively. The self energies contain all the interactions of the system.

Figure 5.3: *The Dyson equation 5.6 in Feynman diagrams. The double lines represent the propagators for electrons in the interacting system, the single lines represent the non-interacting electron propagators and the circle V represents the electron self energy, which contains all the interactions. A similar diagram can be drawn to visualize Dyson equation 5.7*

The Dyson equations can be physically interpreted as follows: the probability amplitude to go from state j at time τ' to state i at time τ in a perturbed system is equal to the probability amplitude to go from state j at time τ' to state i at time τ in an unperturbed system plus the probability amplitude to go from state j at time τ' to state k at time τ_2 in a perturbed system, have interactions between times τ_2 and τ_1 at the scatterer Σ to go from state k to state l and finally go from state l at time τ_1 to state i at time τ in an unperturbed system, integrated over all possible times τ_1 and τ_2 and over all possible intermediate states k and l.

The Green's functions and self energies can be used to calculate many one-particle characteristics of the system under investigation. In particular the current through the system is calculated using equation 5.36 and electron or phonon density of states using equation 5.37. Notice that the Green's functions and the self energies are matrices, where each element is a function of the two times τ and τ'. The size of the electronic (phononic) Green's function and self energy matrices is equal to the number of electronic (phononic) states in the bridge. The elements, which are labeled with i, j, are denoted with either $G_{ij}(\tau,\tau')$ and $D_{ij}(\tau,\tau')$ or $[G(\tau,\tau')]_{ij}$ and $[D(\tau,\tau')]_{ij}$.

These Dyson equations are projected from the Keldysh contour onto the real time axis, resulting in equations for the projected Green's functions and self energies. There are four possible situations.

- τ' is on the upper branch of the Keldysh contour and τ is on the lower branch of the Keldysh contour. Now $\tau' < \tau$ independent of their values and the time ordering operator in equation 5.4 arranges the Green's function as in equation 5.8. This is called the greater projection.
- τ' is on the lower branch of the Keldysh contour and τ is on the upper branch of the Keldysh contour. Now $\tau' > \tau$ independent of their values and the time ordering operator in equation 5.4 arranges the Green's function as in equation 5.9. This is called the lesser projection.
- Both τ' and τ are on the upper branch of the Keldysh contour. Now time ordering on the Keldysh contour is identical to time ordering in real time space. The time

ordering operator in equation 5.4 arranges the Green's function as in equation 5.10. This is called the time ordered projection.

- Both τ' and τ are on the lower branch of the Keldysh contour. Now time ordering on the Keldysh contour is the opposite of time ordering in real time space. The time ordering operator in equation 5.4 arranges the Green's function as in equation 5.11. This is called the anti time ordered projection.

$$\begin{aligned}
[G^{>}(\tau,\tau')]_{ij} &= -i\langle\hat{c}_i(\tau)\hat{c}_j^{\dagger}(\tau')\rangle && (5.8)\\
[G^{<}(\tau,\tau')]_{ij} &= i\langle\hat{c}_j^{\dagger}(\tau')\hat{c}_i(\tau)\rangle && (5.9)\\
G^{t}(\tau,\tau') &= \theta(t_1-t_2)G^{>}(\tau,\tau')+\theta(t_2-t_1)G^{<}(\tau,\tau') && (5.10)\\
G^{\bar{t}}(\tau,\tau') &= \theta(t_2-t_1)G^{>}(\tau,\tau')+\theta(t_1-t_2)G^{<}(\tau,\tau') && (5.11)
\end{aligned}$$

It is convenient and commonly applied to define two different projections of the Green's functions, which are linear combinations of these four. They are called the retarded projection (equation 5.12) and the advanced projection (equation 5.13).

$$\begin{aligned}
G^{r}(\tau,\tau') &= G^{t}(\tau,\tau')-G^{<}(\tau,\tau') && (5.12)\\
&= G^{>}(\tau,\tau')-G^{\bar{t}}(\tau,\tau')\\
&= \theta(\tau-\tau')\left(G^{>}(\tau,\tau')+G^{<}(\tau,\tau')\right)
\end{aligned}$$

$$\begin{aligned}
G^{a}(\tau,\tau') &= G^{t}(\tau,\tau')-G^{>}(\tau,\tau') && (5.13)\\
&= G^{<}(\tau,\tau')-G^{\bar{t}}(\tau,\tau')\\
&= \theta(\tau'-\tau)\left(G^{>}(\tau,\tau')+G^{<}(\tau,\tau')\right)
\end{aligned}$$

The exact analogue projections are introduced for the phonon Green's function $D(\tau,\tau')$. In the remainder of this chapter, only equations for the greater, lesser and retarded projections of Green's functions and self energies are given. The advanced projection of a Green's function or self energy is always the conjugate transpose of the corresponding retarded projection.

The system is treated as a steady-state system, which means that all two-time quantities depend only on the time difference. Using this fact, it is possible to transform these two-variable Green's functions and self energies into one-variable Green's functions and self energies with a Fourier transformation. The Fourier variable associated with the Green's function and self energy for electrons is denoted by E, the Fourier variable associated with the Green's function and self energy for phonons is denoted by ω. The resulting Green's functions and self energies are again matrices, where each element is a function of either E or ω. The corresponding equations for the Green's functions are the Dyson equations for the retarded Green's functions,

$$\begin{aligned} G^r(E) &= \frac{1}{[G_0^r(E)]^{-1} - \Sigma^r(E)} && (5.14) \\ D^r(\omega) &= \frac{1}{[D_0^r(\omega)]^{-1} - \Pi^r(\omega)} && (5.15) \end{aligned}$$

and the Keldysh equations for the lesser and greater Green's functions,

$$\begin{aligned} G^<(E) &= G^r(E)\Sigma^<(E)G^a(E) && (5.16) \\ G^>(E) &= G^r(E)\Sigma^>(E)G^a(E) \end{aligned}$$

$$\begin{aligned} D^<(\omega) &= D^r(\omega)\Pi^<(\omega)D^a(\omega) && (5.17) \\ D^>(\omega) &= D^r(\omega)\Pi^>(\omega)D^a(\omega). \end{aligned}$$

The total self energy term comprises all the individual interactions, which are simply added. This leads to equation 5.18 for the self energy for the electrons and to equation 5.19 for the self energy for the phonons for all four individual projections.

$$\begin{aligned} \Sigma_{ij}(E) &= \Sigma_{ij}^L(E) + \Sigma_{ij}^R(E) + \Sigma_{ij}^{ph}(E) && (5.18) \\ \Pi_{ij}(\omega) &= \Pi_{ij}^{ph}(\omega) + \Pi_{ij}^{el}(\omega) && (5.19) \end{aligned}$$

The components of the electronic self energy Σ are the self energies associated with the coupling to the left and right leads (Σ^L and Σ^R) and the self energy associated with the coupling to the primary phonons (Σ^{ph}). In the wide band limit, Σ^L and Σ^R can be obtained exactly. The real parts of the retarded and advanced self energies are negligible, while the imaginary parts are energy independent constants [40], as in equation 5.20,

$$\begin{aligned} \Sigma_K^r &= -\frac{i}{2}\Gamma^K && (5.20) \\ \Sigma_K^< &= i\Gamma^K f_K(E) \\ \Sigma_K^> &= -i\Gamma^K(1 - f_K(E)) \end{aligned}$$

where $K = L$ for the left lead and $K = R$ for the right lead. $f_K(E)$ is the Fermi-Dirac distribution function, equation 5.21, which is dependent on the lead's chemical potential μ_K, that subsequently depends on the applied bias V, as can be seen in equation 5.38.

$$f_K(E) = \left(\exp\left[\frac{E - \mu_K}{k_B T}\right] + 1\right)^{-1} \qquad (5.21)$$

Γ^K is the level-width matrix caused by hybridizations between the left or right lead and the bridge. They are defined by

$$[\Gamma^K(E)]_{ij} = 2\pi \sum_{k\in K} V_{ik}V_{kj}\delta(E-E_k) \tag{5.22}$$

and are independent of energy in the wide band limit. For the electron self energy due to coupling to the phonons, only the lowest order (in electron-phonon coupling M) self energies are taken into account. These are shown in figure 5.4, which lead to equation 5.23 for Σ^{ph}. An excellent review on Feynman diagrams is given in reference [43].

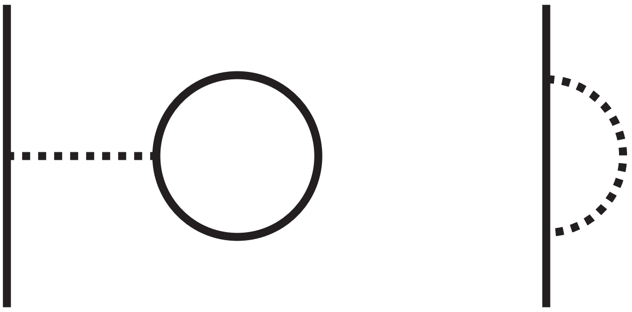

Figure 5.4: *Feynman diagrams for electron self energies. The solid lines represent electron propagators, the dotted lines represent phonon propagators in the unperturbed system. The left diagram is called the Hartree diagram and leads to the last term in the first equation of 5.23. The right diagram is called the Fock diagram and leads to the first three terms in the first equation of 5.23, which are three different projections of this diagram.*

$$\begin{aligned}
[\Sigma^r_{ph}(E)]_{ij} &= i\sum_{k_1,k_2} M_i^{k_1}M_j^{k_2}\int\frac{d\omega}{2\pi}\Big[D^<_{k_1k_2}(\omega)G^r_{ij}(E-\omega) \\
&\quad + D^r_{k_1k_2}(\omega)G^<_{ij}(E-\omega) + D^r_{k_1k_2}(\omega)G^r_{ij}(E-\omega)\Big] \\
&\quad + \delta_{ij}\sum_{k_1,k_2,i'} M_i^{k_1}M_{i'}^{k_2}n^{el}_{i'}D^r_{k_1k_2}(\omega=0) \\
[\Sigma^<_{ph}(E)]_{ij} &= i\sum_{k_1k_2} M_i^{k_1}M_j^{k_2}\int\frac{d\omega}{2\pi}D^<_{k_1k_2}(\omega)G^<_{ij}(E-\omega) \\
[\Sigma^>_{ph}(E)]_{ij} &= i\sum_{k_1k_2} M_i^{k_1}M_j^{k_2}\int\frac{d\omega}{2\pi}D^>_{k_1k_2}(\omega)G^>_{ij}(E-\omega)
\end{aligned} \tag{5.23}$$

Here $n^{el}_i = \rho_{ii}$, where ρ_{ij} is defined by equation 5.24. The Hartree term is omitted in the remainder of this chapter, because the density of states for phonons with $\omega = 0$ is considered zero.

$$\rho_{ij} = -i\int\frac{dE}{2\pi}G^<_{ij}(E) \tag{5.24}$$

Integration over ω from $(-\infty, \infty)$ is required. Positive frequencies refer to processes where a phonon is first absorbed and subsequently re-emitted, where negative frequencies refer to processes where a phonon is first emitted and then reabsorbed.

The components of the phonon self energy Π are the self energy associated with the coupling to the secondary phonons (Π^{ph}) and the self energy associated with the coupling to the electronic system (Π^{el}). In the wide band limit, Π^{ph} can be obtained exactly, using the fact that the thermal bath is in thermal equilibrium. Again, the real parts of the retarded and advanced projections are negligible, while the imaginary parts are energy independent constants [40],

$$\begin{aligned} \Pi^r_{ph}(\omega) &= -\frac{i}{2}\,\mathrm{sgn}(\omega)\gamma(\omega) \qquad (5.25)\\ \Pi^<_{ph}(\omega) &= -i\gamma(\omega)F(\omega) \\ \Pi^>_{ph}(\omega) &= -i\gamma(\omega)F(-\omega). \end{aligned}$$

The function $F(\omega)$ is defined as in equation 5.26. γ is the level-width matrix caused by hybridizations between the primary phonon states and the secondary phonon states. It is defined by equation 5.27 and is independent of energy in the wide band limit.

$$F(\omega) = \begin{cases} N(|\omega|) & \text{if } \omega > 0 \\ 1 + N(|\omega|) & \text{if } \omega < 0 \end{cases} \tag{5.26}$$

$$\gamma_{ij}(\omega) = 2\pi \sum_m U^i_m U^j_m \delta(\omega - \omega_m) \tag{5.27}$$

$N(\omega)$ is the Bose-Einstein distribution function,

$$N(\omega) = \left(\exp\left[\frac{\omega}{k_B T}\right] - 1\right)^{-1}. \tag{5.28}$$

For the phonon self energy due to coupling to the electrons, only the lowest order (in electron-phonon coupling M) self energy is taken into account. This is shown in figure 5.5, which leads to equation 5.29 for Π^{el}.

$$\begin{aligned} [\Pi^r_{el}(\omega)]_{ij} &= -i\sum_{i_1,i_2} M^i_{i_1} M^j_{i_2} \int \frac{dE}{e\pi}\Big[G^<_{i_1 i_2}(E) G^a_{i_2 i_1}(E-\omega) \qquad (5.29)\\ &\quad + G^r_{i_1 i_2}(E) G^<_{i_2 i_1}(E-\omega)\Big] \\ [\Pi^<_{el}(\omega)]_{ij} &= -i\sum_{i_1 i_2} M^i_{i_1} M^j_{i_2} \int \frac{dE}{2\pi} G^<_{i_1 i_2}(E) G^>_{i_2 i_1}(E-\omega) \\ [\Pi^>_{el}(\omega)]_{ij} &= -i\sum_{i_1 i_2} M^i_{i_1} M^j_{i_2} \int \frac{dE}{2\pi} G^>_{i_1 i_2}(E) G^<_{i_2 i_1}(E-\omega) \end{aligned}$$

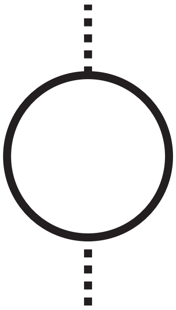

Figure 5.5: *Feynman diagram for phonon self energy. The solid line represents an electron propagator, the dotted lines represent phonon propagators in the unperturbed system. The process drawn is called electron-hole pair excitations and leads to the two terms in the first equation of 5.29, which are two different projections of this diagram.*

5.3 Assumptions and limitations

The above described method is based on perturbation theory, with the electron-phonon coupling M as the perturbation parameter. This is only valid if M is small compared to the inverse traversal time (equation 2.4). Weak electron-phonon coupling therefore imposes:

$$|\frac{M}{\sqrt{\Delta E^2 + \Gamma^2}}| \ll 1 \tag{5.30}$$

An assumption tacitly made is that under steady state conditions, the metal leads are in thermal equilibrium. This assumption is valid if the molecule-lead coupling is not large. If the molecule-lead coupling is so strong that the electron transmission probability is nearly 1, the electrons in the negatively biased lead of energies in the conduction window (i.e. between the Fermi energy of the left lead and the Fermi energy of the right lead) may be depleted. This gives rise to an increased reflection at the onset $eV = \hbar\Omega$, otherwise prohibited by the Fermi exclusion principle. This results in a negative step in the contribution, often seen in point contact spectroscopy (see e.g. [13, 14, 15]).

Since assumption 5.30 must hold to use perturbation theory and Γ must be small to use leads in thermal equilibrium, ΔE must be large, which implies that this model is only valid for the non resonant regime. The usage of this model in the resonant regime is valid only if electron-phonon coupling is very weak, but then no essential inelastic features can be studied.

5.4 Calculation scheme

From equations 5.14, 5.15, 5.16 and 5.17 it is clear that the Green's functions $G(E)$ and $D(\omega)$ are functions of the self energies $\Sigma(E)$ and $\Pi(\omega)$. From equations 5.18, 5.19, 5.23 and 5.29 it is clear that the self energies $\Sigma(E)$ and $\Pi(\omega)$ are functions of the Green's functions $G(E)$ and $D(\omega)$. The equations in section 5.2 provide a self-consistent calculation scheme that takes an infinite number of non crossing diagrams into account to calculate the Green's functions and self energies. This means that the diagrams in figures 5.4 and 5.5 can be infinitely repeated in any order, but no other diagrams are taken into account. This is called the self-consistent Born approximation (SCBA). The calculation consists of the following steps.

Step 1: grids

The equations in section 5.2 involves integration over the electronic energy E and the frequency variable ω. These are done using numerical grids with a fixed minimum, maximum and point density. The range between minimum and maximum is chosen large enough to span the essential energy and frequency ranges, but small enough to keep calculation time under control. The grid step size is chosen smaller than the spectral widths of the functions, but large enough to keep calculation time under control. Details on the choices made are provided in section 5.7.

Step 2: initial values

Before the iteration starts, a value is required for either the Green's function or the self energy. It makes sense to choose the Green's functions of the electrons and the primary phonons that are zeroth order in electron-phonon interaction. This means that for the zero-order electron self energy, only coupling to the leads is taken into account, and for the zero-order phonon self energy, only coupling to the thermal bath is taken into account,

$$\begin{aligned} \Sigma_0(E) &= \Sigma^L(E) + \Sigma^R(E) & (5.31) \\ \Pi_0(\omega) &= \Pi^{ph}(\omega). & (5.32) \end{aligned}$$

This leads to equation 5.33 for the zero-order Green's function for electrons and to equation 5.34 for the zero-order Green's function for primary phonons.

$$\begin{aligned} G_0^r(E) &= \frac{1}{\bar{E} - t + \frac{i}{2}\Gamma(E)} & (5.33) \\ G_0^<(E) &= \frac{i f_L(E)\Gamma^L(E) + i f_R(E)\Gamma^R(E)}{(\bar{E} - t)^2 + (\frac{1}{2}\Gamma(E))^2} \\ G_0^>(E) &= \frac{-i(1 - f_L(E))\Gamma^L(E) - i(1 - f_R(E))\Gamma^R(E)}{(\bar{E} - t)^2 + (\frac{1}{2}\Gamma(E))^2} \end{aligned}$$

$$\begin{aligned} D_0^r(\omega) &= \frac{1}{\bar{\omega} - \Omega + \frac{i}{2}\gamma(\omega)} - \frac{1}{\bar{\omega} + \Omega + \frac{i}{2}\gamma(\omega)} & (5.34) \\ D_0^<(\omega) &= F(\omega)\,[D_0^r(\omega) - D_0^a(\omega)]\,\mathrm{sgn}(\omega) \\ D_0^>(\omega) &= F(-\omega)\,[D_0^r(\omega) - D_0^a(\omega)]\,\mathrm{sgn}(\omega) \end{aligned}$$

Here, $\bar{E}$ in the denominator of equation 5.33 stands for $E \cdot I$, where I is the identity matrix with the same dimensions of the electronic interstate coupling matrix t. Similarly, $\bar{\omega}$ in the denominator of equation 5.34 stands for $\omega \cdot I$, where the identity matrix I has the same dimensions as the matrix Ω.

Step 3: update Green's functions and self energies

The so far obtained Green's functions $G(E)$ and $D(\omega)$ are used in equations 5.23 and 5.29 to calculate the self energies $\Sigma(E)$ and $\Pi(\omega)$. The self energies due to interactions other than electron-phonon interaction are unchanged. These new self energies are used in equations 5.14, 5.15, 5.16 and 5.17 to update the Green's functions. These replace the old values for $G(E)$ and $D(\omega)$.

Step 4: iteration

The updating of the Green's functions and self energies, as described in step 3, is repeated until the self energies Σ^{ph} and Π^{el} have converged. Convergence of a matrix $M(E)$ is achieved if equation 5.35 holds for a certain predefined tolerance δ.

$$\left| \frac{M_{ij}^{(n)}(E) - M_{ij}^{(n-1)}(E)}{M_{ij}^{(n-1)}(E)} \right| < \delta \quad (\forall\ i, j, E) \tag{5.35}$$

Here is $M^{(n)}$ the matrix M after n iteration steps. For this work, δ is set to 10^{-4} for both electron and phonon self energies.

Step 5: one-particle characteristics

After convergence is achieved, several characteristics of the system can be calculated. The total current through the junction is given by equation 5.36.

$$I_L = -I_R = \frac{2e}{\hbar} \int \frac{dE}{2\pi} \mathrm{Tr}\left[\Sigma_L^{<}(E) G^{>}(E) - \Sigma_L^{>} G^{<}(E)\right] \tag{5.36}$$

Other characteristics that can be calculated are the dissipated power in the system and the density of electronic states on the bridge, which is given by equation 5.37 [12].

$$\rho_j = -\mathrm{Im}\left[\int \frac{dE}{\pi} G_{jj}^{r}(E)\right] \tag{5.37}$$

The Green's functions and self energies are calculated for all values for the applied bias V within a certain range, and from these the current is calculated as a function of V. The IETS spectrum is the second derivative of the current I to the applied bias V.

5.5 Technical details

The above described simulation has been implemented in Matlab. The program code can be found in appendix B. Several technical details are described in this section.

Voltage division factor

In this simulation the applied bias voltage does not influence the positions of the electronic levels in the bridge. The chemical potentials are changed according to equation 5.38.

$$\begin{aligned} \mu_L &= E_F + \eta |e| V \\ \mu_R &= E_F - (1-\eta)|e| V \end{aligned} \tag{5.38}$$

Here e is the electron charge and E_F is the unbiased Fermi energy. In all the calculations in this chapter $E_F = 0$ is taken. η is the *voltage division factor*, which is chosen as $\eta = \frac{\Gamma_R}{\Gamma_L + \Gamma_R}$. This reflects the influence of the coupling to the shifting of the electronic levels. In a typical STM geometry, coupling of the adsorbate to the substrate is larger than coupling of the adsorbate to the tip. This reflects in the choice for $\Gamma_L = 0.05$ and $\Gamma_R = 0.5$ in all calculations, where the left lead represents the tip and the right lead represents the substrate. For a better numerical stability, $\eta = 1$ is chosen in several calculations instead of $\eta = 0.91$. This might influence level positions, but if the changes are small, it has no influence on qualitative features.

Update factor

When after an iteration step the new Green's functions replace the old ones, this could lead to either a loop or an instability. To avoid this, the new Green's functions do not simply replace the old ones, but update them according to equation 5.39.

$$\begin{aligned} G^{(n)} &= \alpha G_c^{(n)} + (1-\alpha) G^{(n-1)} \\ D^{(n)} &= \alpha D_c^{(n)} + (1-\alpha) D^{(n-1)} \end{aligned} \tag{5.39}$$

Here $G_c^{(n)}$ and D_c^n are the electron and phonon Green's functions calculated at the n^{th} iteration step, and $G^{(n)}$ and $D^{(n)}$ are the Green's functions after n steps. α is the *update factor*, which is a value between 0 and 1. A lower value for α leads to better stability of the calculations, but to longer calculation times.

Expanding range

In the code, a certain energy grid is chosen which contains the most interesting features of the Green's functions and self energies. Outside this energy range, the Green's functions and self energies are not defined. Still, equations 5.23 and 5.29 require knowledge of the electron Green's functions outside this energy range. For simplicity, it is assumed that $G(E) = G(E_{min})$ for all $E < E_{min}$ and $G(E) = G(E_{max})$ for all $E > E_{max}$. Since the energy grid is chosen large enough to contain all features, this should not influence the calculation too much.

Zero momentum phonons

The Bose-Einstein distribution for phonons lead to a singularity in the occupation $N(\omega)$ for $\omega = 0$, and thus for the function F in equation 5.26. The only place F enters the calculation however is in the phonon self energy due to coupling to the thermal bath, equation 5.25. There it always comes as a multiplier of the thermal bath density of states, which is assumed to go to 0 as ω goes to 0 quicker than F goes to infinity. The point $\omega = 0$ can therefore be disregarded. To avoid singularities, a finite value for $N(\omega = 0)$ is chosen.

5.6 Raising the phonon occupation

As already mentioned in the introduction, IETS might be related to our sense of smell. To prove or disprove this statement, one possible experiment is to increase the phonon occupation in the energy range where the phonon density of states is the highest, i.e. around Ω. This leads to a different electron phonon interaction, which may result in a different current and a different inelastic tunneling spectrum. Since the width of the phonon density of states is small, the band width of the additional phonon occupation peak should also be small. This experiment might be conducted in the laboratory, where a laser emits light onto the substrate to excite vibrations in the adsorbates. The influence of a higher occupation of phonons near a specific band is theoretically investigated with the above mentioned model.

To account for more phonons present in the bridge molecule, a narrow peak around a specific value for ω is superposed on the Bose-Einstein distribution, resulting in a new $N(\omega)$. The quantification of the additional phonons is made with the integral: $N_{add} = \int d\omega \; N_{add}(\omega)$.

In order to know if this is a fair amount of extra phonons, one has to compare to experimentally plausible values. A typical infrared source emits 10^{17} photons per second over an area of 1 mm^2. A typical monolayer of adsorbates exists of 10^{15} molecules per cm^2. A linewidth of the density of phonon states of 5 meV leads with Heisenberg's uncertainty principle to a phonon lifetime of 0.4 ps. The photon-phonon coupling is assumed high enough that every photon induces one phonon. This leads to $N_{add} = 4 \cdot 10^{-9}$. This is much lower than the used N_{add} in the next section.

The validity of this model under these conditions is disputable. Although the important energy parameters M, ΔE and Γ, mentioned in section 5.3, are unchanged, the influence of electron-phonon coupling will be increased. An increase of $N(\omega)$ around $\omega = \Omega$, leads to an increase of $F(\omega)$ around $\omega = \pm\Omega$ (equation 5.26), which in turn gives rise to an increase of $D_0^{<,>}(\omega)$ around $\omega = \pm\Omega$ (equation 5.34). Ultimately this will increase the electron self energy due to electron-phonon interaction through equation 5.23. More electron-phonon scattering will increase the tunneling traversal time. This model is only valid if the traversal time is shorter than the inversed electron-phonon coupling, as is shown in equation 5.30. How much this time is changed by increasing $N(\omega)$ is not known.

5.7 Numerical results

To reduce calculation times, the bridge is assumed to have only one electronic level at $E = t_{11} = t$ and only one primary phonon mode at $\omega = \Omega_{11} = \Omega$. For all calculations the next standard set of parameters is used: $t = 1$ eV, $\Omega = 0.13$ eV, $M = 0.3$ eV, $\gamma_{ph} = 10^{-3}$ eV, $E_F = 0$ eV, $\Gamma_L = 0.05$ eV, $\Gamma_R = 0.5$ eV, $\eta = 1$, $\alpha = 0.5$ and $T = 10$ K.

Figure 5.6 shows the inelastic tunneling spectrum $\frac{d^2I}{dV^2}$ plotted against the bias voltage V for the standard set of parameters. The calculation time for these parameters was 17 minutes. It shows that besides the first harmonic around Ω, also the second and third harmonic shows in the IETS spectrum. This is a result of the SCBA, in which an infinite number of first order diagrams is taken into account. Therefore it is possible to emit or absorb two or even three phonons, although the probability decreases rapidly. The same set of parameters is used by Galperin *et al* (figure 4 in reference [40]) to calculate this IETS spectrum. The general features are the same, although in this graph the second harmonic is a dip instead of a wiggle. Also the absolute values differ.

Figure 5.7 repeats the calculation of figure 5.6, but introduces the extra phonons as described in the previous section. The distribution for the additional phonons is shown in figure 5.7a. The amount of additional phonons is $\int d\omega N_{add}(\omega) = 1$. Figures 5.7b - 5.7d show the IETS spectra without any additional phonons, with 10% of the additional phonons shown in figure 5.7a and with 100% of the additional phonons respectively. The calculation time for figure 5.7b was 9 hours, where the calculation time for figure 5.7c was 11 hours. It took however 27 hours to calculate figure 5.7d.

The IETS spectrum does not change significantly when adding 0.1 phonons. When adding 1 phonon however, the spectrum looks significantly different. The four large wiggles are equidistantly distributed at the same spacing as Ω. The amplitude is decreasing with increasing voltage, although the opposite has also been observed with a coarser grid. These features are not understood. They might be a numerical instability of some sort. Features at Ω, 2Ω and 3Ω are still present, albeit much smaller than before. This means that inelastic features are suppressed when adding a suitable amount of phonons. A possible explanation for this is that the counteracting elastic component grows larger and cancels out most of the inelastic spectrum.

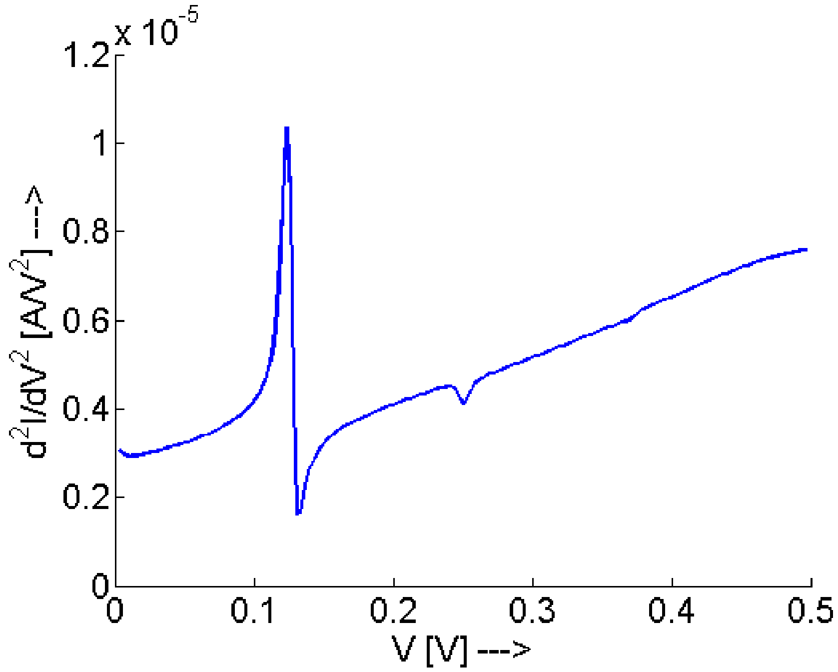

Figure 5.6: *The inelastic tunneling spectrum* d^2I/dV^2 *plotted against the bias voltage* V. *The standard set of parameters is used (see text). This calculation is done using a grid in electron energy of 3151 points spanning the range from* -1.0 eV *to* 2.75 eV *with step size* $2.5 \cdot 10^{-3}$ eV *and a grid in phonon energy of 401 points spanning the range from* -0.5 eV *to* 0.5 eV *with step size* $2.5 \cdot 10^{-3}$ eV. *The voltage grid contains 201 points spanning the range from* 0 V *to* 0.5 V *with step size* $2.5 \cdot 10^{-3}$ V.

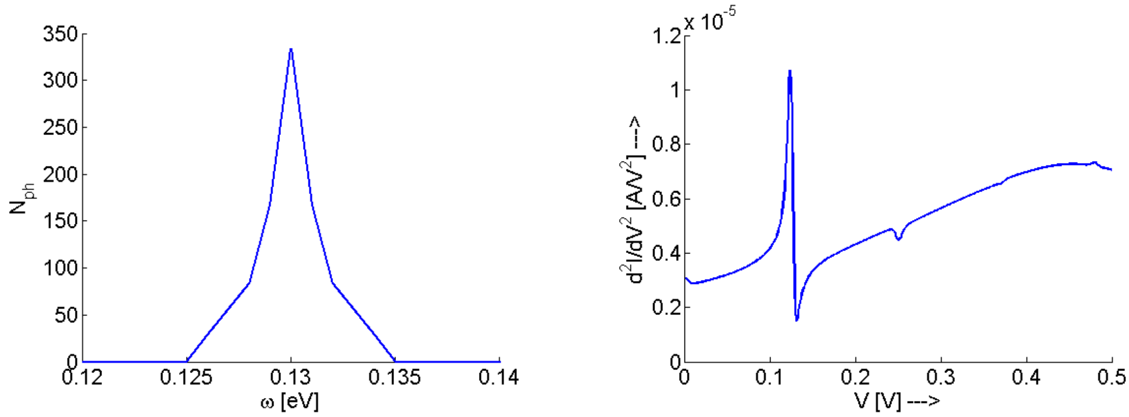

(a) Phonon distribution, used in d) **(b)** No additional phonons

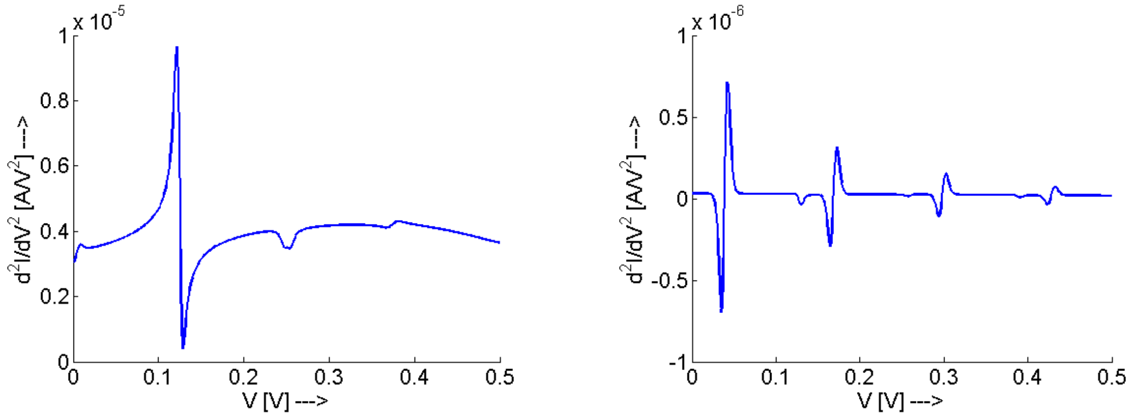

(c) 10% additional phonons **(d)** 100% additional phonons

Figure 5.7: *The inelastic tunneling spectra d^2I/dV^2 when phonons are added, plotted against the bias voltage V. The standard set of parameters is used (see text). These calculations are done using a grid in electron energy of 3751 points spanning the range from -1.0 eV to 2.75 eV with step size $1 \cdot 10^{-3}$ eV and a grid in phonon energy of 1001 points spanning the range from -0.5 eV to 0.5 eV with step size $1 \cdot 10^{-3}$ eV. The voltage grid contains 501 points spanning the range from 0 V to 0.5 V with step size $1 \cdot 10^{-3}$ V.*

Chapter 6

Simulations - Resonant case

The previous chapter explained a method to theoretically predict IETS spectra in the case of non resonant tunneling, based on perturbation theory where the electron-phonon coupling M is the small perturbation parameter. As already mentioned in section 2.4, resonant tunneling is characterized by longer electron life time in the bridge and hence stronger effective electron-phonon coupling. In this case, perturbation theory can no longer be used. However, a transformation of the Hamiltonian leads to a Hamiltonian in which direct electron-phonon coupling is absent.

This chapter will describe a model in which this transformation has been made. The same physical model, described in section 5.1, is valid for this model. The transformation is shown in section 6.1, after which sections 6.2 and 6.3 give the rest of the model and the calculation scheme used to calculate the IETS spectra. The Lehmann representation is used to calculate the step function on a periodic time grid. This will be explained in section 6.46. Section 6.5 gives the technical details of this simulation. The results turn out to be dependent on the size of the energy grid used. This is shown in section 6.3.

This chapter closely follows the work of [44], including the slightly different notation compared to the previous chapter.

6.1 Lang-Firsov transformation

The physical model used in this chapter is the same as described in section 5.1. To simplify the model, only one electronic level on the bridge is considered, with energy ϵ_0 and creation (annihilation) operator $\hat{c}^\dagger$ $(\hat{c})$ and only one primary phonon mode with energy ω_0 and creation (annihilation) operator $\hat{a}^\dagger$ $(\hat{a})$ is considered. The electron-phonon coupling is called M_a. The creation (annihilation) operators for the electronic states in the contacts are $\hat{c}_k^\dagger$ $(\hat{c}_k)$ with $k \in L, R$, the creation (annihilation) operators for the secondary phonons, labeled with β, are $\hat{b}_\beta^\dagger$ $(\hat{b}_\beta)$. The energy parameters V_k and U_β correspond to the electronic and the vibrational coupling, respectively. This leads to a zero-order Hamiltonian as in equation 6.2 and an interaction Hamiltonian as in equation 6.3.

$$\hat{H} = \hat{H}_0 + \hat{H}_1 \tag{6.1}$$

$$\hat{H}_0 = \epsilon_0 \hat{c}^\dagger \hat{c} + \sum_{k \in L,R} \epsilon_k \hat{c}_k^\dagger \hat{c}_k + \omega_0 \hat{a}^\dagger \hat{a} + \sum_\beta \omega_\beta \hat{b}_\beta^\dagger \hat{b}_\beta \tag{6.2}$$

$$\hat{H}_1 = \sum_{k \in L,R} (V_k \hat{c}_k^\dagger \hat{c} + V_k \hat{c}^\dagger \hat{c}_k) + M_a \hat{Q}_a \hat{c}^\dagger \hat{c} + \sum_\beta U_\beta \hat{Q}_a \hat{Q}_\beta \tag{6.3}$$

Here $\hat{Q}_a = (\hat{a}^\dagger + \hat{a})$ and $\hat{Q}_\beta = (\hat{b}_\beta^\dagger + \hat{b}_\beta)$ are phonon displacement operators. As done in previous works on strong electron-phonon interaction (see e.g. [45, 46]), a small polaron transformation is applied to the Hamiltonian 6.1, which is called the Lang-Firsov transformation [47].

$$\hat{\bar{H}} = e^{\hat{S}_a} \hat{H} e^{-\hat{S}_a} \tag{6.4}$$

with

$$\hat{S}_a = \frac{M_a}{\omega_0} (\hat{a}^\dagger - \hat{a}) \hat{c}^\dagger \hat{c} \tag{6.5}$$

The effect of this transformation on the vibrational coupling is neglected. This leads to the Hamiltonian 6.6.

$$\hat{\bar{H}} = \bar{\epsilon}_0 \hat{c}^\dagger \hat{c} + \sum_{k \in L,R} (V_k \hat{c}_k^\dagger \hat{c} \hat{X}_a + V_k \hat{c}^\dagger \hat{X}_a^\dagger \hat{c}_k) + \omega_0 \hat{a}^\dagger \hat{a} + \sum_\beta \omega_\beta \hat{b}_\beta^\dagger \hat{b}_\beta + \sum_\beta U_\beta \hat{Q}_a \hat{Q}_\beta \tag{6.6}$$

where

$$\bar{\epsilon}_0 = \epsilon_0 - \Delta, \quad \Delta \approx \frac{M_a^2}{\omega_0} \tag{6.7}$$

and

$$\hat{X}_a = \exp(i \lambda_a \hat{P}_a), \quad \lambda_a = \frac{M_a}{\omega_0}, \quad \hat{P}_a = -i(\hat{a} - \hat{a}^\dagger) \tag{6.8}$$

Δ is the electronic level shift due to coupling to the primary phonon mode, $\hat{X}_a$ is called the primary phonon shift generator and $\hat{P}_a$ is called the phonon momentum operator. The advantage of this transformation is that direct electron-phonon coupling is absent in Hamiltonian 6.6. The disadvantage is that extra operators are attached to the tunneling term in the Hamiltonian. These operators can be absorbed into a renormalized creation (annihilation) operator for the electrons on the bridge. This leads to an additional complication for the electron Green's function, which will be addressed in the next section.

6.2 Mathematical model

As in chapter 5, the NEGF approach is used to calculate properties of the system, described by Hamiltonian 6.6. The definitions for the Green's functions are the same as in equations 5.4 and 5.5, but the use of Hamiltonian 6.6 instead of Hamiltonian 6.1 leads to the use of the renormalized creation (annihilation) operators for the electrons on the bridge.

$$\begin{align} G(\tau_1, \tau_2) &= -i\langle \hat{T}_c \hat{c}(\tau_1) \hat{c}^\dagger(\tau_2)\rangle_H \tag{6.9} \\ &= -i\langle \hat{T}_c \hat{c}(\tau_1) \hat{X}_a(\tau_1) \hat{c}^\dagger(\tau_2) \hat{X}_a^\dagger(\tau_2)\rangle_{\bar{H}} \notag \\ D(\tau_1, \tau_2) &= -i\langle \hat{T}_c \hat{Q}_a(\tau_1) \hat{Q}_a(\tau_2)\rangle_H \tag{6.10} \\ &= -i\langle \hat{T}_c \hat{Q}_a(\tau_1) \hat{Q}_a(\tau_2)\rangle_{\bar{H}} \notag \end{align}$$

The subscripts H and $\bar{H}$ indicate which Hamiltonian determines the system evolution. τ_1 and τ_2 are time variables on the Keldysh contour, $\hat{T}_c$ is the contour time ordering operator. In the remainder of this chapter, the second form is used and the subscript $\bar{H}$ is omitted. As the next step, the Born-Oppenheimer approximation of decoupling electron and phonon dynamics is made.

$$G(\tau_1, \tau_2) \approx G_c(\tau_1, \tau_2) K(\tau_1, \tau_2) \tag{6.11}$$

where

$$\begin{align} G_c(\tau_1, \tau_2 &= -i\langle \hat{T}_c \hat{c}(\tau_1) \hat{c}^\dagger(\tau_2)\rangle \tag{6.12} \\ K(\tau_1, \tau_2 &= \langle \hat{T}_c \hat{X}_a(\tau_1) \hat{X}_a^\dagger(\tau_2)\rangle \tag{6.13} \end{align}$$

The functions G_c and K will be determined in a similar manner as in chapter 5. The function K will be written in terms of the phonon Green's function D, after which Dyson-like equations will be derived for the Green's functions G_c and D using Feynman diagrams. These will contain self energies for electrons and for phonons, which are called Σ and Π, respectively. By iterating this process, this model yields a self-consistent approach for the intermediate to strong electron-phonon coupling, analogue to the self-consistent Born approximation used in the weak coupling limit in chapter 5.

First, the shift generator correlation function K is expressed in terms of the phonon Green's function. This Green's function is defined as

$$D_{P_a P_a}(\tau_1, \tau_2) = -i\langle \hat{T}_c \hat{P}_a(\tau_1) \hat{P}_a \tau_2\rangle \tag{6.14}$$

In [44], a derivation is presented for an expression for K in terms of D_{P_a, P_a}; the result is presented in equation 6.15.

$$K(\tau_1, \tau_2) = \exp\left\{\lambda_a^2 \left[iD_{P_a P_a}(\tau_1, \tau_2) - \langle \hat{P}_a^2\rangle\right]\right\} \tag{6.15}$$

Here, $\langle \hat{P}_a^2\rangle = iD^{<,>}_{P_a P_a}(t, t)$, depending on which projection of $K(\tau_1, \tau_2)$ is considered. In steady state, $\langle \hat{P}_a^2\rangle$ is time independent.

Next, the electron Green's function $G_c(\tau_1, \tau_2)$, equation 6.12, and the phonon Green's function $D_{P_a,P_a}(\tau_1, \tau_2)$, equation 6.14, are expressed in terms of the corresponding self energies in Dyson-like equations. They are not real Dyson equations, because Wick's theorem is not valid due to the exponential operator $\hat{X}$. Reference [44] gives a derivation for these Dyson-like equations; the results are presented in equations 6.16 and 6.17.

$$D_{P_aP_a}(\tau, \tau') = D^{(0)}_{P_aP_a}(\tau, \tau') + \int_c d\tau_1 \int_c d\tau_2 D^{(0)}_{P_aP_a}(\tau, \tau_1)\Pi_{P_a,P_a}(\tau_1, \tau_2)D^{(0)}_{P_aP_a}(\tau_2, \tau') \tag{6.16}$$

$$G_c(\tau, \tau') = G^{(0)}_c(\tau, \tau') + \sum_{k\in L,R} \int_c d\tau_1 \int_c d\tau_2 G^{(0)}_c(\tau, \tau_1)\Sigma_{c,K}(\tau_1, \tau_2)G^{(0)}_c(\tau_2, \tau') \tag{6.17}$$

where the self energies Π_{P_a,P_a} and $\Sigma_{c,K}$ are given by the following equations.

$$\begin{aligned}
\Pi_{P_a,P_a}(\tau_1, \tau_2) &= \sum_{\beta} |U_\beta|^2 D_{P_\beta P_\beta}(\tau_1, \tau_2) - i\lambda_a^2 \sum_{k\in L,R} |V_k|^2 \times & (6.18)\\
&\quad \Big[g_k(\tau_2, \tau_1)G_c(\tau_1, \tau_2)\langle \hat{T}_c \hat{X}_a(\tau_1)\hat{X}^\dagger_a(\tau_2)\rangle + (\tau_1 \leftrightarrow \tau_2)\Big] & \\
\Sigma_{c,K}(\tau_1, \tau_2) &= \sum_{k\in K} |V_k|^2 g_k(\tau_1, \tau_2)\langle \hat{T}_c \hat{X}_a(\tau_2)\hat{X}^\dagger_a(\tau_1)\rangle & (6.19)
\end{aligned}$$

Here, $K = L, R$ are the two contacts and g_k is the free (unperturbed) electron Green's functions for state k in the contacts. Equations 6.15, 6.16 and 6.17 are solved self-consistently in the next section. Therefore the last $D^{(0)}_{P_aP_a}$ and $G^{(0)}_c$ are replaced by $D_{P_aP_a}$ and G_c, respectively.

6.3 Calculation scheme

The procedure used here is similar as in chapter 5. Zero order Green's functions are introduced to be able to calculate the self energies using equations 6.18 and 6.19, which in turn are used to calculate the Green's functions and the shift generator correlation function using equations 6.15, 6.16 and 6.17. This step is repeated until the self energies are converged. With the thus obtained self energies and Green's functions, one particle properties of the system are evaluated.

Since the dependence of K on $D_{P_aP_a}$ is exponential, projections of K are easier to express in terms of $D_{P_aP_a}$ in the time domain. However, lesser and greater projections of $D^{(0)}_{P_aP_a}$ and $G^{(0)}_c$ are easier to write down in the energy domain. Therefore, both domains are used and fast Fourier Transform is used to transform the functions between them. The projections of functions from the Keldysh time contour to the real time axis are the same as in section 5.2, where the superscripts $<$, $>$ and r stand for the lesser, greater and retarded projections, respectively. The calculation consists of the following steps.

Step 1: grids

The grids necessary are a time grid and an energy grid. The energy grid is chosen symmetric around $E = 0$. It should be chosen large enough to contain all interesting features. Grid step size should be chosen smaller than the spectral widths of the functions, but large enough to keep calculation time and data storage under control. Details on the choices made are provided in section 6.6. The time grid runs from 0 to a value T_{max}. The value of this maximum is not important, because the absolute value of time is never used. Therefore, time can be scaled at will.

Step 2: initial values

As in chapter 5, the initial values for the Green's functions are the zero-order Green's functions in electron-phonon interaction. The retarded zero-order Green's functions are given by the following two equations.

$$D^{(0),r}_{P_aP_A}(E) = \left[E - \omega_0 + \frac{i}{2}\gamma_{ph}\right]^{-1} - \left[E + \omega_0 + \frac{i}{2}\gamma_{ph}\right]^{-1} \tag{6.20}$$

$$G^{(0),r}_c(E) = \left[E - \bar{\epsilon}_0 - \Sigma^{(0),r}_c(E)\right]^{-1} \tag{6.21}$$

For the retarded phonon self energy due to coupling to the thermal bath, the wideband limit is used for the secondary phonons, resulting in an energy independent level-width γ_{ph}, analogue to equation 5.27.

$$\gamma_{ph} = 2\pi \sum_{\beta} |U_\beta|^2 \delta(E - \omega_\beta) \tag{6.22}$$

The retarded electron self energy due to coupling to the contacts is taken in the following form,

$$\Sigma^{(0),r}_c(E) = \Sigma^{(0),r}_{c,L}(E) + \Sigma^{(0),r}_{c,R}(E) \tag{6.23}$$

$$\Sigma^{(0),r}_{c,K}(E) = \frac{1}{2}\frac{\Gamma^{(0)}_K W^{(0)}_K}{E - E^{(0)}_K + iW^{(0)}_K} \tag{6.24}$$

where $K = L, R$, $E^{(0)}_K$ is the center of the band in the contacts, $W^{(0)}_K$ the half width of the band and $\Gamma^{(0)}_K$ is the escape rate to contact K in the electron wideband limit.

The lesser and greater zero-order phonon Green's functions are given by the following expression,

$$D^{<,>}_{P_aP_a}(E) = -iN(E)\frac{\gamma_{ph}}{(E \mp \omega_0)^2 + (\frac{1}{2}\gamma_{ph})^2} - i(1 + N(E))\frac{\gamma_{ph}}{(E \pm \omega_0)^2 + (\frac{1}{2}\gamma_{ph})^2} \tag{6.25}$$

where $N(E)$ is the Bose distribution of the thermal phonon bath. In equation 6.25 the upper sign corresponds to the lesser projection, the lower sign corresponds to the greater projection.

The lesser and greater zero-order electron Green's functions are given by the following expression,

$$G_c^{(0),<,>}(E) = |G_c^{(0),r}(E)|^2 \Sigma_c^{(0),<,>}(E) \tag{6.26}$$

where $\Sigma_c^{(0),<,>}$ is the zero-order electron self energy due to coupling to the contacts, taken in the following form,

$$\begin{aligned}
\Sigma_c^{(0),<,>}(E) &= \Sigma_{c,L}^{(0),<,>}(E) + \Sigma_{c,R}^{(0),<,>}(E) && (6.27)\\
\Sigma_{c,K}^{(0),<} &= i f_K(E)\Gamma_K(E) && (6.28)\\
\Sigma_{c,K}^{(0),>} &= -i(1 - f_K(E))\Gamma_K(E) && (6.29)
\end{aligned}$$

where

$$\Gamma_K(E) = -2\mathrm{Im}\left(\Sigma_{c,K}^{(0),r}(E)\right) = \frac{\Gamma_K^{(0)}(W_K^{(0)})^2}{(E - E_K^{(0)})^2 + (W_K^{(0)})^2} \tag{6.30}$$

is the escape rate to contact K, which would be energy independent in the electron wide-band limit, but in general is not. $f_K(E)$ is the Fermi distribution in contact K. The lesser and greater projections of the self energies and Green's functions are then transformed to the time domain.

Step 3: calculate the correlation functions for the shift generator operators

With Langreth rules [48] and equation 6.15, one gets the following expressions for the lesser and greater correlation functions for the shift generator operators.

$$\begin{aligned}
\langle \hat{X}_a^\dagger(0)\hat{X}_a(t)\rangle &= \exp\left\{i\lambda_a^2\left[D_{P_aP_a}^<(t) - D_{P_aP_a}^<(t=0)\right]\right\} && (6.31)\\
\langle \hat{X}_a(t)\hat{X}_a^\dagger(0)\rangle &= \exp\left\{i\lambda_a^2\left[D_{P_aP_a}^>(t) - D_{P_aP_a}^>(t=0)\right]\right\} && (6.32)
\end{aligned}$$

Step 4: calculate the self energies

Projections of equation 6.18 are used to obtain the following expressions for the lesser and greater phonon self energies due to coupling to the electrons in the time domain.

$$\begin{aligned}
\Pi_{P_aP_a,el}^<(t) &= i\lambda_a^2\langle \hat{X}_a^\dagger(0)\hat{X}_a(t)\rangle\left\{\left[\Sigma_c^{(0),>}(t)\right]^* G_c^<(t) + \Sigma_c^{(0),<}(t)\left[G_c^>(t)\right]^*\right\} && (6.33)\\
\Pi_{P_aP_a,el}^<(t) &= i\lambda_a^2\langle \hat{X}_a(t)\hat{X}_a^\dagger(0)\rangle\left\{\Sigma_c^{(0),>}(t)\left[G_c^<(t)\right]^* + \left[\Sigma_c^{(0),<}(t)\right]^* G_c^>(t)\right\} && (6.34)
\end{aligned}$$

Similarly, projections of equation 6.19 are used to obtain the following expressions for the lesser and greater electron self energies due to coupling to the contacts and to the phonons in the time domain.

$$\Sigma_c^<(t) = \Sigma_c^{(0),<}(t)\langle \hat{X}_a^\dagger(0)\hat{X}_a(t)\rangle \tag{6.35}$$

$$\Sigma_c^>(t) = \Sigma_c^{(0),>}(t)\langle \hat{X}_a(t)\hat{X}_a^\dagger(0)\rangle \tag{6.36}$$

In theory, the retarded self energies in the time domain can be obtained from the lesser and greater counterparts

$$\Sigma_c^r(t) = \theta(t)\left(\Sigma_c^>(t) - \Sigma_c^<(t)\right) \tag{6.37}$$

similar to equation 5.12. Because of the finite grid, inherent to the use of FFT, the time domain analog of the Lehmann representation

$$\Sigma_c^r(t) = \exp\left[-\delta t\right]\left(\Sigma_c^>(t) - \Sigma_c^<(t)\right) \tag{6.38}$$

is used with $\delta \to 0$ to suppress negative time contributions. This is explained in more detail in section 6.4. The self energies are then transformed to the energy domain.

Step 5: update the Green's functions

The in step 4 obtained self energies are used to update the Green's functions in the energy domain. The retarded Green's functions are given by the following equations.

$$D^r_{P_aP_a}(E) = \left[\frac{1}{D^{(0),r}_{P_aP_a}(E)} - \Pi^r_{P_aP_a,el}(E)\right]^{-1} \tag{6.39}$$

$$G_c^r(E) = \left[E - \bar{\epsilon}_0 - \Sigma_c^r(E)\right]^{-1} \tag{6.40}$$

$$\tag{6.41}$$

The Keldysh equations [49] 6.42 and 6.43 are used to obtain the lesser and greater projections of the Green's functions from the retarded projections.

$$D^{<,>}_{P_aP_a}(E) = |D^r_{P_aP_a}(E)|^2\Pi^{<,>}_{P_aP_a}(E) \tag{6.42}$$

$$G_c^{<,>}(E) = |G_c^r(E)|^2\Sigma_c^{<,>}(E) \tag{6.43}$$

These Green's functions replace the old Green's functions. The Green's functions are then transformed to the time domain.

Step 6: iteration

The in step 5 obtained Green's functions are used again in step 3 and 4 to update the correlation functions for the shift generator operators and the self energies, which in turn are used to update the Green's functions in step 5. This process is repeated until both the self energies $\Pi^r_{P_aP_a,el}(E)$ and $\Sigma^r_c(E)$ and both the Green's functions $D^r_{P_aP_a}(E)$ and $G^r_c(E)$ have converged. The convergence criterium is the same as in chapter 5, defined by equation 5.35, except here $\delta = 10^{-6}$.

Step 7: one particle characteristics

After convergence is achieved, several characteristics of the system can be calculated. The current is calculated with equation 5.36, the non equilibrium electronic density of states is calculated according to

$$A(E) = i\left(G^>(E) - G^<(E)\right) \tag{6.44}$$

and the non equilibrium electronic distribution in the bridge is given by

$$f(E) = \frac{\mathrm{Im}\left[G^<(E)\right]}{A(E)} \tag{6.45}$$

6.4 Lehmann representation

Consider a function $F(E)$ defined on a finite energy grid, with inverse Fourier transform $f(t)$, calculated with FFT. When one uses FFT, one inevitably assumes periodicity of all the functions defined on the time grid. Since no functions explicitly depend on the time parameter t, the scaling of t is random, and so is the period T. Once a period T is chosen, all the time-dependent functions are assumed to be periodic with this period, so $f(t+T) = f(t), \forall t \in \mathbb{R}$. This means that if the actual time-dependent function $\bar{f}(t)$ looks like the one schematically drawn in figure 6.1a, in the simulation after an inverse discrete Fourier transform from $F(E)$, this function is approximated by $f(t)$, which looks like the one drawn in figure 6.1b.

The time grid is chosen from 0 to T, but could as well have been chosen e.g. from $-T$ to 0. This means that the functions $f(t)$ will have contributions from both $t < 0$ and $t > 0$. For the retarded Green's functions, only contributions from $t > 0$ should be considered. The Green's functions and self energies are assumed to go to 0 as t goes to ∞. This means that most of the contributions will be near 0. For $t > 0$, this is on the left side of the time grid if it runs from 0 to T, but because of the periodicity of the functions, this is also on the left side of the time grid if it runs from e.g. $-T$ to 0, which is visible around $t = -T$ in figure 6.1b. For $t < 0$, this is on the right side of the time grid if it runs from $-T$ to 0, but again due to periodicity also on the right side of the time grid if it runs from 0 to T, which is visible around $t = T$ in figure 6.1b. An exponential factor is added to cut this contribution on the right side of the time grid, which mainly comes from $t < 0$, while keeping the contributions on the left side of the time grid, which mainly comes from $t > 0$.

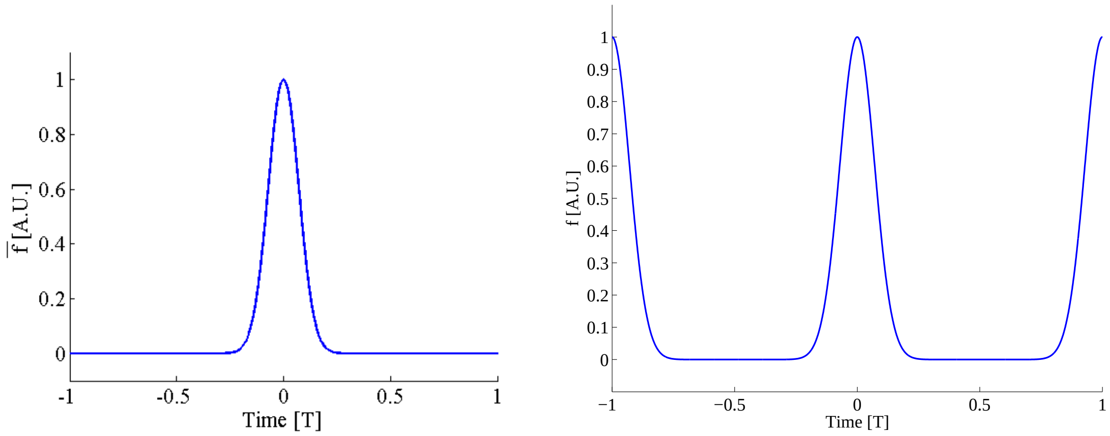

(a) **(b)**

Figure 6.1: *A random function $\bar{f}(t)$ as drawn in (a) looks like the function $f(t)$, drawn in (b), when it is calculated with an inverse Fourier transform, because periodicity is assumed when FFT is used.*

$$f^r(t) = \exp\left[-\delta t\right] f(t) \tag{6.46}$$

where $f(t)$ is the periodic function obtained from the inverse Fourier transform of $F(E)$ and $f^r(t)$ is an approximation of the non periodic function $\bar{f}(t)$ with only positive time contributions considered. δ is a small parameter, typical $\delta \sim \frac{4}{T}$. Figure 6.2 shows the result of this Lehmann representation. The green line is the original non periodical function $\bar{f}(t)$ for $t > 0$, the blue line is the function $f^r(t)$ obtained using the Lehmann representation with $\delta = \frac{4}{T}$. Obviously this is an approximation, but the Heaviside function in equation 6.37 cannot be implemented when a mixture of contributions is present on the same time grid.

6.5 Technical details

Voltage division factor

As in chapter 5, the applied bias voltage does not influence the positions of the electronic levels in the bridge, and the chemical potentials are changed according to equation 5.38. In the following calculations, $\eta = \frac{\Gamma_R}{\Gamma_L + \Gamma_R}$.

Update factor

As described in section 5.5, an update factor α is used to update the Green's functions with the newly calculated Green's functions. In the following calculations however, $\alpha = 1$,

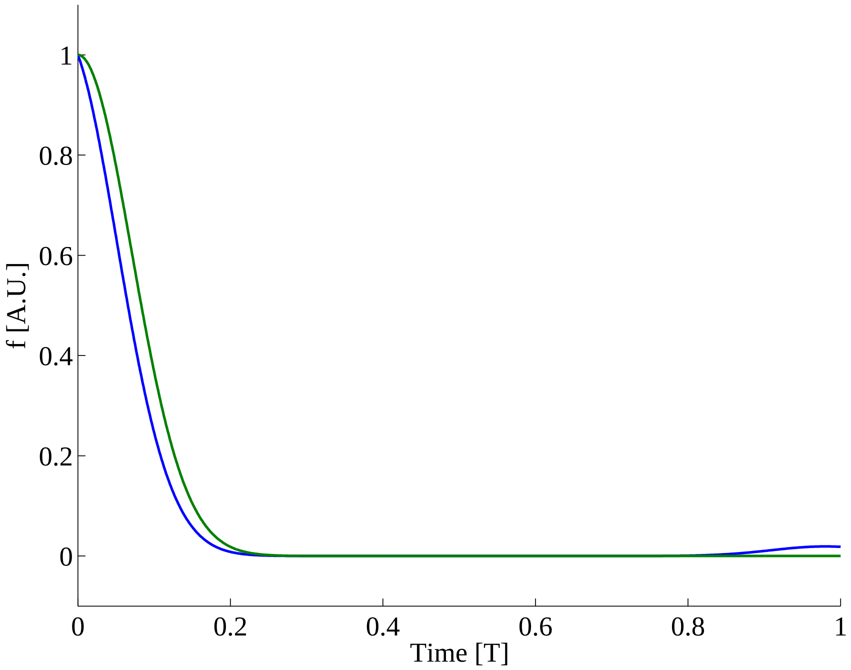

Figure 6.2: *The original non periodic function $\bar{f}(t)$ (green line) and the function $f^r(t)$, obtained with applying the Lehmann representation to the inverse Fourier transform of $F(E)$.*

which means that the newly calculated Green's functions simply replace the so far obtained ones.

6.6 Influence of energy range

The problem with the implementation of this model, shown in appendix C, is that the results depend on the range of the energy grid. An even bigger problem is that all features tend to disappear when a larger energy range is taken into account. Figure 6.3 shows the density of states as a function of energy. Phonon absorption and emission sidebands are seen at sufficient high temperature and weak coupling between bridge and leads, as long as the used energy range is small enough.

Figure 6.3 shows that the number of grid points is not important for the qualitative and quantitative features of the density of states. When a too small energy grid is chosen, neighboring features, which are nothing more than mirror images of the features that are taken into account due to inevitably assumed periodicity, might influence the calculations when Fourier transforms are used. One way to get around this problem is *zero padding*: adding zeros both left and right of the used functions, to move the mirror images far away from the grid of interest. Since the zero order Green's functions are nearly zero for large energies, this is equivalent to taking a larger energy grid into account.

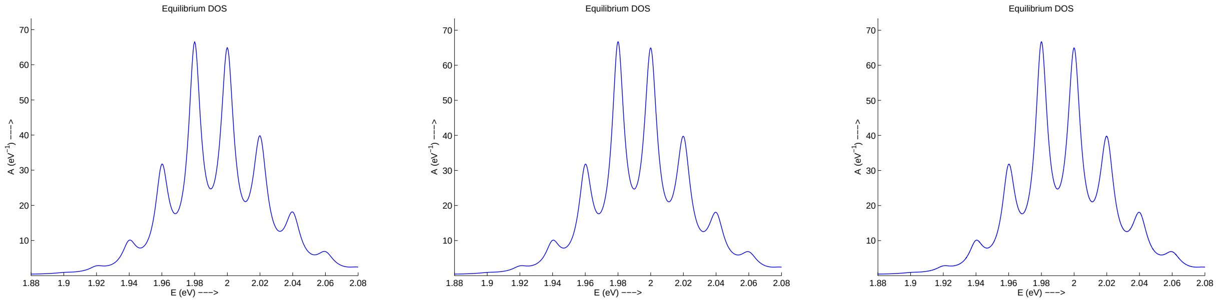

(a) $E = -4 : 5 \cdot 10^{-4} : 4$ **(b)** $E = -4 : 1 \cdot 10^{-4} : 4$ **(c)** $E = -4 : 2 \cdot 10^{-5} : 4$

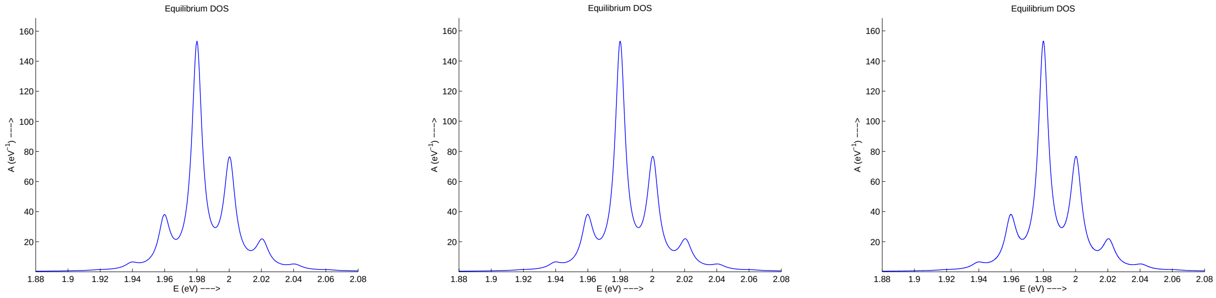

(d) $E = -10 : 5 \cdot 10^{-4} : 10$ **(e)** $E = -10 : 1 \cdot 10^{-4} : 10$ **(f)** $E = -10 : 2 \cdot 10^{-5} : 10$

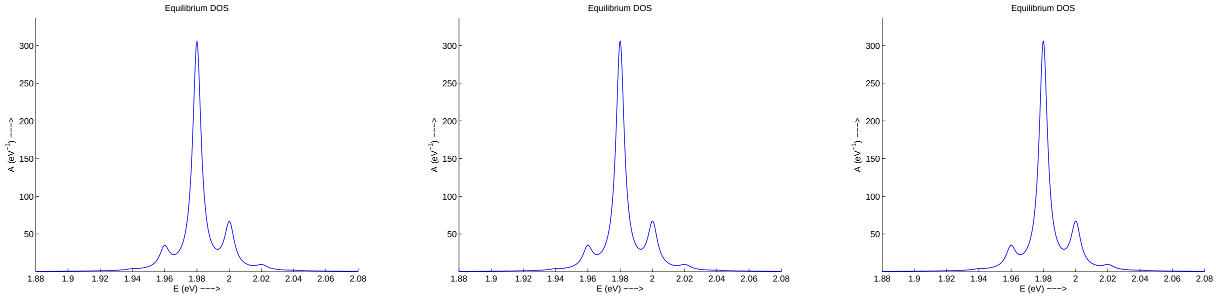

(g) $E = -25 : 5 \cdot 10^{-4} : 25$ **(h)** $E = -25 : 1 \cdot 10^{-4} : 25$ **(i)** $E = -25 : 5 \cdot 10^{-5} : 25$

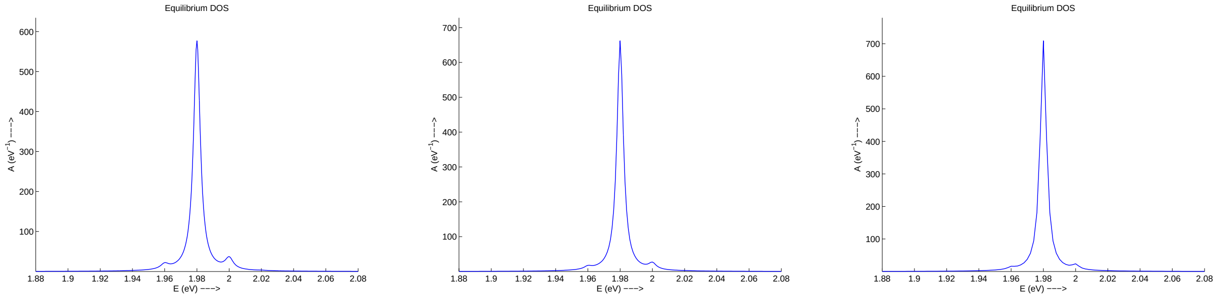

(j) $E = -100 : 5 \cdot 10^{-4} : 100$ **(k)** $E = -200 : 1 \cdot 10^{-3} : 200$ **(l)** $E = -400 : 2 \cdot 10^{-3} : 400$

Figure 6.3: *Equilibrium density of states for strong electron phonon coupling relative to the molecule-lead coupling. The parameters used in this calculation are* $T = 300\ K$, $\Gamma_L^{(0)} = \Gamma_R^{(0)} = 0.002\ eV$, $\epsilon_0 = 2\ eV$, $\omega_0 = 0.02\ eV$, $M_a = 0.02\ eV$, $\gamma_{ph} = 0.001\ eV$ *and* $E_F = 3.98\ eV$. *The different energy ranges are given in the corresponding captions, where* $-4 : 1 \cdot 10^{-4} : 4$ *is an energy grid from* -4 *to* $4\ eV$, *with grid spacing* $1 \cdot 10^{-4}\ eV$.

Chapter 7

Summary and outlook

7.1 IETS - The experiment

Although the mechanism of the nose is not understood, one idea is that it works as a vibrational spectroscope, similar to IETS. IETS is an experimental technique which is often used to study vibrations of adsorbates on a certain surface. With the use of an STM, IETS can be performed in single molecules.

The energy of vibrational modes of an adsorbed molecule is dependent on the substrate. The adsorbates studied in this work are NO molecules. The holes in the *d*-orbital of transition metals lead to a strong, coordinate bond between the N atom and the metal substrate, where the filled *d*-orbital of noble metals prevents this bond, resulting in a weaker bond. This influences the position of the vibrational modes in the IETS spectrum.

The noble metals used as substrates are Au(111), Ag(111), Au(100) and Ag(100). The first two substrates exhibit *sp*-surface states, resulting in features in the LDOS of the bare metal, clouding any vibrational features in the IETS spectrum. On Au(100), NO molecules are still mobile at $T = 4$ K. Adsorbate molecules have to be at a fixed position in order to perform many IETS measurements on them. Only on Ag(100), correct IETS measurements have been performed.

Not all vibrational modes can be observed with STM-IETS: some modes do not couple with the incident electrons. This coupling is dictated by selection rules, which are as yet unknown. For NO on Rh(111), the frustrated rotation mode had not been observed, although the Rh-NO stretch had been observed around 50 meV. For CO on Cu(100), comparable to NO on Ag(100), the frustrated rotation mode had been observed around 35 meV, but no Cu-CO stretch had been observed. For CO on Ag(110), a frustrated rotation mode had been observed around 21 meV. In this work, the IETS spectrum of NO on Ag(100) is presented. An antisymmetric peak around ±21 meV is ascribed to the frustrated rotation mode of NO; no other vibrational modes have been observed up to 150 meV.

An antisymmetric peak however, has also been observed on bare Ag(100). This suggests that an NO molecule is adsorbed on the tip. There are three characteristics to identify a molecule on the tip. First, atomic resolution is more easily achieved with an NO terminated tip, where it is not achieved at low setpoint current with a bare tip. Second, NO is imaged as a protrusion with an NO terminated tip, where it is imaged as a depression with a bare tip. Last, with an NO molecule on the tip, the IETS spectrum shows vibrational features even on a clean part of the substrate.

The fact that the observed peak over bare Ag is not shifted suggests that the W tip is Ag terminated due to the dipping procedure. The most likely position for NO on Ag is the upright position with the N atom bound to the Ag. When the tip is not dipped, the end atoms of the apex are tungsten atoms. When an NO molecule adsorbs to this W tip, the most likely position is the flat position, leading to observed peaks and dips in the IETS spectra around 56 meV and 101 meV. They had been calculated with DFT methods to be around 56 meV and 114 meV.

In the future, IETS spectra have to be taken with a bare tip. Deposition without the tip in the neighborhood is a requirement to do so. Dipping might be used to coat the tip with the same metal as the substrate is, but should be recorded carefully. Well controlled measurements will lead to reproducible spectra, which are required to construct selection rules for STM-IETS.

Another possible experiment for the future is taking IETS spectra while exciting the adsorbates. Laser light can be used to provide a narrow band energy source to excite certain vibrations of the adsorbates. A problem in practice is the extreme short lifetime of a molecular vibration (~ 1 ps).

7.2 IETS - The theory

The influence of certain parameters of the used system on the IETS spectrum can be predicted with a proper model for the STM tunnel junction. Many studies have been performed on this system, some of which are reviewed in this thesis.

The most general method is the NEGF, which uses non equilibrium Green's functions to calculate one particle characteristics like the tunneling current or the adsorbate density of states. Although the method is general, approximations have to be made to be able to calculate the Green's functions. In this thesis, the self consistent Born approximation is used for the case of non resonant tunneling, which neglects all interactions between electrons and phonons except for the Hartree and the Fock diagrams, which are second order in the small perturbation parameter M, which is a measure for the electron-phonon coupling. A simulation has been written to calculate the IETS spectrum of a typical STM tunnel junction. The effect of additional phonons due to excitations with phonons from a laser source, as would be the case in the experiment described above, shows not a lot of changes in the spectrum. For an extremely high number of additional phonons, the IETS features seem to decrease, although the calculations are possibly not stable.

In the resonant case, electron-phonon coupling is stronger, and coupling to the leads is smaller, requiring a different approach. A transformation of the Hamiltonian is used to renormalize the electron Green's functions in exchange for removal of direct electron-phonon coupling. The small perturbation parameter is V, the coupling of the electrons on the bridge molecule to the two contacts. A simulation has been written to calculate DOS and IETS spectra. Because some expressions are given in time domain, while others are given in energy domain, FFT is used to transform between them. Implementation of this has caused an error in the simulation, resulting in DOS which depend on the used energy range. Larger energy ranges lead to the disappearing of features in the DOS, which should not be the case.

The NEGF is a general model, which can also be used to calculate satellite peaks in the electronic resonance peak in the $\frac{dI}{dV}$-spectrum, or the heat generation in single molecule systems. Also large molecules with many electronic and vibrational levels can be modeled to fit IETS spectra. The above mentioned selection rules are a necessary input to these calculations.

Generalization of the used calculation schemes would involve using other terms in the Green's functions beside the Hartree and Fock terms, abandoning the non-crossing approximation, or going beyond second order in electron-phonon coupling in the non resonant case or in coupling to the contacts in the resonant case.

Appendix A

Clean Au and Ag substrates

A.1 Au(111)

The Au(111) samples used are evaporated gold on borosilicate glass samples from Arrandee. The thickness of the gold layer ≈ 250 nm. The surface has been made flat by either flame annealing, for which the procedure is described on Arrandee's website [50], or by annealing with the electron beam heater described in section 3.1 to 500°C for 30 minutes. The result of this is large grains of typically $500-1000$ nm size, separated by $10-30$ nm deep trenches. These grains either show as triangles with angles of 60 degrees or atomically flat terraces separated by step edges. The size of these triangles range from more than 100 nm to less than 10 nm and have a relative height of one *step height* compared to its neighbor. The size of these flat terraces depends on the quality of the annealing, but could range up to 200 nm and perhaps even more. They are separated by step edges with a height of one step height. The step height is material dependent. For Au(111) and Ag(111), the theoretical step height is $\frac{1}{3}\sqrt{3}a = 237$ pm, where $a = 410$ pm is the lattice constant of both Au and Ag in the fcc structure. Both structures can form on one surface, as is shown in figure A.1.

It is energetically unfavorable for Au atoms in a (111)-surface to stay in their original bulk positions. Rather, the surface is tend to be compressed, resulting in several orientations of the top surface to the layer beneath [51], collectively called the herringbone reconstruction. This is shown in figure A.2. It has been reported many times in literature, see e.g. [52, 53, 54, 55].

A line scan is taken at the line A in this image, which is shown in figure A.3. The typical height differences in figure A.2a is 40 pm. The higher lines in figure A.2a are called *tram rails*. The measured width of this tram rail, labeled with b in figure A.2a is 0.7 ± 0.2 nm. The small distance between them (labeled c) is measured to be 0.8 ± 0.2 nm, the large distance between them (labeled a) is measured to be 1.0 ± 0.2 nm.

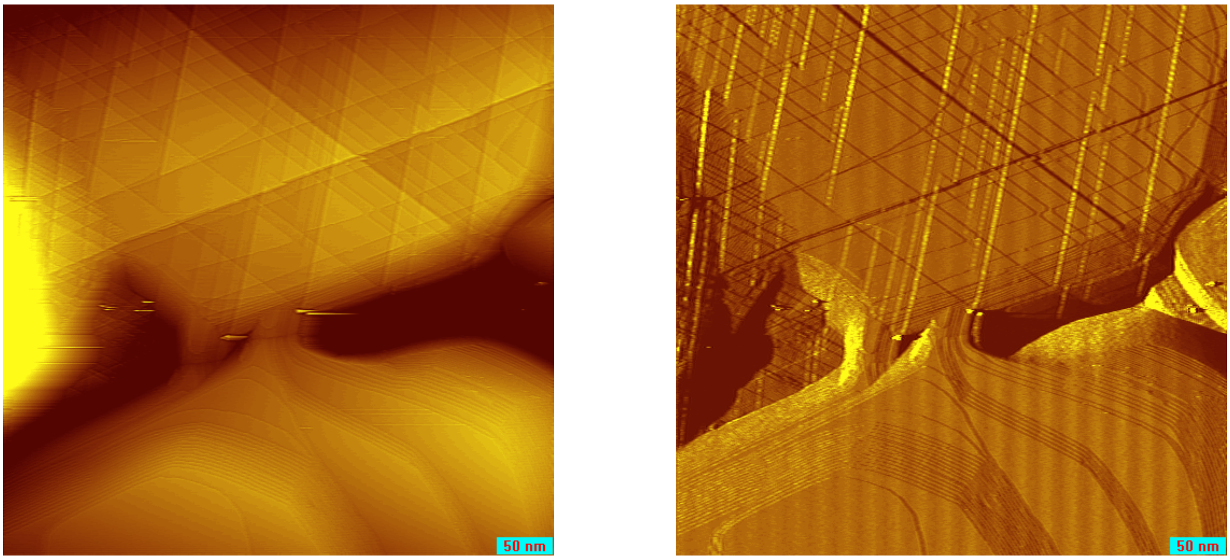

(a) Topography **(b)** Current

Figure A.1: *An STM image of e-beam annealed Au(111). The scan size is* 500×500 *nm,* $V_b = 150$ *mV,* $I_{sp} = 0.5$ *nA,* $T = 77$ *K. The upper part shows triangles, typical for annealed Au(111), the bottom part shows flat terraces, separated by step edges. These step edges tend to conglomerate.*

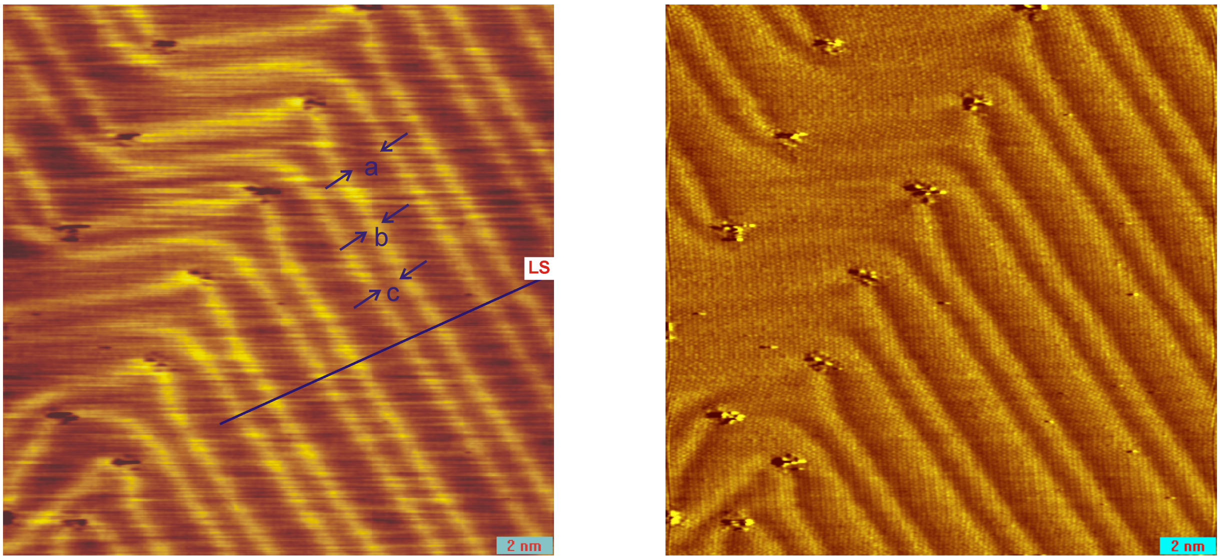

(a) Topography **(b)** Current

Figure A.2: *An STM image of e-beam annealed Au(111). The scan size is* 20×20 *nm,* $V_b = 150$ *mV,* $I_{sp} = 0.5$ *nA,* $T = 77$ *K. Clearly visible is the surface reconstruction, which is the herringbone reconstruction in the case of Au(111).*

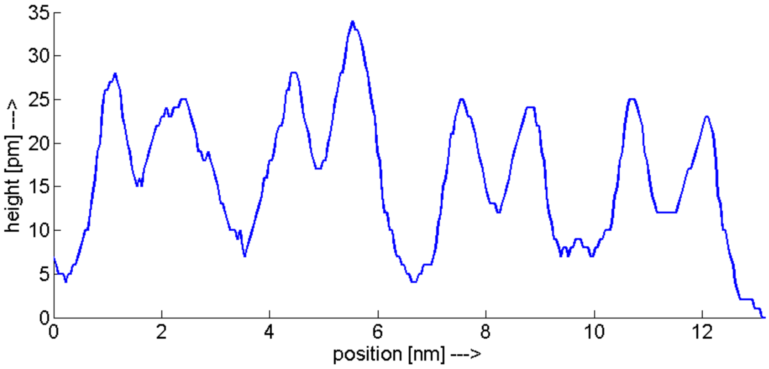

Figure A.3: *A line scan, taken at line LS in figure A.2a.*

A.2 Ag(111)

The used Ag(111) sample is a single crystal sample. It has been cleaned by sputtering, described in section 3.1 and annealed to 500°C for 30 minutes. Ag(111) does not exhibit surface reconstruction, although there are clearly visible surface states, which are shown in figure A.4. A zoom in of these states and a local density of states measurement is presented in section 4.2.

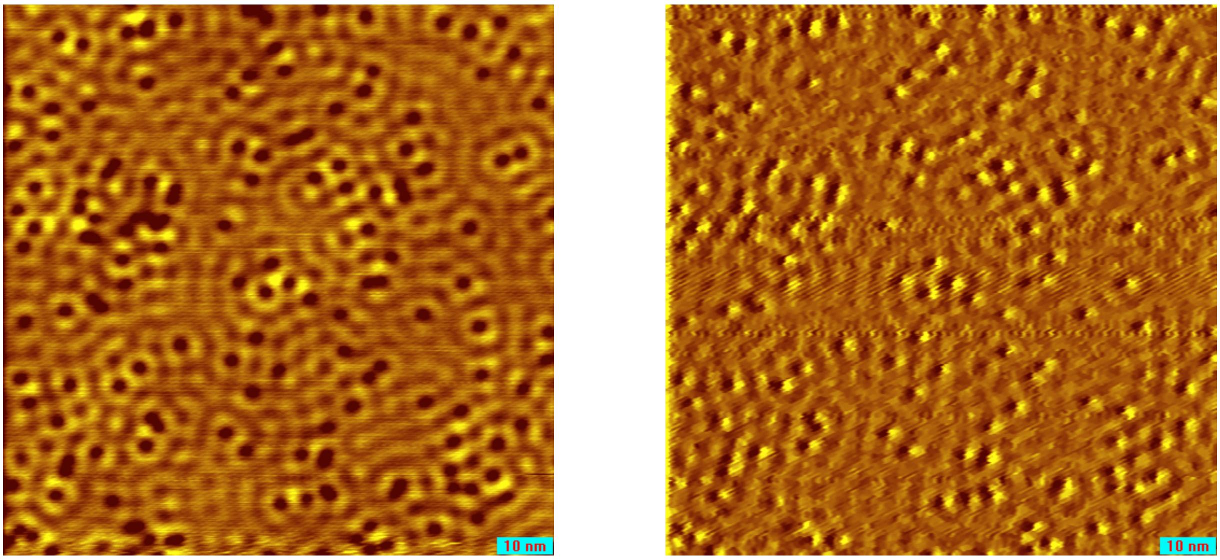

(a) Topography **(b)** Current

Figure A.4: *An STM image of e-beam annealed Ag(111). The scan size is* 100×100 *nm,* $V_b = 10$ *mV,* $I_{sp} = 0.4$ *nA,* $T = 4$ *K. Clearly visible are the sp−surface states.*

A.3 Au(100)

The Au(100) sample used is a single crystal sample. The surface has been cleaned by sputtering and made flat by annealing with the electron beam heater described in section 3.1 to 500°C for 30 minutes. As mentioned in section 4.3, the surface layer of Au(100) reconstructs. This reconstruction and buckling is schematically shown in figure A.5.

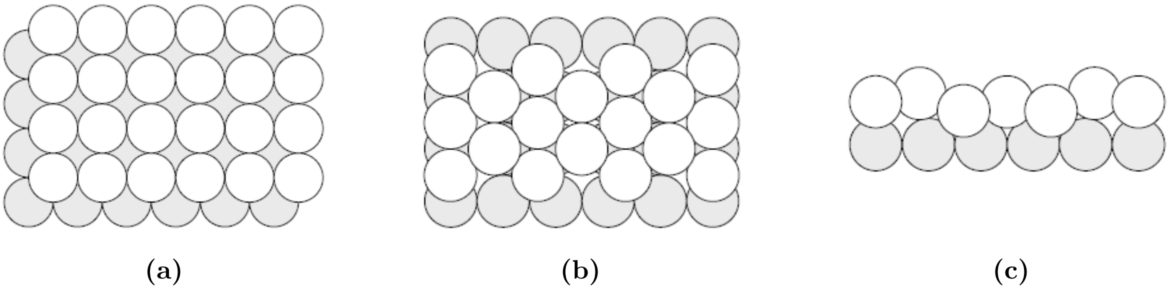

(a) **(b)** **(c)**

Figure A.5: *a) The unreconstructed Au(100) surface. b) The quasi-hexagonal reconstruction of the Au(100) surface. c) Side view of the reconstruction. The phenomenon that height differences occur, is called buckling.*

The reconstruction can be visualized by STM imaging. On a large scale, this leads to rows with a spacing of 1.5 ± 0.1 nm, as shown in figure A.6. On a small scale, this leads to the quasi-hexagonal structure as shown in figure A.7.

A.4 Ag(100)

The Ag(100) sample used is a single crystal sample. The sample was cleaned by sputtering, described in section 3.1 and annealed to 500°C for 30 minutes. There is no surface reconstruction, nor any surface states on clean Ag(100). Figure A.8 shows the clean Ag(100) surface.

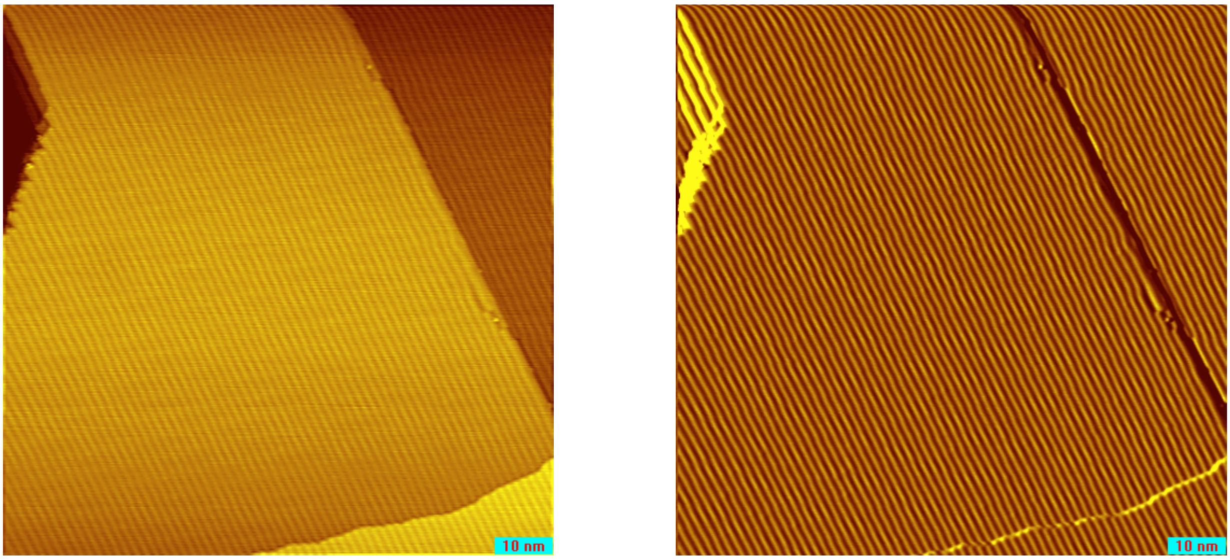

(a) Topography **(b)** Current

Figure A.6: *An STM image of e-beam annealed Au(100). The scan size is* 96×96 *nm,* $V_b = 100$ *mV,* $I_{sp} = 0.75$ *nA,* $T = 77$ *K. The surface reconstruction leads to atom rows parallel to the step edges.*

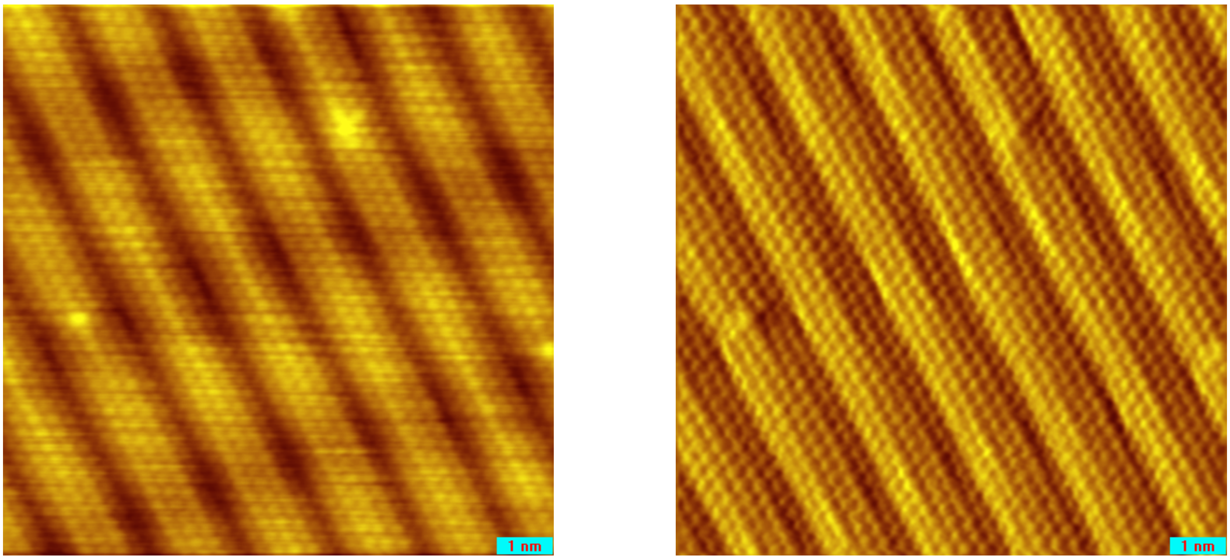

(a) Topography **(b)** Current

Figure A.7: *Another STM image of e-beam annealed Au(100). The scan size is* 10×10 *nm,* $V_b = 1$ *mV,* $I_{sp} = 6$ *nA,* $T = 77$ *K. The surface reconstruction leads to a quasi-hexagonal arrangement.*

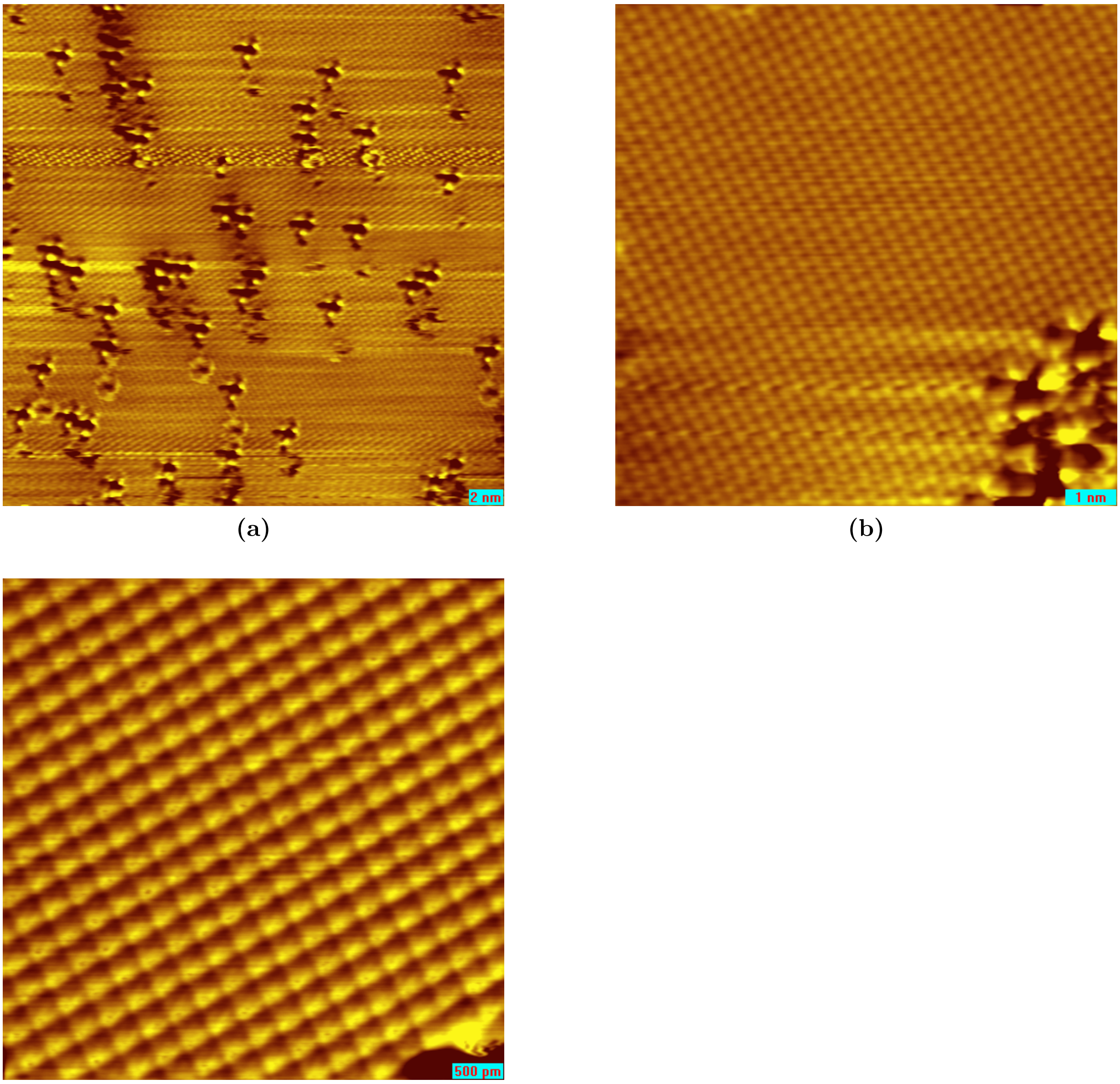

(a)

(b)

(c)

Figure A.8: *Three topographic images of a clean Ag(100) surface. The black dots in figure a and the features in the bottom right of figures b and c are vacancies. a) Scan size is* 30×30 *nm,* $V_b = 100$ *mV,* $I_{sp} = 0.1$ *nA,* $T = 4$ *K. b) Scan size is* 10×10 *nm,* $V_b = 15$ *mV,* $I_{sp} = 0.1$ *nA,* $T = 4$ *K. c) Scan size is* 5×5 *nm,* $V_b = 15$ *mV,* $I_{sp} = 0.1$ *nA,* $T = 4$ *K.*

Appendix B

Matlab files belonging to chapter 5

There are five m-files required to run this program. They should be in one directory, startiter.m is the m-file to run the simulation.

startiter.m

```
clear all

%*******************************************************************

%Physical constants

q = 1.60217646e-19; %Electron charge
hbar = 1.05457148e-34; %Planck's constant

%*******************************************************************

%System parameters

EF=0; %Fermi energy
kT = 10 * 8.617e-5; %Temperature

%Position of electronic bridge level
t = 1; %NB t = t(1,1) = E(1)

%Couplings between bridge electron states and lead electron states (all in
%eV)
DeltaL = 0.05; DeltaR = 0.5; Delta=DeltaL+DeltaR;

%Voltage division factor
```

```
%eta=trace(DeltaR)/trace(Delta);
eta=1; %Most of the times, eta=1 is chosen for better numerical stability

%Energy of primary phonon (in eV);
Omega = 0.13;

%Coupling between bridge electron state and primary phonon state (in
%eV)
M = 0.3;

%Coupling between primary phonon state and secondary phonon states (in eV)
zeta = 1e-3;

%**********************************************************************

%E-grid parameters (all in eV)
Emin = -1; Emax = 2.75; dE = 0.0025;

%omega-grid parameters (all in eV)
omegamin = -0.5; omegamax = 0.5; domega = dE;

%Make E-grid
E = (Emin:dE:Emax)'; NE = length(E); for dummyi=1:NE
    if abs(E(dummyi))<0.1*dE
        E(dummyi)=0;
    end
end
%Make omega-grid
omega = (omegamin:domega:omegamax)'; Nomega = length(omega); for
dummyi=1:Nomega
    if abs(omega(dummyi))<0.1*domega
        omega(dummyi)=0;
    end
end

%**********************************************************************

%Tolerance levels for self energies
Sigmachange = 1e-3; Pichange = 1e-3;

%Voltage sweep parameters
dV=dE; %Never make dV<dE, otherwise you get numerical instability
Vmin=0; Vmax=0.5; VV = (Vmin:dV:Vmax)'; NV = size(VV,1); II =
```

```
zeros(NV,1);

%Here starts the voltage sweep
tic for iV = 1:NV
    V = VV(iV);
    muL = EF+eta*V;
    muR = EF-(1-eta)*V;
    voltstep; %Start the iteration to determine the Green’s functions
    calccurrent; %Use the Green’s functions to determine the current.
    II(iV) = currentI;
    if iV == 1
        required_time = toc*NV %Show how long the calculation will take
    end
end %of the bias sweep loop

G1 = diff(II)./dV; VG=VV(2:NV)-0.5*dV*ones(NV-1,1); IETS =
diff(G1)./dV; VIETS=VV(2:(NV-1));

elapsed_time=toc
save data001
```

voltstep.m

```
%Equation numbers refer to Galperin’s paper "Inelastic electron tunneling
%spectroscopy in molecular junctions: Peaks and dips", Journal of Chemical
%Physics volume 121, number 23, pp 11965

%Step 1

GammaL = DeltaL * ones(NE,1); GammaR = DeltaR * ones(NE,1); Gamma =
GammaL + GammaR;

fL=1 ./ (1 + exp((E - muL) ./ kT)); %Fermi Dirac distribution
fR=1 ./ (1 + exp((E - muR) ./ kT));

gamma = zeta * ones(Nomega,1);

F = zeros(Nomega,1); for dummyomega = 1:Nomega
    F(dummyomega) = funcF(omega(dummyomega),kT);
end minF = zeros(Nomega,1); for dummyomega = 1:Nomega
    minF(dummyomega) = funcF( - omega(dummyomega),kT);
end
```

```
%*********************************************************************

%Step 2

%Equation 23a
G0r = 1 ./ (E - t + 1/2 * i * Gamma); G0a = conj(G0r);
%Equation 23b
G0l = (i * fL .* GammaL + i * fR .* GammaR) ./ ((E - t).^2 + (1/2 *
Gamma).^2);
%Equation 23c
G0g = ( - i * (1 - fL) .* GammaL - i * (1 - fR) .* GammaR) ./ ((E -
t).^2 + (1/2 * Gamma).^2);

%Equation 24a
D0r = 1 ./ (omega - Omega + (i/2) * gamma) - 1 ./ (omega + Omega +
(i/2) * gamma); D0a = conj(D0r);
%Equation 24b
D0l = F .* (D0r - D0a) .* sign(omega);
%Equation 24c
D0g = minF .* (D0r - D0a) .* sign(omega);

%Temporary Green's functions
Gr = G0r; Ga = G0a; Gl = G0l; Gg = G0g; Dr = D0r; Da = D0a; Dl =
D0l; Dg = D0g;


%*********************************************************************

%Step 3

%Equation 15a
SigmaLr =  - 1/2 * i * GammaL; SigmaLa = conj(SigmaLr);
%Equation 15b
SigmaLl = i * GammaL .* fL;
%Equation 15c
SigmaLg =  - i * GammaL .* (1 - fL);

%Equation 15a
SigmaRr =  - 1/2 * i * GammaR; SigmaRa = conj(SigmaRr);
%Equation 15b
SigmaRl = i * GammaR .* fR;
%Equation 15c
```

```
SigmaRg =  - i * GammaR .* (1 - fR);

%Zero order electron self energy due to interactions with phonons is zero
Sigmaphr = zeros(NE,1); Sigmapha = zeros(NE,1); Sigmaphl =
zeros(NE,1); Sigmaphg = zeros(NE,1);

%Equation 19a
Piphr =  - 1/2 * i * sign(omega) .* gamma; Pipha = conj(Piphr);
%Equation 19b
Piphl =  - i * gamma .* F;
%Equation 19c
Piphg =  - i * gamma .* minF;

%Zero order phonon self energy due to interactions with electrons is zero
Pielr = zeros(Nomega,1); Piela = zeros(Nomega,1); Piell =
zeros(Nomega,1); Pielg = zeros(Nomega,1);

%*******************************************************************

%Step 4

Sigmacheck = 0; Picheck = 0; itstep = 0; %itstep is the number of iteration steps
while ( min(Sigmacheck,Picheck) == 0 )

    itstep = itstep + 1;
    Sigmaphrold = Sigmaphr;
    Pielrold = Pielr;

    %Equation 17a
    Grexpanded = [Gr(1) * ones(Nomega,1);Gr;Gr(end) * ones(Nomega,1)];
    Glexpanded = [Gl(1) * ones(Nomega,1);Gl;Gl(end) * ones(Nomega,1)];
            %Equation 17 states Grij(E-omega), but in this calculation Grij is
            %only defined in the E-range from Emin to Emax. To take the values
            %of Grij for E<Emin and E>Emax, Grij is expanded with
            %Grij(E) = Grij(Emin) for E<Emin and Grij(E) = Grij(Emax) for E>Emax.
            %Something similar goes for Ggij and Glij
    integrand = zeros(NE,1);
    for dummyomega = 1:Nomega
        A1 = Dl(dummyomega) * Grexpanded(Nomega + 1 -
            round(omega(dummyomega)/domega):Nomega + NE -
            (omega(dummyomega)/domega));
        B1 = Dr(dummyomega) * Glexpanded(Nomega + 1 -
            round(omega(dummyomega)/domega):Nomega + NE -
```

```
        (omega(dummyomega)/domega));
    C1 = Dr(dummyomega) * Grexpanded(Nomega + 1 -
        round(omega(dummyomega)/domega):Nomega + NE -
        (omega(dummyomega)/domega));
    integrand = integrand + domega / (2 * pi) * (A1 + B1 + C1);
    clear A1 B1 C1
end
Sigmaphr = i * M^2 * integrand;
Sigmapha = conj(Sigmaphr);

%Equation 17b
Glexpanded = [Gl(1) * ones(Nomega,1);Gl;Gl(end) * ones(Nomega,1)];
integrand = zeros(NE,1);
for dummyomega = 1:Nomega
    A1 = Dl(dummyomega) * Glexpanded(Nomega + 1 -
        round(omega(dummyomega)/domega):Nomega + NE -
        (omega(dummyomega)/domega));
    integrand = integrand + domega / (2 * pi) * A1;
    clear A1
end
Sigmaphl = i * M^2 * integrand;

%Equation 17c
Ggexpanded = [Gg(1) * ones(Nomega,1);Gg;Gg(end) * ones(Nomega,1)];
integrand = zeros(NE,1);
for dummyomega = 1:Nomega
    A1 = Dg(dummyomega) * Ggexpanded(Nomega + 1 -
        round(omega(dummyomega)/domega):Nomega + NE -
        (omega(dummyomega)/domega));
    integrand = integrand + domega / (2 * pi) * A1;
    clear A1
end
Sigmaphg = i * M^2 * integrand;

%*************************************************************************

%Step 5

%Equation 22a
Pielr=zeros(Nomega,1);
for dummyomega = 1:Nomega
    Gaexpanded = [Ga(1) * ones(Nomega,1);Ga;Ga(end) * ones(Nomega,1)];
    Glexpanded = [Gl(1) * ones(Nomega,1);Gl;Gl(end) * ones(Nomega,1)];
```

```
    A1 = Gl .* Gaexpanded(Nomega + 1 -
        round(omega(dummyomega)/domega):Nomega + NE -
        (omega(dummyomega)/domega));
    B1 = Gr .* Glexpanded(Nomega + 1 -
        round(omega(dummyomega)/domega):Nomega + NE -
        (omega(dummyomega)/domega));
    Pielr(dummyomega) = - i * M^2 * dE / (2 * pi) * sum(A1 + B1);
end
Piela = conj(Pielr);
%Equation 22b
Piell=zeros(Nomega,1);
for dummyomega = 1:Nomega
    Ggexpanded = [Gg(1) * ones(Nomega,1);Gg;Gg(end) * ones(Nomega,1)];
    A1 = Gl .* Ggexpanded(Nomega + 1 -
        round(omega(dummyomega)/domega):Nomega + NE -
        (omega(dummyomega)/domega));
    Piell(dummyomega) = - i * M^2 * dE / (2*pi) * sum(A1);
end
%Equation 22c
Pielg=zeros(Nomega,1);
for dummyomega = 1:Nomega
    Glexpanded = [Gl(1) * ones(Nomega,1);Gl;Gl(end) * ones(Nomega,1)];
    A1 = Gg .* Glexpanded(Nomega + 1 -
        round(omega(dummyomega)/domega):Nomega + NE -
        (omega(dummyomega)/domega));
    Pielg(dummyomega) = - i * M^2 * dE / (2*pi) * sum(A1);
end

%*************************************************************************

%Step 6

%Equation 13
Sigmar = SigmaLr + SigmaRr + Sigmaphr;
Sigmaa = SigmaLa + SigmaRa + Sigmapha;
Sigmal = SigmaLl + SigmaRl + Sigmaphl;
Sigmag = SigmaLg + SigmaRg + Sigmaphg;

%Equation 14
Pir = Piphr + Pielr;
Pia = Pipha + Piela;
Pil = Piphl + Piell;
Pig = Piphg + Pielg;
```

```
%*************************************************************************

%Step 7

alpha = 0.5;
Grold = Gr; Gaold = Ga; Glold = Gl; Ggold = Gg;
Drold = Dr; Daold = Da; Dlold = Dl; Dgold = Dg;

%Equation 9
Gr = 1 ./ ((1 ./ G0r) - Sigmar);
Ga = conj(Gr);

%Equation 11
Gl = Gr .* Sigmal .* Ga;
Gg = Gr .* Sigmag .* Ga;

%Equation 10
Dr = 1 ./ ((1 ./ D0r) - Pir);
Da = conj(Dr);

%Equation 12
Dl = Dr .* Pil .* Da;
Dg = Dr .* Pig .* Da;

Gr = alpha * Gr + (1 - alpha) * Grold;
Ga = alpha * Ga + (1 - alpha) * Gaold;
Gl = alpha * Gl + (1 - alpha) * Glold;
Gg = alpha * Gg + (1 - alpha) * Ggold;

Dr = alpha * Dr + (1 - alpha) * Drold;
Da = alpha * Da + (1 - alpha) * Daold;
Dl = alpha * Dl + (1 - alpha) * Dlold;
Dg = alpha * Dg + (1 - alpha) * Dgold;

%*************************************************************************

%Step 8

max(abs(Sigmaphrold - Sigmaphr))
if max(abs(Sigmaphrold - Sigmaphr)) < Sigmachange
    Sigmacheck = 1;
end
```

```
    if max(abs(Pielrold - Pielr)) < Pichange
        Picheck = 1;
    end

end %of the while loop

%************************************************************************
```

funcF.m

```
function dummyF = funcF(omega,kT) if omega > 0
    dummyF = funcN(omega,kT);
end if omega < 0
    dummyF = 1 + funcN(-omega,kT);
end if omega == 0
    dummyF = funcN(1e-3,kT);
end
```

funcN.m

```
function dummyN = funcN(omega,kT) dummyN = 1/(exp(omega/kT)-1);

%The following lines are added when additional phonons are required. These
%numbers are used to produce figure 5.6d

%steps = 0.001;
%
%if (abs(omega-(0.13)) < 1e-7) || (abs(omega+(0.13)) < 1e-7)
%    dummyN=dummyN+1/3*1/steps;
%end
%if (abs(omega-(0.13-1*steps)) < 1e-7) || (abs(omega-(0.13+1*steps)) < 1e-7) ||
(abs(omega-(-0.13-1*steps)) < 1e-7) || (abs(omega-(-0.13+1*steps)) < 1e-7)
%    dummyN=dummyN+1/6*1/steps;
%end
%if (abs(omega-(0.13-2*steps)) < 1e-7) || (abs(omega-(0.13+2*steps)) < 1e-7) ||
(abs(omega-(-0.13-2*steps)) < 1e-7) || (abs(omega-(-0.13+2*steps)) < 1e-7)
%    dummyN=dummyN+1/12*1/steps;
%end
%if (abs(omega-(0.13-3*steps)) < 1e-7) || (abs(omega-(0.13+3*steps)) < 1e-7) ||
(abs(omega-(-0.13-3*steps)) < 1e-7) || (abs(omega-(-0.13+3*steps)) < 1e-7)
%    dummyN=dummyN+1/18*1/steps;
```

```
%end
%if (abs(omega-(0.13-4*steps)) < 1e-7) || (abs(omega-(0.13+4*steps)) < 1e-7) ||
(abs(omega-(-0.13-4*steps)) < 1e-7) || (abs(omega-(-0.13+4*steps)) < 1e-7)
%    dummyN=dummyN+1/36*1/steps;
%end
```

calccurrent.m

```
%Calculate the current

fL = 1./(1+exp((E-muL)./kT)); GammaL = DeltaL*ones(NE,1);

%Equation 15b
SigmaLl = i*GammaL.*fL;

%Equation 15c
SigmaLg = -i*GammaL.*(1-fL);

%Equation 27
summand = SigmaLl.*Gg - SigmaLg.*Gl; currentI =
real(2*q*q/hbar*dE/(2*pi)*sum(summand));
```

Appendix C

Matlab files belonging to chapter 6

There are three m-files required to run this program. They should be in one directory, startiter.m is the m-file to run the simulation.

startiter.m

```
clear all

tic

%*************************************************************************

pmset; %Load the set of parameters

%E-grid parameters (all in eV)
Emin = -4; Emax = 4; dE=5e-4;

%Make E-grid
E = (Emin:dE:Emax)'; NE = length(E); for dummyi=1:NE
    if abs(E(dummyi))<0.1*dE
        E(dummyi)=0;
    end
end

t = (0:(NE-1));

%*************************************************************************

%Bose distribution for the phonons
N = 1./(exp(abs(E)/kT)-0.999);
```

```
%There is no voltage sweep taken into this m-file, but this can easily be
%added.

muL = EF+eta*V; muR = EF-eta*V;

voltstep

GGl = fftshift(fft(tGl.*tXad0Xat)); GGg =
fftshift(fft(tGg.*tXatXad0));

AA = real(i*(GGg-GGl)); f = imag(GGl)./AA; II1 =
real(sum(SigmaL0l.*Gg-SigmaL0g.*Gl)/(2*pi)*(1.6e-19)^2/hbar*dE)

clear t* fL fR *g *l Sigma*0* G*0* D*0* GammaL GammaR Sigmarold
filename=['filename_here']; save(filename)
```

pmset.m

```
%Physical constants

q = 1.60217646e-19; %Electron chaerge
hbar = 1.05457148e-34; %Planck's constant

%*******************************************************************

%System parameters

kT = 10 * 8.617e-5;

%Unperturbed position of electronic bridge level
eps0 = 2;

%Contact energy parameters
%EK0 is the centre of the band of the contact
%WK0 is the half width of the band of the contact
%GammaK0 is the escape rate to contact K in the electron wideband limit
%(WK0->infinity relative to all other energy parameters of the junction)

EL0 = 0; WL0 = 10; GammaL0 = 0.002; ER0 = 0; WR0 = 10; GammaR0 =
0.002;
```

```
%Energy of primary phonons (in eV);
omega0 = 0.2;

%Coupling between bridge electron states and primary phonon state (in eV)
Ma = 0.063;

%Coupling between primary phonon state and secondary phonon states (in eV)
%Equation 25: gammaph is independent of energy in phonon wide band limit
gammaph = 1e-3;

%Other parameters
Delta = Ma^2/omega0;
epsbar0 = eps0 - Delta;
lambdaa = Ma/omega0;
infdelta = 1e-6;
eta=1/2; %Voltage division factor
relchange = 1e-6; %Tolerance level
EF = epsbar0 - 2;
```

voltstep.m

```
%Equation numbers refer to equations in PRB 73, 045314 (Galperin, Nitzan
%and Ratner, Resonant Inelastic Tunneling in Molecular Junctions, 2006)

%Step 1

%Calculate the retarded electron self energy due to coupling to the
%contacts.
%EK0 is the centre of the band of the contact
%WK0 is the half width of the band of the contact
%GammaK0 is the escape rate to contact K in the electron wideband limit
%(WK0->infinity relative to all other energy parameters of the junction)

SigmaL0r = 1/2 * (GammaL0 * WL0) ./ (E-EL0 + i * WL0); %Equation 27
SigmaR0r = 1/2 * (GammaR0 * WR0) ./ (E-ER0 + i * WR0); %Equation 27
Sigma0r = SigmaL0r + SigmaR0r; %Equation 26

%Calculate the zero-order retarded phonon and electron Green functions
%in the energy domain.

D0r = 1 ./ (E-omega0 + i * gammaph/2) - 1 ./ (E + omega0 + i *
gammaph/2); G0r = 1 ./ (E-epsbar0-Sigma0r);
```

```
%**********************************************************************

%Step 2

%Obtain the lesser and greater projections of the phonon and electron Green
%functions with the Keldysh equations (equations 28 and 29).
%
%In the first iteration step we use the zero-order retarded Green functions
%with the phonon self energy due to coupling to the thermal bath in place
%of the full phonon self energy and with the zero-order (in vibronic
%coupling) electron self energy in place of the full electron self energy.

D0l = -i * N * gammaph ./ ((E-omega0).^2 + (gammaph/2)^2) - i * (1 +
N) * gammaph ./ ((E + omega0).^2 + (gammaph/2)^2); D0g = -i * N *
gammaph ./ ((E + omega0).^2 + (gammaph/2)^2) - i * (1 + N) * gammaph
./ ((E-omega0).^2 + (gammaph/2)^2);

%The phonon self energy due to coupling with the thermal bath is calculated
%using this formula.

Piphl = D0l ./ (abs(D0r).^2); Piphg = D0g ./ (abs(D0r).^2);

GammaL = -2 * imag(SigmaL0r); GammaR = -2 * imag(SigmaR0r);

fL=1 ./ (1 + exp((E-muL) ./ kT)); %Fermi Dirac distribution
fR=1 ./ (1 + exp((E-muR) ./ kT));

SigmaL0l = i * fL .* GammaL; SigmaR0l = i * fR .* GammaR; SigmaL0g =
-i * (1-fL) .* GammaL; SigmaR0g = -i * (1-fR) .* GammaR;

Sigma0l = SigmaL0l + SigmaR0l; Sigma0g = SigmaL0g + SigmaR0g;

G0l = abs(G0r).^2 .* Sigma0l; G0g = abs(G0r).^2 .* Sigma0g;

%Temporary set the Green functions as the zero-order Green functions and
%calculate the time domain Green functions and the time domain electron
%self energies.

Dr = D0r; Dl = D0l; Dg = D0g; Gr = G0r; Gl = G0l; Gg = G0g;

tDl = ifft(ifftshift(Dl)); tDg = ifft(ifftshift(Dg)); tDr =
ifft(ifftshift(Dr)); tGl = ifft(ifftshift(Gl)); tGg =
```

```
ifft(ifftshift(Gg)); tGr = ifft(ifftshift(Gr));

Sigmal = Sigma0l; Sigmag = Sigma0g; Sigmar = Sigma0r;

tSigma0l = ifft(ifftshift(Sigma0l)); tSigma0g =
ifft(ifftshift(Sigma0g)); tSigmal = tSigma0l; tSigmag = tSigma0g;

%*****************************************************************

%Step 3

Pielr = zeros(NE,1); AA = zeros(NE,1);

%Here starts the iteration.

itstep = 0; itcheck = 1;

while itcheck == 1

 Sigmarold = Sigmar;
 Pielrold = Pielr;
 Drold = Dr;
 Grold = Gr;
 AAold = AA;

%Calculate the correlation operators for the primary phonon shift
%generators using equations 34 and 35. This gives the operators in the time
%domain. Required therefore are the greater and lesser projections of the
%Green functions in the time domain.

tXad0Xat = exp(i * lambdaa^2 * (tDl-tDl(1))); tXatXad0 = exp(i *
lambdaa^2 * (tDg-tDg(1)));

%*****************************************************************

%Step 4

%Use the lesser and greater projections of the electron self energy, the
%lesser and greater projections of the electron Green function and the
%lesser and greater correlation functions for the primary phonon shift
%generators in (projections of) equation 21 to yield the lesser and greater
%phonon self energies due to coupling to the electron in the time domain.
%This is shown in equations 36 and 37.
```

```
tPiell = i * lambdaa^2 * tXad0Xat .* (conj(tSigma0g) .* tGl +
tSigma0l .* conj(tGg)); tPielg = i * lambdaa^2 * tXatXad0 .*
(tSigma0g .* conj(tGl) + conj(tSigma0l) .* tGg);
%tPiell = zeros(NE,1);
%tPielg = zeros(NE,1);

%Use the lesser and greater projections of the electron self energy and the
%lesser and greater correlation functions for the primary phonon shift
%generators in (projections of) equation 22 to yield the lesser and greater
%electron self energies due to coupling to the phonons in the time domain.
%This is shown in equations 38 and 39.

tSigmal = tSigma0l .* tXad0Xat; tSigmag = tSigma0g .* tXatXad0;

%It is noteworthy to point out that the phonon self energy contains
%contributions due to both coupling to the thermal bath and to the
%electron, while the electron self energy is a sum of contributions from
%the two contacts dressed by the electron-phonon interaction.

%The retarded self energies in time domain can be obtained from the lesser
%and greater counterparts. We use the time domain analog of the Lehmann
%representation to suppress negative time contributions on the FFT grid.
%See the paper for more information.

tPielr = exp(-4 * t/t(end))' .* (tPielg-tPiell); tSigmar = exp(-4
* t/t(end))' .* (tSigmag-tSigmal);

%The thus calculated self energies are transformed to the energy domain.

Piell = fftshift(fft(tPiell)); Pielg = fftshift(fft(tPielg)); Pielr
= fftshift(fft(tPielr)); Sigmal = fftshift(fft(tSigmal)); Sigmag =
fftshift(fft(tSigmag)); Sigmar = fftshift(fft(tSigmar));

Pil = Piphl + Piell; Pig = Piphg + Pielg;

%*********************************************************************

%Step 5

%Update the Green functions. The retarded Green functions in the energy
%domain are calculated using equations 40 and 41, the lesser and greater
%projections are then obtained from the Keldysh equations (equations 28 and
```

```
%29)

alpha = 1;

Dr = alpha * (1 ./ ((1 ./ D0r)-Pielr)) + (1-alpha) * Dr; Gr = alpha
* (1 ./ (E-epsbar0-Sigmar)) + (1-alpha) * Gr;

Dl = abs(Dr).^2 .* Pil; Dg = abs(Dr).^2 .* Pig; Gl = abs(Gr).^2 .*
Sigmal; Gg = abs(Gr).^2 .* Sigmag;

%The Green functions are now transformed to the time domain.

tDl = ifft(ifftshift(Dl)); tDg = ifft(ifftshift(Dg)); tDr =
ifft(ifftshift(Dr)); tGl = ifft(ifftshift(Gl)); tGg =
ifft(ifftshift(Gg)); tGr = ifft(ifftshift(Gr));

%*****************************************************************

%Step 6

%The updated Green functions are used in step 3, closing the self
%consistent loop. Steps 3-5 are repeated until convergence is achieved. As
%a test, we use the retarded projection of the electron self energy Sigmar.
%Convergence is achieved when the absolute change of the self energy
%in two subsequent iterations is less than a predefined tolerance which we
%call relchange.

GGl = fftshift(fft(tGl .* tXad0Xat)); GGg = fftshift(fft(tGg .*
tXatXad0)); AA = real(i * (GGg-GGl));

if max([abs(Sigmarold-Sigmar) ./ abs(Sigmar) ; abs(Pielrold-Pielr)
./ abs(Pielr) ; abs(Drold-Dr) ./ abs(Dr) ; abs(Grold-Gr) ./ abs(Gr)
; abs(AAold-AA) ./ abs(AA)]) < relchange
 itcheck = 0;
end itstep = itstep + 1;

end %of the while loop
```

Bibliography

[1] L. Turin and F. Yoshii, Structure-odor relations: a modern perspective, *Handbook of Olfaction and Gustation*, ISBN: 978-0824707194 (2002)

[2] L. Turin, Chem. Senses **21**, 773 (1996)

[3] G. Binnig, H. Rohrer, Ch. Gerber and E. Weibel, IBM J. Res. Dev. **30**, 355 (1986)

[4] K.W. Hipps, Scanning Tunneling Spectroscopy, *Handbook of Applied Solid State Spectroscopy*, ISBN: 978-0-387-32497-5 (2006)

[5] R.J. Hamers, Ann. Rev. Phys. Chem. **40**, 531-559 (1989)

[6] J.D. Langan and P.K. Hansma, Surf. Sci. **52**, 211 (1975).

[7] K.W. Hipps and U. Mazur, Inelastic Electron Tunneling Spectroscopy, *Handbook of Vibrational Spectroscopy*, ISBN: 978-0-471-98847-2 (2001).

[8] A. Bayman, P. Hansma and W.C. Kaska, Phys. Rev. B **24**, 2449 (1981)

[9] J.R. Hahn, H.J. Lee and W. Ho, Phys. Rev. Lett. **85**, 1914 (2000)

[10] B.N.J. Persson and A. Baratoff, Phys. Rev. Lett. **59**, 339 (1987)

[11] W. Wang, T. Lee, I. Kretzschmar and M.A. Reed, Nano Lett. **4**, 643 (2004)

[12] T. Mii, S.G. Tikhodeev and H. Ueba, Phys. Rev. B **68**, 205406 (2003)

[13] R.H.M. Smit, Y. Noat, C. Untiedt, N.D. Lang, M.C. van Hemert and J.M. van Ruitenbeek, Nature **419**, 906 (2002)

[14] J. Park, A.N. Pasupathy, J.I. Goldsmith, C.C. Chang, Y.Yaish, J.R. Petta, M. Rinkoski, J.P. Sethna, H.D. Abruna, P.L. McEuen and D.L. Ralph, Nature **417**, 722 (2002)

[15] W. Liang, M.P. Shores, M. Bockrath, J.R. Long and H. Park, Nature **417**, 725 (2002)

[16] M. Galperin, M.A. Ratner and A. Nitzan, Cond. Matt. **19**, 103201 (2006)

[17] A. Nitzan, J. Jortner, J. Wilkie, A.L. Burin and M.A. Ratner, J. Phys. Chem. B **104**, 5661-5 (2000)

[18] National Physical Laboratory, *Sputtering yields for neon, argon and xenon ions*, `http://www.npl.co.uk/nanoanalysis/sputtering_yields.html`, (Accessed 29 Aug 2007)

[19] J.H.A. Hagelaar, C.F.J. Flipse and A.P.J. Jansen, J. Phys. Conf. Series **61**, 379 (2007)

[20] G. Witte, J. Chem. Phys. **115**, 2757 (2001)

[21] T.W. Root, G.B. Fisher and L.D. Schmidt, J. Chem. Phys. **73**, 4679 (1989)

[22] G. Blyholder, J. Phys. Chem. **68**, 2772 (1964)

[23] H.B. Gray, *Electrons and Chemical Bonding*, New York, New York (1964)

[24] I. Tamm, Z. Phys. **76**, 849 (1932)

[25] W. Shockley, Phys. Rev. **56**, 317 (1939)

[26] L. Bürgi, *Scanning tunneling microscopy as local probe of electron density, dynamics, and transport at metal surfaces*, Thesis EPFL, no 2033 (1999).

[27] K. Morgenstern, K.-F. Braun and K.-H. Rieder, Phys. Rev. Lett. **89**, 226801 (2002)

[28] Ph. Avouris, I.-W. Lyo and P. Molinàs-Mata, Chem. Phys. Lett. **240**, 423 (1995)

[29] E.D.L Rienks, G.P. van Berkel, J.W. Bakker and B.E. Nieuwenhuys, 12th International Conference STM'03, AIP Conference Proceedings **696**, 734-737 (2003)

[30] S.K. So, R. Franchy and W. Ho, J. Chem. Phys. **91**, 5701 (1989)

[31] W.A. Brown, P. Gardner and D.A. King, J. Phys. Chem. **99**, 7065 (1995)

[32] W.A. Brown, P. Gardner, M. Perez Jigato and D.A. King, J. Chem. Phys. **102**, 7277 (1995)

[33] L.J. Lauhon and W. Ho, Phys. Rev. B. **60**, R8525 (1999)

[34] A.J. Heinrich, C.P. Lutz, J.A. Gupta and D.M. Eigler, Science **298**, 1381 (2002)

[35] J.R. Hahn and W. Ho, Phys. Rev. Lett **87**, 166102 (2001)

[36] J.R. Hahn and W. Ho, Phys. Rev. Lett **87**, 196102 (2001)

[37] H.J. Lee and W. Ho, Science **286**, 1719 (1999)

[38] L. Bartels, G. Meyer and K.-H. Rieder, Appl. Phys. Lett. **71**, 213 (1997)

[39] S. Raimes, *Many-electron theory*, North Holland, Amsterdam (1972).

[40] M. Galperin, M.A. Ratner and A. Nitzan, J. Chem. Phys. **121**, 11965 (2004).

[41] G.D. Mahan, *Many-Particle Physics*, 2nd ed., Plenum Press, New York (1990).

[42] L. Keldysh, Sov. Phys. JETP **20**, 1018 (1965).

[43] R.D. Mattuck, *A guide to Feynman diagrams in the many-body problems*, McGraw-Hill, London (1976)

[44] M. Galperin, A. Nitzan and M.A. Ratner, Phys. Rev B **73**, 045314 (2006).

[45] U. Lundin and R.H. McKenzie, Phys. Rev. B **66** 075303 (2002)

[46] J.-X. Zhu and A.V. Balatsky, Phys. Rev. B **67** 165326 (2003)

[47] I.G. Lang and Y.A. Firsov, Sov. Phys. JETP **16**, 1301 (1963)

[48] D.C. Langreth, in *Linear and Nonlinear Electron Transport in Solids*, edited by J.T. Devreese and D.E. Doren, Plenum Press, New York (1976), p. 3-32

[49] H. Haug and A.-P. Jauho, *Quantum Kinetics in Transport and Optics of Semiconductors*, Springer, Berlin (1996)

[50] Arrandee, *How to use arrandee/ Au(111) by flame annealing*, `http://www.arrandee.com` (Accessed 29 Aug 2007)

[51] Chemical Science & Technology Laboratory, *Growth of self-assembled monolayers*, `http://www.cstl.nist.gov/div836/836.04/SAMS/growth.htm` (Accessed 29 Aug 2007)

[52] S. Narasimhan and D. Vanderbilt, Phys. Rev. Lett. **69**, 1564 (1992)

[53] P. Han, B.A. Mantooth, E.C.H. Sykes, Z.J. Donhauser and P.S. Weiss, J. Am. Chem. Soc. **126**, 10787 (2004)

[54] J.V. Barthe, H. Brune, G. Ertl and R.J. Behm, Phys. Rev. B **42**, 9307 (1990)

[55] W. Chen, V. Madhavan, T. Jamneala and M.F. Crommie, Phys. Rev. Lett. **80**, 1469 (1998)